DEVELOPMENT OF *IN VITRO* MODELS TO EXAMINE CELL-MINERAL INTERACTION AND CELL-MEDIATED MINERAL FORMATION

A Dissertation

Presented to the Faculty of the Graduate School

of Cornell University

In Partial Fulfillment of the Requirements for the Degree of

Doctor of Philosophy

By

Debra DengWen Lin

January 2013

DEVELOPMENT OF *IN VITRO* MODELS TO EXAMINE CELL-MINERAL INTERACTIONS AND CELL-MEDIATED MINERAL FORMATION

Debra DengWen Lin, PhD
Cornell University, 2013

The development of hard tissues such as bone and teeth are examples of biomineralization processes in which organisms actively direct mineralization. The formation of hard tissues is a highly regulated process involving the coordination of extracellular matrix production by the cells and the mineralization of the matrix network regulated by proteins secreted by the cells. The formation of these tissues follows a sequence of events in a spatial and temporal manner dictated by cellular processes. In addition to the cells involved in the formation and remodeling of hard tissues, such as osteoblasts (OBs) and osteoclasts (OCs) in bone, other cell-types, such as breast and prostate tumor cells, can interact with bone.

Two strategies were taken in this thesis to understand how cells are involved in the mineralization process. Cell culture systems were designed to examine cell-mineral interactions or to examine cell-mediated mineral formation. Chapter 1 discusses the requirements for sustaining cell viability and function as well as the various components involved in designing cell culture systems such as cell source, culture method, and mineral source.

Culture systems to study cell-mineral interactions require an environment containing the mineral of interest for cells to be cultured upon. Hydroxyapatite ($Ca_{10}(PO_4)_6(OH)_2$, HA) is the main mineral component of bone and has been noted to change in size, shape, and crystallinity with age, anatomical location, and disease progression. Chapter 2 describes a two-step method for synthesizing hydroxyapatite nanoparticles with controlled shape, size, and crystallinity in order to evaluate how differences in HA crystal properties can affect cellular response.

Three culture systems were developed and described in this work. Two systems were developed to utilize the synthetic hydroxyapatite nanoparticles (prepared in Chap. 2) for

examining cell-mineral interactions. In Chapter 3, dry-annealed synthetic and commercial HA particles were combined with polylactide(co-glycolide) (PLG) and spin-coated onto glass substrates to form a film of PLG-HA to examine how changes in crystallinity can affect OB attachment and matrix production. Chapter 4 describes the integration of a series of hydrothermally aged HA nanoparticles into porous PLG scaffolds to examine breast cancer cell response to various HA nanoparticles with discrete sizes. Finally, Chapter 5 details the third system designed for culturing cells in a 3-D gel system that allows for the presence of 1-D gradients to study cell-mediated mineral formation with articular chondrocytes.

Due to the breadth of components involved, designing culture systems for mineralization studies are complex and selection of cell source, culture method, and mineral source should be dictated by research questions of interest of particular aspects of these processes (Chapter 1). Chapter 2 demonstrates how controlling for reactant salts, reactant concentration, reaction duration, and reaction volume in the initial precipitation step leads to changes in shape (e.g., rounded to plate-like) and phase (e.g., brushite to HA) while further post-processing techniques can be applied to tune phase, size, crystallinity, and dispersity. Surfaces containing dry-annealed particles increased fibronectin secretion from osteoblasts in Chapter 3, however this response was not due solely to an increase in crystallinity, and other changes to the surfaces due to heat treatment need to be examined. Breast tumor cells in Chapter 4 attached better on scaffolds containing smaller, less crystalline HA, however interleukin-8 (IL-8) secretion was upregulated in cells cultured on scaffolds containing larger, more crystalline HA, indicating IL-8 as a potential factor in facilitating breast cancer tumor metastasis processes. Chapter 5 establishes a 3-D culture system which can support cell viability and matrix production with future work to optimize the system for culturing cells under mineralizing gradients.

BIOGRAPHICAL SKETCH

Debra DengWen Lin was born on September 4, 1985 to TsanHai Lin and ShuFen Huang. Her parents had immigrated to the United States in search of better opportunities and encouraged Debra to do the same. She found science with medical applications to be fascinating and sought colleges with research opportunities in the field. Debra graduated from Auburn High School ranked number 1, varsity tennis MVP, gold medalist pianist, with a bunch of medals from Science Olympiad, and went on to attend the Massachusetts Institute of Technology fall of 2003.

At MIT, Debra joined Course 3, the Department of Materials Science & Engineering. During that time, she authored a patent at her summer internship at Toyota Motor Corporation in Japan, pulled an all-nighter with a group of friends to write a successful SBIR grant, and drove around Boston on the MIT ambulance as an EMT. While studying abroad at the University of Cambridge, she hitch-hiked across Europe to raise funds to support educational opportunities for children in Africa. To continue her interest in science with medical applications, she decided to pursue graduate studies. During Cornell's graduate school visitation weekend, Debra met Professor Lara Estroff whose passion for Biomineralization and fascinating research got her to sign up. Debra completed her BS in Course 3 at MIT in 2007.

Debra joined Prof. Estroff's group and began her graduate work at Cornell University in fall of 2007. She is a National Science Foundation Graduate Research Fellow, NSF East Asia & Pacific Summer Institute Program Fellow, ICCBMT Poster Award Recipient, and Featured Woman in STEM. Through these years she has worked on many projects towards understanding the biomineralization processes of bone and calcification from a materials and biological perspective. In January 2013, Debra will be the second person in the family history to have earned a PhD. She will begin work at the Research and Innovation Lab at L'Oreal, focusing on topics in skincare.

DEDICATION

To my grandfather, Fu Huang, who had the vision,

To my mother, ShuFen Huang, who was the motivation,

And to my father, TsanHai Lin, who made it happen.

Thank you for the life I am able to lead.

ACKNOWLEDGEMENTS

This work would not have been possible without the support and mentorship of many individuals and funding agencies. I would like to thank first and foremost, my advisor and committee chair Professor Lara Estroff for her mentorship and enthusiasm throughout my experience at Cornell University. She has been an incredible support and inspiration.

To my committee members Dr. Adele Boskey who took me in for an entire summer and Professor Ulrich Wiesner for letting me crash at his sabbatical home in Australia, thank you for sharing your knowledge and thoughts on life.

To my collaborators Professor Claudia Fischbach-Teschl, Siddharth Pathi, Professor Lawrence Bonassar, Dr. Omotunde Babalola, Professor Dietmar W. Hutmacher, Dr. Anna Taubenberger, and their group members, thank you for welcoming me to your lab.

To my group members, especially Dr. Hanying Li, Dr. Ellen Keene, Dr. Jason Dorvee, Emily Asenath-Smith, and Miki Kunitake, good times.

To my undergraduates, especially Kevin Eckes and Wangzhong Sheng, you are wonderful.

To my family for their love and cheers, especially my father TsanHai Lin, who went through this before and deeply empathizes, and my sister Jessica Lin who read every page of every chapter of this work, lots of love.

I would also like to thank my funding sources, the National Science Foundation Graduate Research Fellowship and East Asia & Pacific Summer Institutes Program, the National Institutes of Health, Cornell Center for Materials Research, and Professor Estroff.

TABLE OF CONTENTS

LIST OF FIGURES

LIST OF TABLES

LIST OF ABBREVIATIONS

2X	Twice concentrated
ACP	Amorphous Calcium Phosphate
AB/AM	Antibiotics/Antimycotics
BCA	Bicinchonic Acid
BSA	Bovine Serum Albumin
Ca	Calcium
CaP	Calcium Phosphate
cDMEM	Culture Dulbecco's Modified Eagle Media supplemented with 10% FBS, 1% AB/AM
DCPD	Dicalcium Phosphate Dihydrate
DI-H_2O	Deionized Water
DMEM	Dulbecco's Modified Eagle Media
ECM	Extracellular Matrix
FN	Fibronectin
FTIR	Fourier Infrared Spectroscopy
FBS	Fetal Bovine Serum
GAG	Glycosaminoglycans
HA	Hydroxyapatite
HEPES	*N*-2-hydroxyethyl piperazine-*N*′-2-ethanesulfonic acid
hOB	Human Osteoblasts
ICP-AES	Inductively Coupled Plasma Atomic Emission Spectrometry
IL-8	Interleukin-8
$NaHCO_3$	Sodium Bicarbonate

NCP	Noncollagenous Protein
NM	Non-Mineral-Containing
OB	Osteoblast
OC	Osteoclast
OCP	Octacalcium Phosphate
P	Phosphate
PBS	Phosphate Buffered Saline
PEI	Polyethylene-imine
PLG	Polylactide(co-glycolide)
PS	Polystyrene
PS-STRS	Polystyrene Tube-STRS
PTHrP	Parathyroid Hormone Related Peptide
pXRD	Powder X-Ray Diffraction
S	Silicone
S-STRS	Silicone Tube-STRS
sHA	Synthetic HA
STRS	Single Tube Reservoir System
TE	Tissue Engineered
TEM	Transmission Electron Microscopy
TCP	Tricalcium Phosphate
THF	Tetrahydrofuran
Tris	Tris(hydroxymethyl)aminomethane
XRD	X-Ray Diffraction

CHAPTER 1
INTRODUCTION: DESIGN REQUIREMENTS FOR CELL CULTURE SYSTEMS FOR MINERALIZATION STUDIES

1.1 Abstract

The development of cell culture systems to understand cell-mineral and cell-mineralization interactions with hydroxyapatite (HA, $Ca_{10}(PO_4)_6(OH)_2$), the main mineral component of bone, is a growing field due to the need for better bone-regeneration and bone-healing materials for bone repair. The growth, development, and healing of hard tissues such as bone and teeth is a complex process dictated by cell function and response to the bone microenvironment. Furthermore, bone is a living tissue that changes with time as bone remodels with age and in response to disease pathology. In order to understand these processes, it is necessary to develop model systems that break down this process into simpler components. Chapter 1 discusses the design requirements for developing cell cultures for mineralization studies.

1.2 Introduction

Cell culture systems for mineralization studies are valuable tools to understand the development, healing, and breakdown of hard tissues. The processes by which mineralized tissues are formed are complex and involve cellular processes, the extracellular matrix (ECM), noncollagenous proteins (NCPs), and ion gradients [1]. To break down the complexity, *in vitro* models can be designed to investigate particular components associated with the mineralization process. Due to the breadth of questions and large number of components associated with the mineralization process, cell culture systems for mineralization studies are designed to examine specific cell-mineral interactions or cell-mediated mineral formation processes. This thesis focuses on designing cell culture systems to examine cellular behavior with changes in the mineral hydroxyapatite (cell-mineral interaction) and how the presence of cells can affect the formation of hydroxyapatite (cell-mediated mineral formation).

Hydroxyapatite (HA), chemical formula $Ca_{10}(PO_4)_6(OH)_2$ is the hard component of mineralized tissues such as bone and teeth. For example, HA comprises up to 96 wt% of tooth enamel and 70 wt% of bone [2]. The other components include the extracellular matrix (ECM) made up of collagen (bone) or amelogenin (tooth enamel), noncollagenous proteins (NCPs), and water. The HA and ECM act as a composite material and contribute properties such as toughness and stiffness to mineralized tissues allowing for functions such as mobility, organ protection, and food processing [3, 4]. In addition to bone and teeth, a gradient of HA is also found at the osteochondral interface between subchondral bone and articular cartilage [5]. The gradient of mineral allows for the transition of forces from the stiff bone to the more compliant cartilage.

Cells play an important role in the formation, maintenance, and healing of mineralized tissues. For example, the bone microenvironment is constantly being remodeled by bone cells. Osteoblasts (OBs) are the bone cells responsible for the production of new bone. The OBs deposit an extracellular matrix, the osteoid, comprising of mainly of collagen type I and assist in the mineralization of the osteoid to form new bone [6]. Overtime, as OBs become enclosed within bone, some become osteocytes, and continue to interact with the bone matrix. Osteoclasts (OCs) are bone cells that break down old or damaged bone. In addition to secreting the matrix framework for mineralization and clearing away old bone, osteoblasts and osteoclasts also play multiple roles in controlling and modulating the mineralization process. These cells produce an assortment of NCPs involved in the mineralization process by acting as controls for cell binding and regulation of mineralization during the crystal nucleation and growth process of HA [7]. In addition to the cells found in bone, other cell types also interact with bone and HA. At the osteochondral interface, deep-zone articular chondrocytes in cartilage are embedded in a gradient of mineral [8] and have the ability to influence the formation of the mineralized region of cartilage [9, 10]. In advanced stages of several cancers, tumor cells can metastasize to bone [11]. The regions of bone with metastatic tumor cells are at risk of forming osteolytic or osteoblastic lesions. The cancer cells interact with the bone cells and therefore alter the mineral environment and respond to changes in environmental cues.

Cells are sensitive to their surrounding environment and changes in surface roughness [12], the presence of nano-sized compared to micro-sized surface features [13, 14], and mineral phase [15] have evoked different cellular responses in OBs and OCs. In addition, as a function of tissue age, anatomical location, and disease progression, the mineral component HA in tissues

can change in size [16, 17], crystallinity [18, 19], and density [20]. These changes influence the microenvironment of the tissue.

Hard tissue development is dictated by cellular function in producing the ECM and utilizing NCPs to regulate the mineralization of the ECM [21]. Culture systems have been developed to examine the mineral formation process by culturing cells to confluence on surfaces to allow matrix formation then mineral formation by adding phosphate to the cultures [22, 23]. Other methods attempt to recreate tissues in 3-D scaffolds before inducing mineral formation *in vitro* [24, 25]. These methods lack controls to study the mineralization process in a spatial and temporal manner.

In vitro models can be designed to examine cell-mineral interactions and cell-mediated mineral formation to determine their roles in the bone mineralization and healing process. This thesis dissertation discusses the development of *in vitro* models to better understand the bone mineralization process via two approaches: designing cell culture systems to examine cell-mineral interactions and cell culture systems to examine cell–mineral formation. In pursuit of understanding how changes in the environment due to changes in HA such as size and crystallinity can affect cell response to examine cell-mineral interactions, synthesis methods for obtaining HA of specific size and crystallinity were developed. The HA was then introduced into two different culture systems: polymer films on glass substrates and 3-D porous polymer scaffolds. Towards examining cell-mediated mineral formation, a 3-D culture system was developed to introduce ion gradients relevant to mineralization to cells for study of the spatial and temporal changes regulated by cells during the formation of mineral. This work presents the design requirements necessary for developing cell culture systems to study mineralization

processes of hard tissue through the development of cell culture systems that examine cell response to changes in the microenvironment and cell regulation of the formation of HA.

1.3 Experimental Design Requirements

1.3.1 General Requirements for Culturing Cells

The standard consideration for systems to examine cell-mineralization interaction is the merging of the requirements for maintaining cell health and functionality and the requirements for stable HA and/or ions for the formation of HA [1]. Conditions for cell culture are more rigid, as most cell types require an environment of 37.5 ºC, pH 7.4, 5% CO_2, humidity, and a source of nutrients for the cells. The most common source of nutrients supplied to cell cultures are liquid nutrient media containing a combination of salts, amino acids, vitamins, and sugar to support cell growth and proliferation. The formulation of the nutrient media is not uniform for all cell types and is selected based on the cell type and cell source [26]. Media cultures are further supplemented with additives such as fetal bovine serum (FBS), antibiotics/antimycotics (AB/AM), ascorbic acid, and other growth factors which improve cell growth, prevent infections, and enhance ECM production. The following sections further describe individual components required for designing cell culture systems such as the selection of cell source, the culture method, and source of HA mineral (Fig 1.1).

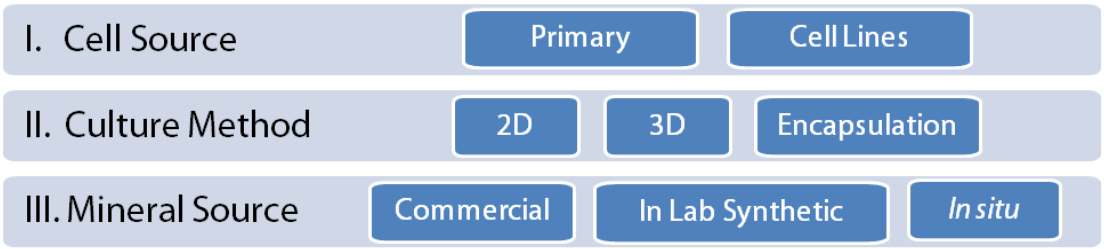

Figure 1.1: Schematic of the components necessary in designing cell culture systems for mineralization studies.

1.3.2 Cell Source Selection: Primary Cells vs. Cell Lines

Cells can be obtained from a number of sources. The cell types utilized in the thesis are primary human osteoblasts, primary bovine articular chondrocytes, and MDA-MB231 cells from a tumor cell line. Primary cell sources are harvested directly from the tissue of interest, such as long bones or the periosteum, and cells are obtained via enzyme digestion [27, 28]. Primary cells provide a close analog of what occurs *in vivo*. Tumor cell lines are convenient for reproduction of large quantities of genetic clones and have the same response and phenotype under the same experimental conditions [29]. However, due to the genetic modification, cells from cell lines do not fully reflect the *in vivo* response and can be selected to have specific responses such as the preferred attachment of MDA-MB231 cells to bone [30].

1.3.3 Culture Methods: 2-D, 3-D, and Encapsulation

In addition to providing an environment suitable for cell growth (Section 1.3.1) and selecting the cell source (Section 1.3.2), geometrical considerations of the culture system should be taken into account. Cells can be grown on surfaces in 2-D cultures in flasks or petri dishes. Surface cultures allow for high proliferation rates, easy exchange of gases and wastes, and replenishment of nutrients. Progression of the culture can be easily examined via optical microscopy and other surface techniques such as atomic scanning microscopy [1]. However, the cellular growth and development on flat surfaces can lead to changes in cell phenotype which can induce cell differentiation into different cell types [31]. To present a more biologically relevant environment, cells can be cultured in 3D systems or via encapsulation within a matrix. 3D cultures such as porous polymeric scaffolds provide limited surface area for proliferation, which also limits access to nutrients or molecules of interest depending on the distance from the

edge of the construct [32, 33]. In the case of encapsulation, where cells are surrounded by the culture medium such as in hydrogels, cells have access to molecules of interest and nutrients via diffusion; however they are also generally isolated from other cells [35]. Tumor cells grown in 3-D scaffolds were able to more closely mimic tumor tissue compared to the same cells cultured on surfaces [32]. Osteoblast-like cells MC3T3 had different levels of gene expression in 2D compared 3D culture environments [36]. Culture systems in 2-D (Chapter 3), 3-D (Chapter 4) and encapsulation (Chapter 5) were investigated in this thesis.

1.3.4 Conditions for Introducing Hydroxyapatite to Cells

The solubility of HA is relatively low, with a K_{sp} of 6.62×10^{-126} at 25°C [37]. Under the conditions for cell culture in the absence of cells, HA particles are stable and show little evidence of dissolution [30] indicating the suitability of introducing HA nanoparticles into culture systems to examine the interaction with cells. HA can be obtained through commercial sources as well as synthesized in the laboratory [38, 39]. However, the nanometer length scales of most of these sources of HA make HA particles susceptible to phagocytosis by cells, which can induce an inflammatory response [40]. For examining surface interactions of cells with HA, platforms are necessary to present HA to cells to avoid phagocytosis. Embedding HA particles into a polymer scaffold prevents cells from taking in HA particles while presenting a surface for cells to interact with the HA. This method is utilized in Chapters 3 and 4 for examining how cells interact with different types of HA.

1.3.5 Conditions for the Formation of Hydroxyapatite In Situ

Additional challenges arise for culture systems that induce the formation of HA in situ. Culture systems designed to induce mineralization add relatively low concentrations of calcium and phosphate (Ca X P 5.5 mM^2) to the media at ratios favorable for HA [22, 41]. Cells are able to sequester the calcium and phosphate ions to form mineral in culture. Alternatively, formation of mineral can be imposed on the cells within gel systems by increasing the concentration of calcium and phosphate ions introduced to the culture, however, challenges arise as the higher concentration of ions interact more readily with culture buffers for pH and with the mineral inhibitors in serum [10, 42]. These concerns are further addressed in Chapter 5.

1.4 Thesis Summary

The objective of this thesis work was to develop cell culture systems to understand the role of the mineral component HA in providing environmental cues for cells and to understand the role of cells in modulating the formation of the HA mineral during the mineralization process. These culture systems needed to maintain cell viability and function in the presence HA or ion gradients for the formation of HA. Two strategies were applied to the design of these systems to investigate cell-mineral interaction and cell-mediated mineral formation.

In the first approach to examine cell-mineral interactions, methods to synthesize HA with a range of size and crystallinity were developed. HA in hard tissues come in a variety of sizes, crystallinities, and morphologies. To investigate how these parameters impact the environment in contact with cells, a range of HA particles with differences in size, crystallinity, and morphology need to be obtained synthetically. Commercially available particles are the most commonly used source of HA. However, these particles often have a wide range of sizes and

contain impurities. Chapter 2 describes a two-step synthesis method for HA which allows for tuning of the HA properties at multiple points of the synthesis process to obtain populations of HA particles with well-defined sizes, crystallinities, and morphologies.

Chapter 3 utilizes dry annealed HA precipitate synthesized by methods described in Chapter 1 to investigate how heat treatment induced changes in crystallinity and other factors can affect cellular response. HA precipitate was mixed with poly(lactide-co-glycolide) (PLG) and spin-coated onto glass substrates. Primary human osteoblasts were obtained from patients undergoing knee replacement surgery and cultured onto the surfaces. OB sensitivity to the changes in HA properties induced from heat treatment were evaluated by examining differences in adhesion, spreading, metabolic activity, and fibronectin production of the cells cultured on the surfaces.

Pursuing the question of crystallinity further, Chapter 4 describes the incorporation of HA with size and crystallinity differences obtained through hydrothermal aging of HA precipitates by methods described in Chapter 1 into porous PLG 3-D scaffolds. Scaffolds were seeded with MDA-MB231 breast cancer cells. Tumor cell adhesion, proliferation, and protein secretion on the scaffolds were evaluated to determine the influence of HA size and crystallinity on tumor cell response.

In the second approach to examine cell-mediated mineral formation, a system was developed to encapsulate cells in an environment suitable for HA crystal growth in situ. Chapter 5 describes how primary bovine articular chondrocytes were encapsulated by agarose gel in a 3-D gel diffusion system to understand how the presence of cells can influence the presence of ion gradients for mineral formation. The culture system was optimized to sustain cell viability and

matrix production. Preliminary results from introducing gradients of calcium and phosphate for mineralization are included in Chapter 5.

1.5 Conclusions

Understanding the mineralization process of biological organisms in developing their skeleton can assist in the design and development of the next generation of hard tissue repair materials. Replicating similar mechanisms utilized by nature to control the nucleation, growth and morphology of bone mineral HA will provide materials with similar properties to that of native tissue and allow for the study of where these crystals are formed and how they are organized within the body. Through the development of these *in vitro* models to examine cell-mineral and cell-mineralization interactions, I hope to further the understanding of bone development, regeneration, and healing.

References

[1] Boskey AL, Roy R. Cell culture systems for studies of bone and tooth mineralization. Chem Rev 2008;108(11):4716-33.

[2] Nanci A. Ten Cate's Oral histology: development, structure, and function. Mosby, Elsevier, St. Louis, 2008.

[3] Moffat, KL, Wang, IN, Rodeo, SA, Lu, HH. Orthopedic interface tissue engineering for the biological fixation of soft tissue grafts. Clinics in Sports Med 2009;28(1):157-88.

[4] Weiner S, Wagner HD. The material bone: Structure-mechanical function relations. Annu Rev Mater Sci 1998;28:271-89.

[5] Johnson K., Terkeltaub R. Inorganic pyrophosphate (PPI) in pathologic calcification of articular cartilage. Frontiers in Bioscience 2005;10:988-97.

[6] Hott M, Noel B, Bernache-Assolant D, Rey C, Marie PJ. Proliferation and differentiation of human trabecular osteoblastic cells on hydroxyapatite. J Biomed Mater Res 1997;37:508-16.

[7] Vogel V, Baneyx G. The Tissue engineering puzzle: a molecular perspective. Annu Rev Biomed Eng 2003;5:441-63.

[8] Tortelli F, Cancedda R. Three-dimensional cultures of osteogenic and chondrogenic cells: a tissue engineering approach to mimic bone and cartilage in vitro. Euro Cells Mater 2009;17:1-14.

[9] Jiang J, Nicoll SB, Lu HH. Co-culture of osteoblasts and chondrocytes modulates cellular differentiation *in vitro*. Biochem Biophys Res Comm 2005;338(2):762-770.

[10] St-Pierre JP, Pillar RM, Grynpas MD, Kandel RA. Calcification of cartilage formed *in vitro* on calcium polyphosphate bone substitutes is regulated by inorganic polyphosphate. Acta Biomater 2010;6(8):3302-9.

[11] Pathi SP, Kowalczewski C, Tadipatri R, Fischbach C. A novel 3-D mineralized tumor model to study breast cancer bone metastasis. PLoS One. 2010;5(1):e8849.

[12] Geblinger D, Addadi L, Geiger B. Nano-topography sensing by osteoclasts. J Cell Sci 2010;1(123 pt9):1503-10.

[13] Gittens RA, Olivares-Navarrete R, McLachlan T, Cai Y, Hyzy SL, Schneider JM, Schwartz Z, Sandhage KH, Boyan BD. Differential response of osteoblast lineage cells to

nano-topographically-modified, micro-roughened titanium-aluminum-vanadium alloy surfaces. Biomaterials 2012;33(35):8986-94.

[14] Palin E, Liu H, Webster TJ. Mimicking the nanofeatures of bone increases bone-forming cell adhesion and proliferation. Nanotech 2005;16:1828-1835.

[15] Monchau F, Lefévre A, Descamps M, Beluqin-myrdycz A, Laffargue P, Hildebrand HF. *In vitro* studies of human and rat osteoclast activity on hydroxyapatite, β-tricalcium phosphate, calcium carbonate. Biomolecular Eng 2002;19:143-152.

[16] Boskey AL. Bone mineral crystal size. Osteoporosis International 2003;14:S16-20.

[17] Rohanizadeh R, LeGeros RZ, Bohic S, Pilet P, Barbier A, Daculsi G. Ultrastructural properties of bone mineral of control and tiludronate-treated osteoporotic rat. Calcif Tissue Int 2000;67:330-6.

[18] Lange C, Li C, Manjubala I, Wagermaier W, Kuhnisch J, Kolanczyk M, Mundios S, Knaus P, Fratzl P. Fetal and postnatal mouse bone tissue contains more calcium than is present in hydroxyapatite. J Struc Biol 2011;176(2):159-67.

[19] Kuhn LT, Grynpas MD, Rey C, Wu Y, Ackerman JL, Glimcher MJ. A comparison of the physical and chemical differences between cancellous and cortical bovine bone mineral at two ages. Calcif Tissue Int 2008;83(2):146-54.

[20] Donnelly E, Meridth DS, Ngyuyen JT, Gladnick BP, Rebolledo BJ, Shaffer AD, Lorich DG, Lane JM, Boskey AL. Reduced cortical bone compositional heterogeneity with bisphosphonate treatment in postmenopausal women with intertrochanteric and subtrochanteric fractures. J Bone Min Res 2012;27(3):672-8.

[21] Lowenstam HA, Weiner S. On Biomineralization. Oxford University Press 1989.

[22] Reichert JC, Quent VMC, Burke LJ, Stansfield SH, Clements JA, Hutmacher DW. Mineralized human primary osteoblast matrices as a model system to analyze interactions of prostate cancer cells with the bone microenvironment. Biomaterials 2010;31:7928-36.

[23] Ahrens PB, Solursh M, Reiter RS. Stage-related capacity for limb chondrogenesis in cell culture. Dev Biol 1977;60(1):69-82.

[24] St-Pierre JP, Pilliar RM, Grynpas MD, Kandel RA. Calcification of cartilage formed *in vitro* on calcium polyphosphate bone substitutes is regulated by inorganic polyphosphate. Acta Biomater 2010;6(8):3302-9.

[25] Spalazzi JP, Dagher E, Doty SB, Guo XE, Rodeo SA and Lu HH. *In vivo* evaluation of multi-phased scaffold designed for orthopedic interface tissue engineering and soft tissue-to-bone integration. J Biomed Mat Res A 2008;86A(1): 1-12.

[26] Fundamental techniques in cell culture – 2nd Edition. European Collection of Cell Cultures and Sigma-Aldrich®, 2010.

[27] Gay CV, Lloyd QP. Characterization of calcium efflux by osteoblasts derived from long bone periosteum. Comp Biochem Physiol A Physiol 1995;111(2):257-61.

[28] Declercq HA, Verbeeck RM, De Ridder LI, Schacht EH, Cornelissen MJ. Calcification as an indicator of osteoinductive capacity of biomaterials in osteoblastic cell cultures. Biomaterials 2005;26(24):4964-74.

[29] Bodine PV, Komm BS. Tissue culture models for studies of hormones and vitamin action in bone cells. Vitam Horm 2002;64:101-51.

[30] Pathi SP, Lin DDW, Dorvee JR, Estroff LA, Fischbach C. Hydroxyapatite nanoparticle-containing scaffolds for the study of breast cancer bone metastasis. Biomaterials 2011;32(22):5112-22.

[31] Anselme K. Osteoblast adhesion on biomaterials. Biomaterials 2000; 21:667-81

[32] Fischbach C, Chen R, Matsumoto T, Schmelzle T, Brugge JS, Polverini PJ, Mooney DJ. Engineering tumors with 3-D scaffolds. Nature Methods 2007;4:855-60.

[33] Barron MJ, Tsai CJ, Donahue SW. Mechanical stimulation mediates gene expression in MC3T3 osteoblastic cells differently in 2D and 3D environments. J Biomech Eng 2010;132(4):041005.

[34] Grinnell F. Fibroblast biology in three-dimensional collagen matrices. Trends Cell Biol 2003; 13:264-9

[35] Cukierman E, Pankove R, Yamada KM. Cell interactions with three-dimensional matrices. Curr Opin Cell Biol 2002; 14:633-9

[36] Chatterjee K, Lin-Gibson S, Wallace WE, Parekh SH, Lee YJ, Cicerone MT, Young MF, Simon CG Jr. The effect of 3D hydrogel scaffold modulus on osteoblast differentiation and mineralization revealed by combinatorial screening. Biomaterials 2010;31(19):5051-62.

[37] Elliot JC. Structure and chemistry of the apatites and other calcium orthophosphates. Elsevier 1961.

[38] Dorozhkin SV. Nanosized and nanocrystalline calcium orthophosphates. Acta Biomaterialia 2010;6(3):715-34.

[39] Conz MB, Granjeiro JM, Soares GdA. Physicochemical characterization of six commercial hydroxyapatites for medical-dental applicatons as bone graft. J Applied Oral Sci 2005;13:136-40.

[40] Alliot-Licht B, Gregoire M, Orly I, Menanteau J. Cellular activity of osteoblasts in the presence of hydroxyapatite: an in vitro experiment. Biomaterials 1991;12(8):752-6.

[41] Boskey AL. Hydroxyapatite formation in a dynamic collagen gel system: effects of type I collagen, lipids, and proteoglycans. J Phys Chem 1989;93(4):1628-33.

[42] Pasch A, Farese S, Gräber S, Wald J, Richtering W, Floege J, Jahnen-Dechent W, A nanoparticle-based serum test measuring overall calcification inhibition, J Am Soc Nephrol 2012;23(10):1744-52.

CHAPTER 2
SYNTHESIS METHODS FOR HYDROXYAPATITE NANOPARTICLES WITH CONTROLLED SIZE, SHAPE, AND CRYSTALLINITY

Contributors: Wangzhong Sheng, Jason Dorvee, Lara Estroff

2.1 Abstract

With age, anatomic location, and disease progression, the mineral component of bone, hydroxyapatite (HA, $Ca_{10}(PO_4)_6(OH)_2$), changes. Variations in the bone microenvironment, which result in part from the materials properties of the HA nanocrystals, may lead to variation in cellular response and functions of cells in contact with bone. To investigate the effect of specific HA properties on cellular response, it is necessary to develop reproducible synthesis methods for producing HA with specific size, shape and crystallinity. This chapter describes a method to synthesize HA nanoparticles with controlled size, shape, and crystallinity via a two-step process. The first step is to precipitate HA from calcium and phosphate salts in solution. Initial parameters such as choice of ionic salts and reaction volume were varied to evaluate their effect on HA precipitation. In the second step, the HA precipitate was subject to "post-processing" steps such as dry-annealing, hydrothermal aging, and dialysis to obtain narrow distributions in size, shape, and crystallinity of HA nanoparticles. The phase of the precipitate was identified by x-ray diffraction (XRD), crystallinity characterized with fourier transform infrared spectroscopy (FTIR), and shape examined via transmission electron microscopy (TEM). Particles were utilized in studies described in Chapters 3 and 4 of this thesis. The results of this work will provide further insight into how HA nanoparticles can be used to determine the effects of specific properties of HA, such as crystallinity, chemical composition, and size, on cellular activity and, ultimately, bone regeneration and healing.

2.2 Introduction

Hydroxyapatite ($Ca_{10}(PO_4)_6(OH)_2$, HA) found in mineralized tissues come in a wide variety of shapes, such as nanoplatelets in bone [1] and rods in tooth enamel [2]. Pathological mineralization of soft tissues have also been observed, e.g. spherical and needle-like HA, in healthy heart valves and transplanted porcine heart valves [3, 4]. Changes have been noted in HA plate thickness [5, 6] and crystal size and order (crystallinity) [7] with organism age. HA crystal thickness and bone heterogeneity has also been observed to be affected by disease progression and drug treatment in osteoporotic mice and patients [8, 9]. These changes in HA properties can lead to changes in the bone microenvironment and may regulate cellular response [10, 11].

Cell behavior has been demonstrated to be affected by mineral characteristics such as phase, size, and crystallinity. Osteoblasts (OBs) cultured with different phases of calcium phosphate (CaP) such as HA, tricalcium phosphate (TCP), and amorphous calcium phosphate (ACP) have shown varying levels of osteoconduction, adsorption, and proliferation [12, 13]. Other cell types, such as osteoclasts, demonstrated differences in differentiation on surfaces with similar roughness, but different phases of CaP such as HA and TCP [14]. Nanoparticle size has been observed to affect the adsorption of proteins [15, 16] and influence attachment of cells [17, 18]. HA crystallinity has also shown to affect adsorption and proliferation of cells as well as the adsorption of proteins relevant for cellular function in attachment and tissue formation [13, 19-21]. These studies show the sensitivity of cells to differences in mineral properties *in vitro*, however, much of the work utilizes CaP materials with a wide dispersity of sizes with few controls over the nanoscale materials properties.

The variety of HA size, shape, and morphology in biology, requires the development of synthetic methods to obtain HA with a range of properties to investigate how these properties can regulate cell response. Commercially available HA particles are heterogeneous in size, shape, and chemical composition [16, 22]. Synthesis methods to obtain HA nanoparticles with narrow size distributions often depend on the presence of surfactants or on fractionation which introduces organic impurities to the HA and provide lower yields [23-26]. This chapter details a two-step process, which begins with the precipitation of HA from aqueous solutions of soluble calcium (Ca) and phosphate (P) salts, followed by a selection of post-processing methods of the precipitate to obtain HA nanoparticles with controlled size, shape, and crystallinity.

2.3 Materials & Methods

2.3.1 Step I: Aqueous Precipitation of Hydroxyapatite Nanoparticles

What follows is a general procedure for aqueous precipitation of HA from Ca and P salts. All chemicals were obtained from Sigma Aldrich and used as received. Ca salts ($Ca(NO_3)_2 \cdot 4H_2O$, $CaCl_2 \cdot 2H_2O$) and P salts (Na_2HPO_4, $(NH_4)_2HPO_4$) were dissolved in deionized water (DI-H_2O) at particular concentrations as described in the following experimental sections. The pH of the Ca and P solutions was adjusted with 0.1 M HCl for reactions with $CaCl_2$, 0.1 M HNO_3 for $Ca(NO_3)_2 \cdot 4H_2O$, 0.1 M NH_4OH for $(NH_4)_2HPO_4$, and 0.1 M NaOH for Na_2HPO_4. The pH of the reactants was brought to pH 9-9.5 before mixing and not maintained through the course of the reaction. All solutions were passed through a 0.45 μm pore-size filter (Whatman) before mixing. Reaction temperature was maintained at 4 ºC via an ice-water bath for first 6 hrs then allowed to warm to room temperature with further stirring. P solutions were added drop-wise from 18 gauge syringes (PrecisionGlide®) at a rate of 6.7 ± 0.5 mL/min by hand, timed in

minute intervals, into Ca solutions in an ice-water bath with rapid stirring until a Ca to P of 1.67 was obtained. Variables examined in Part I of the synthesis method were precursor salts (Section 2.3.1.1), reaction time (Section 2.3.1.2), and volume of the reaction (Section 2.3.1.3).

2.3.1.1 Precursor Salts

The effect of the precursor salts on the precipitate was examined through conducting precipitation reactions with four combinations of reactants: A) $CaCl_2 \cdot 2H_2O$ with Na_2HPO_4, B) $CaCl_2 \cdot 2H_2O$ with $(NH_4)_2HPO_4$, C) $Ca(NO_3)_2 \cdot 4H_2O$ with Na_2HPO_4, and D) $Ca(NO_3)_2 \cdot 4H_2O$ with $(NH_4)_2HPO_4$ (Table 2.1). Reactions were conducted as described in Section 2.3.1. 300 mL of 10 mM phosphate solution was added drop-wise to 500 mL of 10 mM Ca solution under rapid stirring for final concentrations of 6.25 mM calcium and 3.75 mM P in a total volume of 800 mL. Precipitate was removed from solution after 26 hrs, then washed and dried as described in Section 2.3.2.1. These precipitates will be referred to as A26, B26, C26, and D26. Further discussion of reactions will be referred to by the reactant combination IDs assigned in Table 2.1.

Table 2.1: List of calcium and phosphate salt precursor combinations for precipitation reaction

Reactant pair ID	**Calcium Salt**	**Phosphate Salt**
A	$CaCl_2$	Na_2HPO_4
B	$CaCl_2$	$(NH_4)_2HPO_4$
C	$Ca(NO_3)_2$	Na_2HPO_4
D	$Ca(NO_3)_2$	$(NH_4)_2HPO_4$

2.3.1.2 Reaction Time

The effect of the stirring time (3, 26, and 72 hours) was evaluated for reactions A and D from Section 2.3.1.1. Precipitate was removed, then washed and dried as described in Section 2.3.2.1. Reaction conditions are summarized in Table 2.2.

Table 2.2: Summary of precipitation of calcium phosphate with different stirring times

Sample ID	**Reactants (Table 2.1)**	**Stir Time [Hr]**
A3	A	3
A26	A	26
A72	A	72
D3	D	3
D26	D	26
D72	D	72

2.3.1.3 Reaction Volume

The effect of changing reaction volume was examined for reactant pair A. Precipitate A3 from Section 2.3.1.3 was obtained from a reaction volume of 800 mL after 3 hrs of the reaction (A3-800mL). Precipitate A3-800mL was compared to precipitate obtained from a similar reaction with a smaller volume. Briefly, 90 mL of 10 mM Na_2HPO_4 was added drop-wise into a solution of 150 mL of 10 mM $CaCl_2$ for a total reaction volume of 240 mL. Precipitate was removed after 3 hrs of the reaction (A3-240mL) and dried as described in Section 2.3.2.1.

2.3.2 Step II: Post-processing Methods of Precipitated HA Nanoparticles from 2.3.1

2.3.2.1 Drying & Storage

Precipitates prepared as described in Section 2.3.1.1 were concentrated into 50 mL centrifuge tubes (Thermo Scientific Sorvall legend RT+, Thermo Scientific, 3,600 g, 7 min) and supernatant removed after precipitate formed a pellet. The pellet was re-suspended in 15 mL of 0.1 M NH_4OH and centrifuged at 3,600 g for 7 min, twice. Supernatant was removed after each centrifuge cycle. The pellet was re-suspended in acetone and centrifuged a final time. The pellet was spread onto glass slides and allowed to air dry for two days before storage in sealed 20 mL scintillation vials.

2.3.2.2 Dry Annealing

HA precipitates A26, A72, D26, and D72 (Table 2.2) were dried as described in Section 2.3.2.1. The dried precipitates were then annealed in an oven (GS Blue M Electric model no. OV12A, 200 °C in air) for different durations of time. After the heating period, precipitates were allowed to cool to room temperature before storage in 20 mL scintillation vials. A summary of the annealing times for A26 and D26 particles is listed in Table 2.3 and for A72 and D72 particles in Table 2.4.

Table 2.3: Summary of precipitates stirred for 26 hrs followed by dry-annealing periods

Sample ID	**Step I Precipitate (Table 2.2)**	**Annealing Time [Day]**
A26-A0	A26	0
A26-A48	A26	48
D26-A0	D26	0
D26-A48	D26	48

Table 2.4: Summary of precipitates stirred for 72 hrs followed by dry-annealing periods

Sample ID	**Step I Precipitate (Table 2.2)**	**Annealing Time [Day]**
A72-A0	A72	0
A72-A24	A72	24
A72-A72	A72	72
D72-A0	D72	0
D72-A0.5	D72	0.5
D72-A48	D72	48
D72-A120	D72	120

2.3.2.3 Hydrothermal Aging

Calcium phosphate precipitates were taken from the precipitation reactions and placed into a pressure vessel (Parr Instrument Company 276AC-7304). Two different procedures were followed: Preparation I – a 15 mL aliquot was taken directly from the reaction solution and

Preparation II – a 45 mL aliquot from the reaction solution was concentrated by allowing the precipitate to settle by gravity and decanting the solution into a 15 mL volume. Solutions were hydrothermally aged in the pressure vessel at 180 °C for various amounts of time. A combination of reactant concentrations and aging times was examined. Preliminary work used precipitate obtained from reaction conditions modified from the synthesis method developed by Tao without addition of poly(acrylic acid) [27]. Briefly, 40 mL of 66 mM Na_2HPO_4 was added drop-wise into 400 mL of 11 mM $CaCl_2$ under rapid stirring. All other reaction parameters followed those described in Section 2.3.1. Reaction was stirred for 12 hrs before taking a 15 mL aliquot from the reaction (Preparation I) and hydrothermally aging the aliquot for 0.25, 0.5, 0.72, and 1 hr. Similarly, 40 mL of 660 mM Na_2HPO_4 was added drop-wise into 400 mL of 110 mM $CaCl_2$ under rapid stirring to examine changes with reactant solution concentration. Reaction was stirred for 12 hrs before hydrothermally aging a 15 mL aliquot (Preparation I) for 2.16 and 5.7 hrs (Table 2.5). Particles were removed from the pressure vessel and dried as described in Section 2.3.2.1.

Table 2.5: Summary of hydrothermally aged precipitate using Preparation I

ID	Sample ID	Calcium Conc. [mM]	Phosphate Conc. [mM]	Hydrothermal Aging Time [hr]
1	A12-H0.25	11	66	0.25
2	A12-H0.5	11	66	0.5
3	A12-H0.75	11	66	0.75
4	A12-H1	11	66	1
5	A12-H2.16	110	660	2.16
6	A12-H5.7	110	660	5.7

Precipitates obtained from different reaction conditions were also hydrothermally aged to examine the effect of precursor salt and changing the concentration of the precipitates before hydrothermal aging [16]. Precipitate was obtained from reactants D, where 90 mL of 10 mM $(NH_4)_2HPO_4$ was added drop-wise into a solution of 150 mL 10 mM $Ca(NO_3)_2$ and stirred for 13 hrs. Precipitate from these reactions were concentrated 3-fold by centrifugation of 45 mL aliquots and decanted for a total volume of 15 mL (preparation II). Precipitate was re-suspended by sonicating for 30 min (Bransonic 1510R-MT) before hydrothermal aging in the pressure vessel at 180 °C (Table 2.6). Particles were dried following Section 2.3.2.1.

Table 2.6: Summary of hydrothermally aged precipitate from preparation II

ID	Sample ID	Calcium Conc. [mM]	Phosphate Conc. [mM]	Hydrothermal Aging Time [hr]
1	D13-H0	10	10	0
2	D13-H0.5	10	10	0.5
3	D13-H72	10	10	72

2.3.2.4 Dialysis

Precipitate was obtained from reaction of 300 mL 10 mM $(NH_4)_2HPO_4$ added drop-wise into 500 mL of 10 mM $Ca(NO_3)_2$ of 10 mM under rapid stirring. Reaction was allowed to stir for 48 hrs and concentrated 4 times by decanting the solution after allowing precipitate to settle for 30 min. Remaining solution was placed into DI-H_2O hydrated dialysis bags (Cellu®SepT1 Part 5030-46, MWCO 3,500). Precipitate was dialyzed in 0.1 M NaOH over 3 days with NaOH

solutions replaced every day. The precipitate was then further concentrated into 30 mL volumes and stored in scintillation flasks.

2.3.3 Nanoparticle Analysis

Powder x-ray diffraction (pXRD) was used to identify the crystal phase of the particles (Scintag Inc. PAD-X theta-theta X-ray Diffractometer, CuKα 1.54 Å, accelerating voltage 45 kV, current 40 mA, continuous scan, 2.0 deg/min). The pXRD patterns were matched by Miller indices and peak identification cards from the ICCD database [28]. Samples were then combined with KBr and pressed into pellets for transmission FTIR (Mattson Instruments 2020 Galaxy Series FT-IR) to obtain FTIR spectra (res 4.0 cm^{-1}, 64 scans). Particle crystallinity was determined qualitatively from sample splitting factor calculated following the method developed by Weiner and Bar-Yosef modified from the methods developed by Termine and Posner, and Blumenthal and Posner [29-31] as follows:

$$SF = \frac{A_1 + A_2}{A_3} \qquad (2.1)$$

where *SF* is the splitting factor determined by the sum of the intensities at peaks 602 cm^{-1} (A_1) and 563 cm^{-1} (A_2) divided by the intensity of the minima between the two peaks (A_3). The morphology of the particles was examined via TEM. Particles were combined with ethanol and dripped onto carbon-coated copper grids (Electron Microscopy Sciences) and examined with brightfield TEM (FEI Tecnai T-12 Spirit, 120 kV).

2.4 Results

2.4.1 Effect of Precursor Salt on Precipitate

To examine the relevance of precursor salts on precipitate formation, reactions of four different combinations of Ca and P precursors were examined. Reactions using Na_2HPO_4 (reactant combination A and C, Table 2.1) as the P source yielded precipitate with plate-like morphologies and reactions using $(NH_4)_2HPO_4$ (reactant combination B and D, Table 2.1) yielded precipitate with smaller, rounded particles regardless of which calcium precursor was used (Fig. 2.1). The phase of the precipitate differed for different combinations of reactants with all other conditions kept the same. Reactions from combination A and C were identified as dicalcium phosphate dihydrate (DCPD, brushite, chemical formula $Ca(HPO_4)•2(H_2O)$), with the presence of some HA, reaction combination B yielded ACP, and reaction combination D yielded HA (Fig. 2.2).

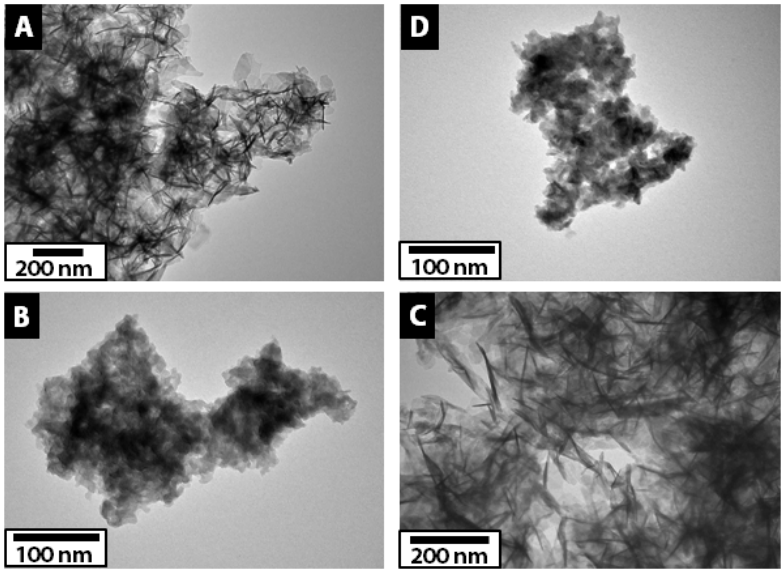

Figure 2.1: TEM micrographs of precipitates obtained from reaction of $CaCl_2$ with Na_2HPO_4 (A), $CaCl_2$ with $(NH_4)_2HPO_4$ (B), $Ca(NO_3)_2$ with Na_2HPO_4 (C), and $Ca(NO_3)_2$ with $(NH_4)_2HPO_4$.

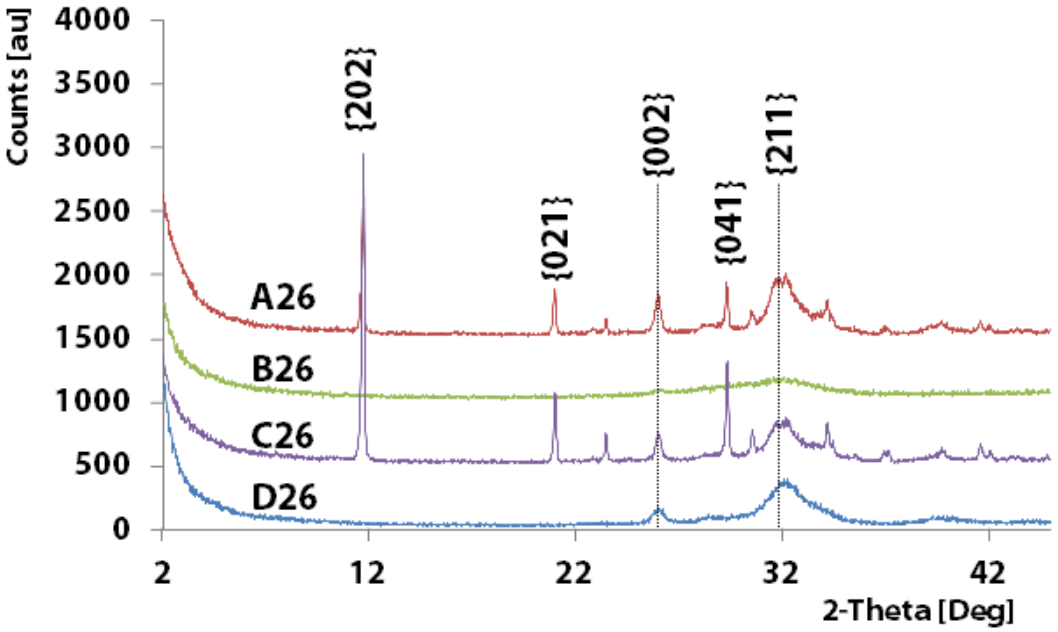

Figure 2.2: pXRD of precipitate A26, B26, C26, and D26 of Section 2.3.11. Typical indices for brushite were placed above corresponding peaks (ICDD PDF 11-293). Miller indices for hydroxyapatite are designated by lines above peaks (ICDD PDF 09-0432) [28].

Further work to examine the effect of pH on the reaction was conducted by Wangzhong Sheng [see Wangzhong Sheng Senior Thesis]. Sheng observed that the phosphate cations played a major role in regulating pH at the start of the reaction, which affects the initial morphology and phase of the precipitate and that these differences could be minimized if pH was maintained through the course of the reaction.

2.4.2 Reaction Duration

It was observed that changing the duration of reaction stirring time had an effect on the phase of the precipitate. For reaction A, precipitate removed from solution at 3 hrs was identified to be DCPD via pXRD. Removal from solution at 26 hrs showed a mixture of CaP phases of DCPD and HA. After 72 hrs, the precipitate is completely HA (Fig. 2.3).

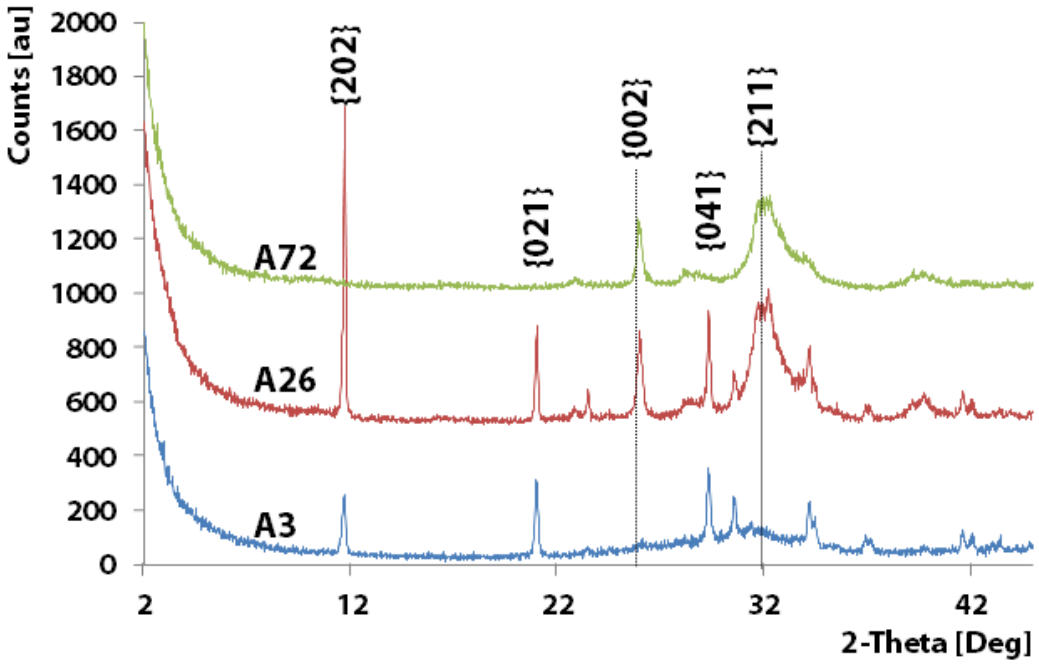

Figure 2.3: pXRD patterns of 800 mL reactions of A stirred for 3 (A3), 26 (A26), and 72 (A72) hrs. Typical indices for brushite were placed above corresponding peaks. Miller indices for hydroxyapatite are designated by lines above peaks.

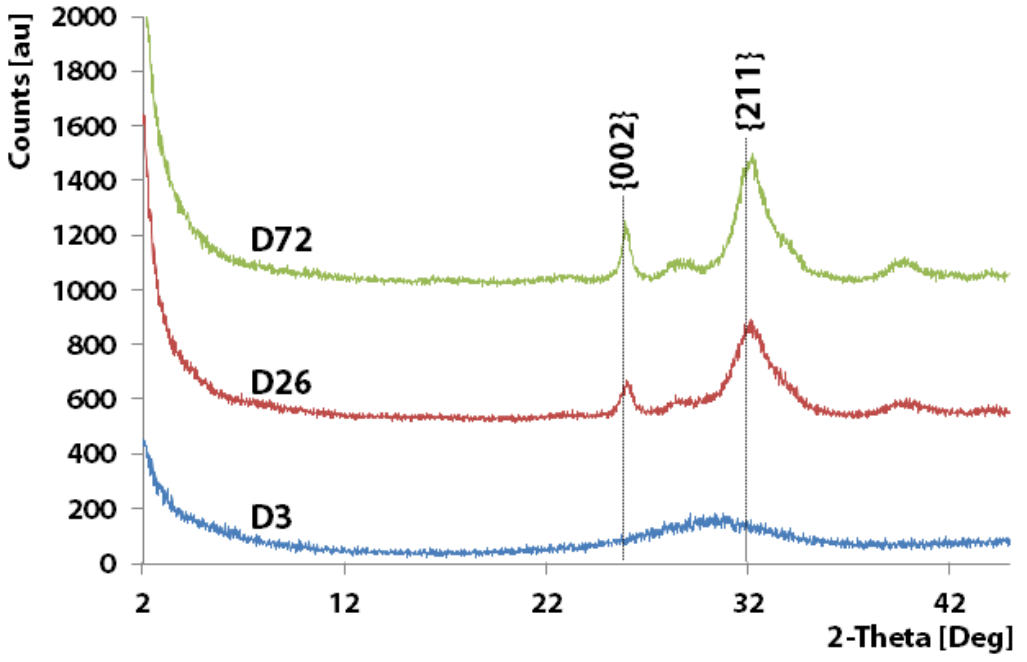

Figure 2.4: pXRD patterns of 800 mL reactions of D stirred for 3 (D3), 26 (D26), and 72 (D72) hrs. Typical indices for hydroxyapatite are designated by lines above peaks.

The change in phase with increased stirring time is also observed for reaction D (Table 2.1) where at 3 hrs, the precipitate was identified as ACP and after 26 hrs, identified as HA (Fig. 2.4).

2.4.3 Reaction Volume

For reactions conducted at smaller volumes, but similar conditions, lower amounts of product were obtained and less reaction time was required for the precipitate phase to become HA. For example, A3-800mL was a mixture of CaP phases, while A3-240mL was only HA (Fig. 2.5). The reagent concentrations and stirring times were identical for these two reactions.

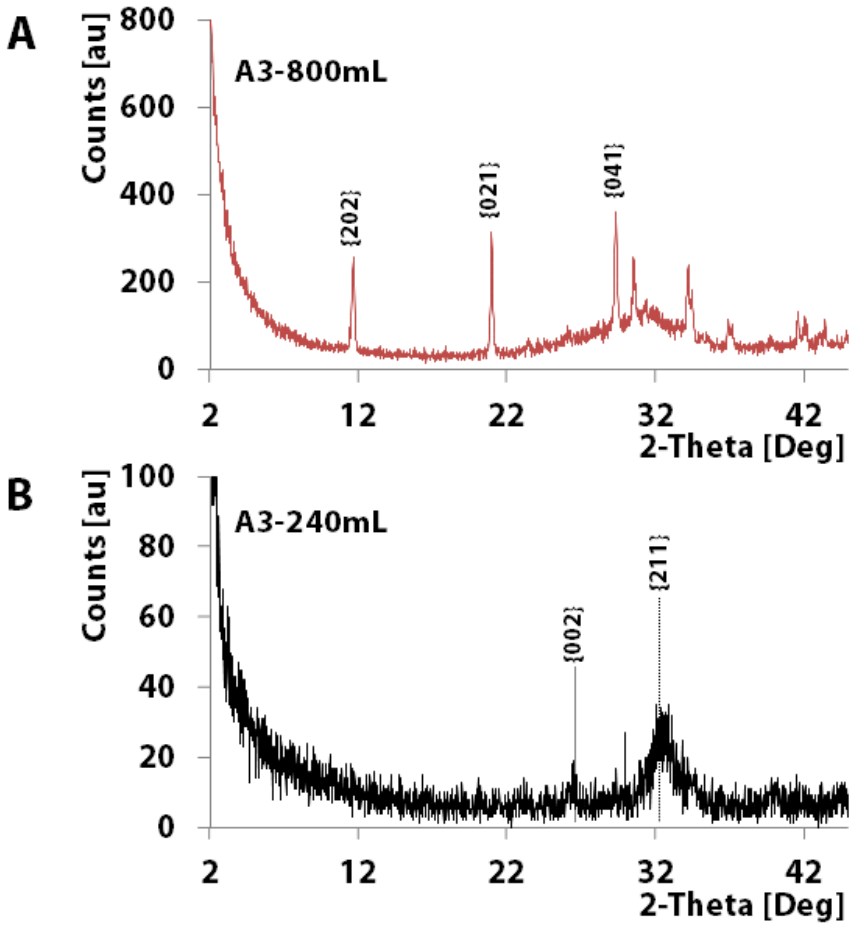

Figure 2.5: pXRD patterns of reactions of A stirred for 3 hrs with reaction volume of 800 mL (A3-800mL) and 240 mL (A3-240mL). Typical indices for hydroxyapatite are designated by lines above peaks and indices for brushite labeled above the peak.

2.4.4 Dry Annealing

Air-dried precipitate was heated at 200 ºC in air at atmospheric conditions. Annealing of precipitate that was identified as HA did not change the phase of the precipitate (Fig. 2.6B, Fig. 2.7, Fig. 2.8), however if the precipitate contained DCPD, DCPD peaks disappeared after 2 days of annealing, transforming the phase of the precipitate to HA (Fig. 2.6A).

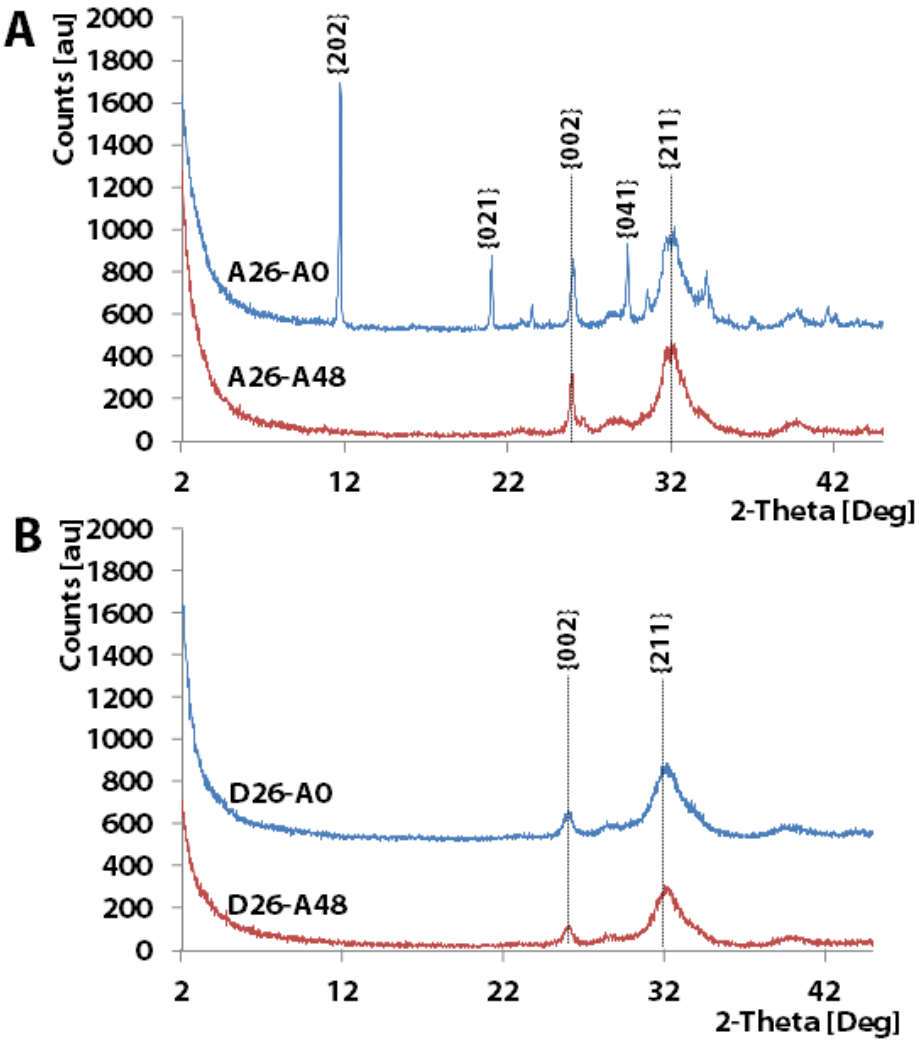

Figure 2.6: pXRD patterns of precipitate from 800 mL reactants A stirred for 26 hrs and then dry annealed for 0 (A26-A0) and 48 (A26-A48) hrs (A) and reactants D stirred for 26 hrs and then dry annealed for 0 (D26-A0) and 48 (D26-A48) hrs (B). Peak indices for brushite are labeled above peaks and indices for HA indicated by dotted lines.

For HA precipitates, dry annealing maintains the phase as HA (Fig. 2.7, Fig. 2.9). From calculating the FTIR splitting factor at the phosphate v_4 peaks at 602 cm^{-1} and 563 cm^{-1} as described in Section 2.3.3, an increase in splitting factor is observed for both reactions through day 3 for A72 particles and day 2 for D72 particles (Fig. 2.8, Fig. 2.10). The changes in splitting factor for D72 particles are smaller than for A72 particles. A decrease in splitting factor is observed for D72 particles on day 5. These results suggest an increase in crystallinity with initial heat treatment, but with extended heating time, the material may become more disordered. Furthermore, regardless of annealing time, the splitting factor values for A72 particles were greater than D72 particles. TEM micrographs of precipitates of A26 and D26 (Fig. 2.1) showed that precipitates obtained from A were larger than precipitates obtained from reactions of D. The increased size of A precipitates may contribute to the increase in splitting factor due to larger coherence lengths within the particles.

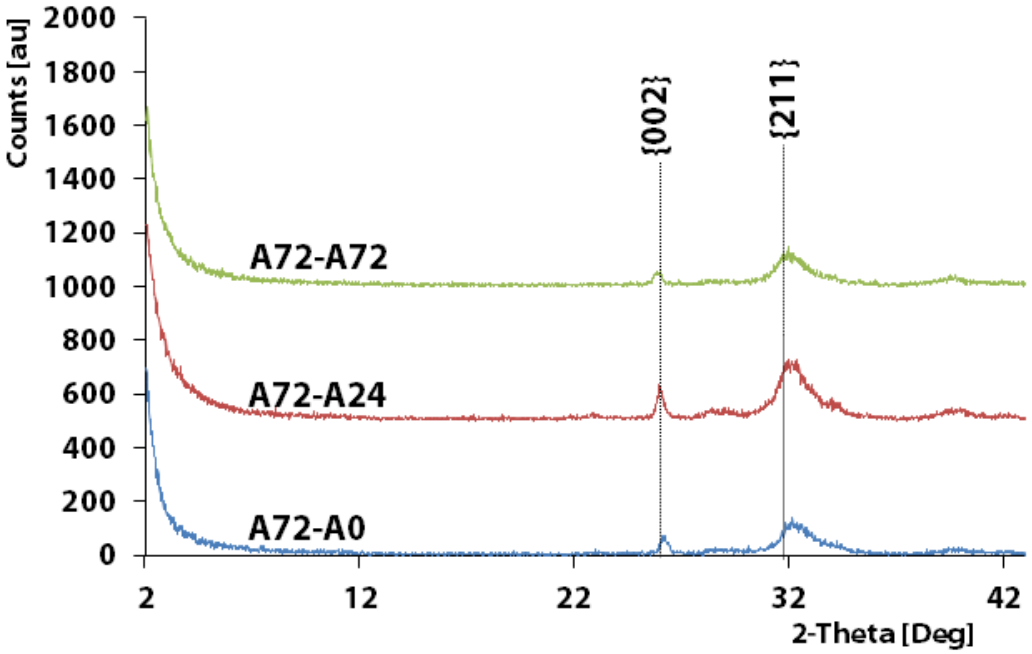

Figure 2.7: pXRD pattern of reactants A after 72 hrs stirring, reacted at 800 mL, air dried, then dry annealed for 0 (A72-A0), 1 (A72-A24), and 3 (A72-A72) hrs, bottom to top. Hydroxyapatite Miller indices are indicated by the dotted lines.

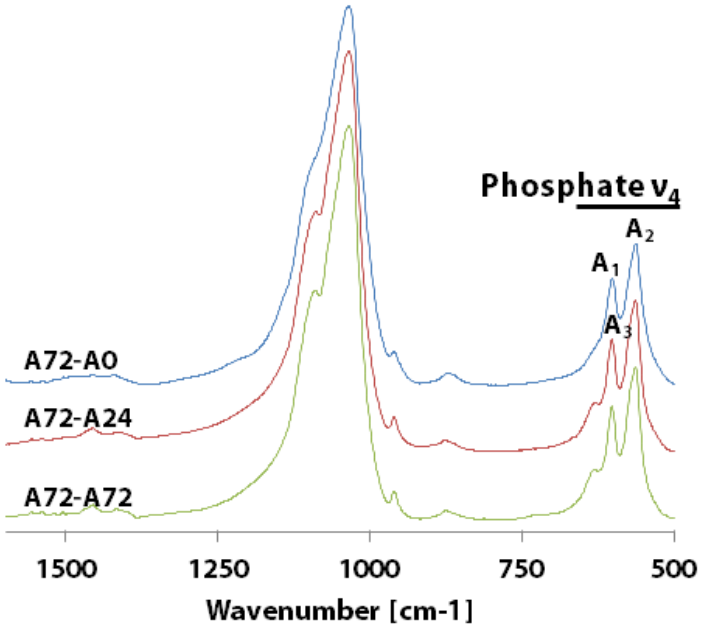

Sample ID	Splitting Factor
A72-A0	3.8
A72-A24	4.1
A72-A72	4.2

Figure 2.8: FTIR of precipitate A72 hrs, reacted at 800 mL, air dried, then dry annealed for 0 (A72-A0), 1 (A72-A24), and 3 (A72-A72) hrs (top to bottom). Splitting factors calculated from phosphate v_4 peaks by calculating the ratio of the sum of intensities at A_1 and A_2 over A_3.

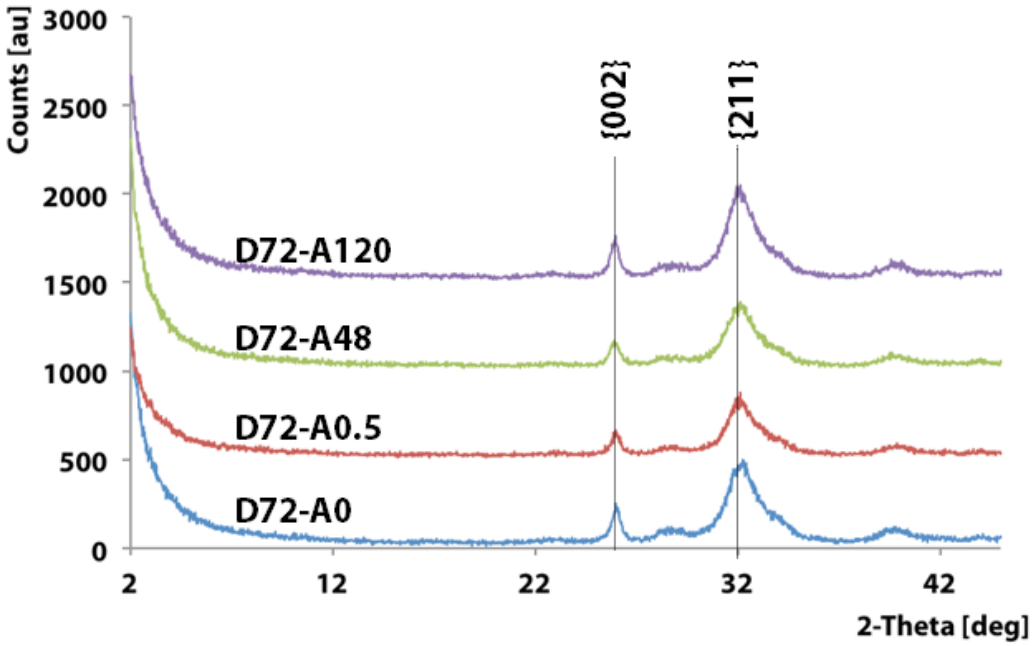

Figure 2.9: pXRD pattern of precipitate D72, reacted at 800 mL, air dried, then dry annealed for 0 (D72-A0), 0.5 (D72-A0.5), 2 (D72-A48), and 5 (D72-A120) hrs bottom to top. Hydroxyapatite Miller indices are indicated by the dotted lines.

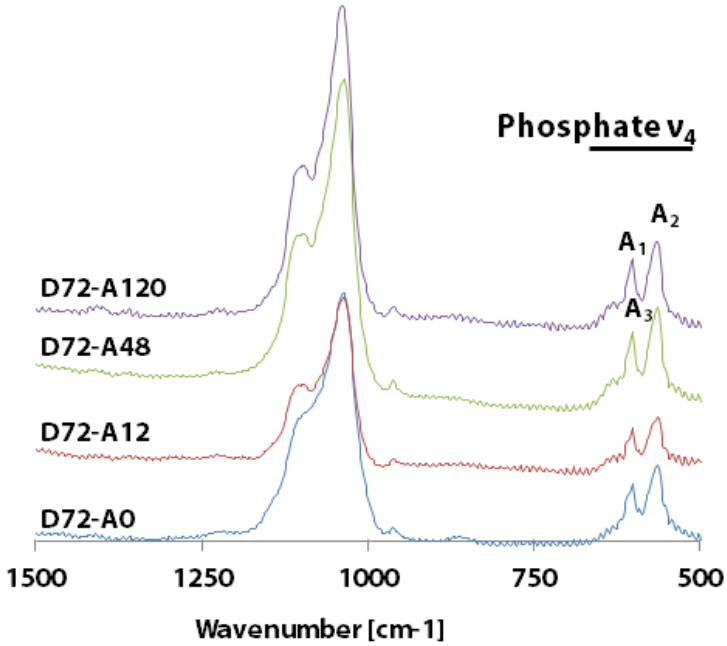

Sample ID	Splitting Factor
D72-A0	2.6
D72-A0.5	2.7
D72-A48	2.7
D72-A120	2.6

Figure 2.10: FTIR spectra of precipitate D72 dry annealed for 0 (D72-A0), 0.5 (D72-A0.5), 2 (D72-A48), and 5 (D72-A120) hrs with a list of the splitting factor calculated from phosphate v_4. Splitting factors calculated from phosphate v_4 peaks by calculating the ratio of the sum of intensities at A_1 and A_2 over A_3.

2.4.5 Hydrothermal Aging

Precipitates from reactions A and D were taken as 15 mL aliquots (Preparation I) or concentrated 15 mL aliquots from decanting the solution (Preparation II) before being placed into a pressure vessel and aged for various durations of time at 180 °C. Hydrothermal synthesis of hydroxyapatite generally occurs in one step where Ca and P precursor salts are mixed in the pressure vessel and heated [18, 22]. Separating the precipitation process from the aging process allows for better control of HA sizes as the nucleation of HA is separated from the growth of the particle and results in more uniform growth of the particles. With increasing hydrothermal aging times, particles grow in size preferentially along the c-axis indicated by the decrease in peak broadening and increased intensity of the {002} peak (Fig. 2.11). The appearance of more well-defined diffraction peaks also indicate that crystallinity increases with hydrothermal aging time.

Additionally, CaP phases that were not pure HA could be transformed to HA with increased hydrothermal aging time. Figure 2.12 shows the progression of DCPD and HA precipitate transforming to pure HA with increased hydrothermal aging time. For samples of HA obtained from hydrothermally aging precipitate containing DCPD, a sharp peak is observed to form to the right of the {002} of HA in samples A12-H.5 through A12-H5.7. Similar peaks have been observed in literature for Ca-deficient HA formed from DCPD precursors [32]. This secondary peak is not observed for hydrothermally aged particles from D reactants (Fig. 2.11).

TEM images of the precipitates obtained through hydrothermal aging are presented in Figure 2.13. With increased hydrothermal aging time, particles become more rod-like in nature. Concentrating the amount of precipitate before hydrothermal aging still allowed for the formation of discrete and elongated particles. By increasing the concentration of the precipitation reaction, larger and more elongated particles could be produced (Fig. 2.13 E, F). However, concentration increase also supported formation of other CaP phases such as DCPD.

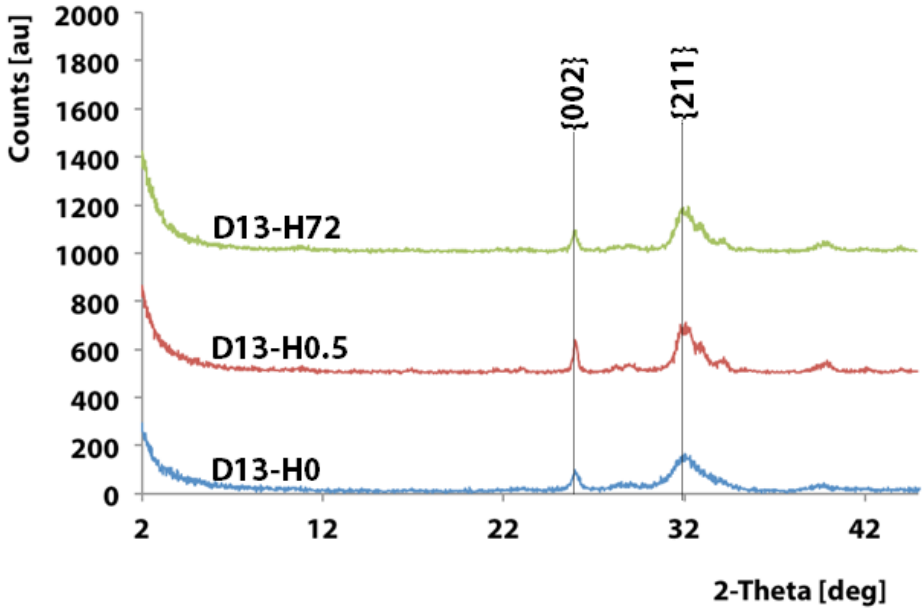

Figure 2.11: pXRD of reaction of D stirred for 13 hrs then hydrothermally aged for 0 (D13-H0), 0.5 (D13-H0.5), and 72 (D13-H72) hrs. Hydroxyapatite Miller indices labeled at peaks.

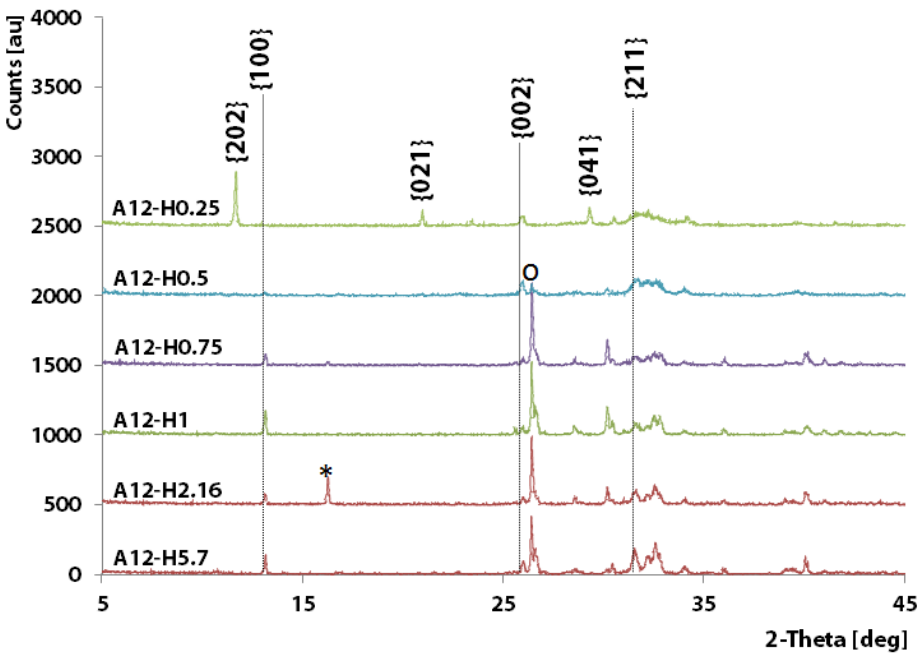

Figure 2.12: pXRD of precipitate after hydrothermal aging from Table 2.5. Peak indices for brushite are labeled above peaks and indicated by dotted lines for hydroxyapatite (HA). (*) – Signal from quartz sample holder. (°) - Peak for HA synthesized from brushite precursor.

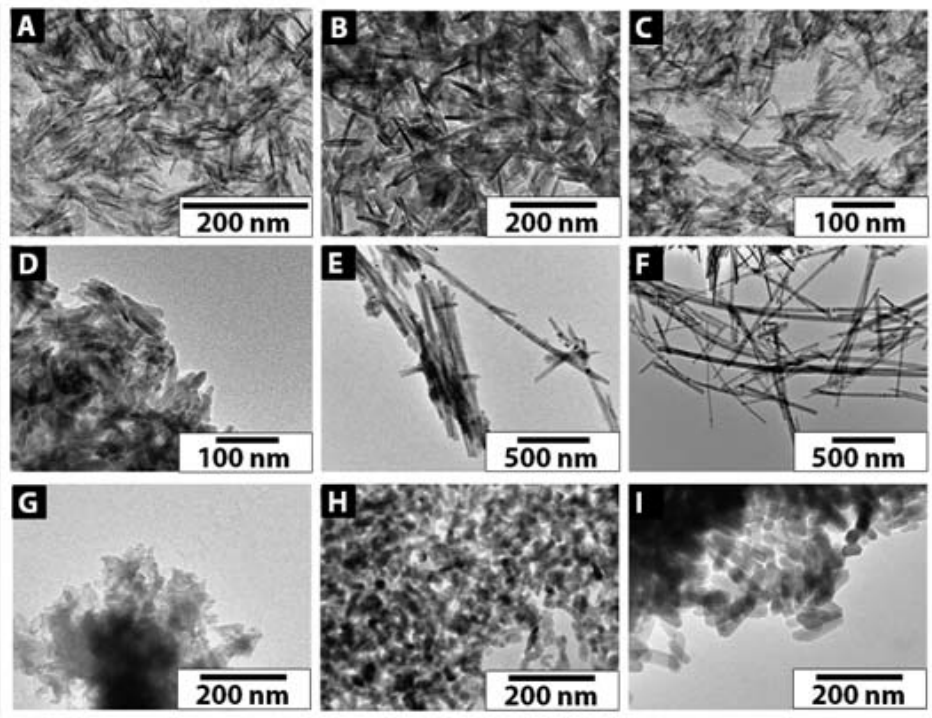

Figure 2.13: TEM micrographs of hydrothermally aged HA particles obtained from parameters 1-6 of Table 2.5 (A-F) and of parameters 1-3 of Table 2.6 (G-I).

2.4.6 Dialysis

For applications where the dispersion of HA is important, dried particles tend to aggregate and settle out of solution. Keeping the particles in solution through dialysis can improve HA nanoparticle dispersion into viscous materials such as collagen gels before setting. To improve HA dispersion into gels, the precipitate was kept in the reaction solution, concentrated by decanting the solution after precipitate settled, and then dialyzed against 0.1 M NaOH. Using this technique, particles remained in an aqueous environment throughout the whole process. Additionally, mineral crystals were elongated (Fig. 2.14A) compared to the precipitate obtained after removal from reaction solution, washed and dried in air (Fig. 2.14B).

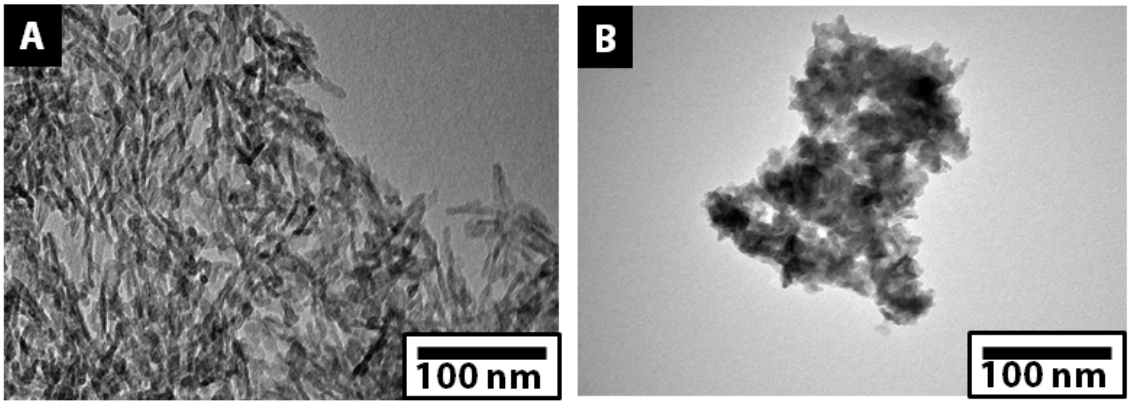

Figure 2.14: TEM micrographs of precipitate from reaction A after 48 hrs of stir dialyzed into 0.1 M NaOH for 3 days (A) and precipitate dried after 48 hr stir.

In work to incorporate HA particles into collagen gels [33], it was observed by optical light microscopy that HA particles dialyzed against 0.1 M NaOH have better dispersion within the gel with less visible HA aggregates (Fig. 2.15A) while gels mixed with dried HA particles have many HA aggregates visible by optical microscope (Fig. 2.15B).

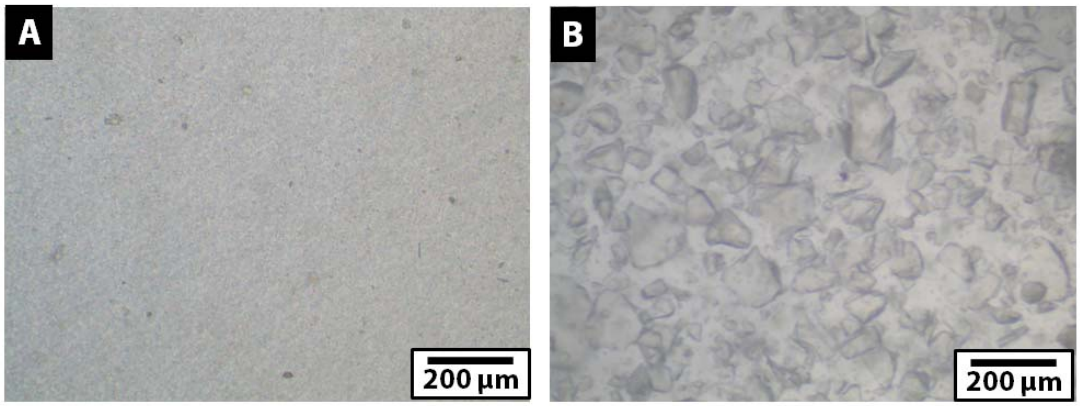

Figure 2.15: Optical light micrographs of collagen gels mixed with HA precipitate from reactants D dialyzed in 0.1 M NaOH (A) and mixed with dried H precipitate (B) Courtesy of Jen Richards [33].

2.5 Discussion

One of the most common ways of synthesizing HA is through the co-precipitation of Ca and P salts in aqueous solutions with molar concentrations of Ca to P equal to 1.67 following variations of the method developed by Tsilieus [34]. Although this process appears straightforward, there are numerous modifications of the Tsilieus method to synthesize hydroxyapatite through aqueous precipitation [23, 35, 36]. These recipes can differ by reactants, concentration, reaction time, temperature, and pH. In this study, several parameters were kept consistent to minimize complexity. Precursor salts were limited to $Ca(NO_3)_2 \cdot 4H_2O$ and $CaCl_2 \cdot 2H_2O$ as the Ca source and Na_2HPO_4 and $(NH_4)_2HPO_4$ as the P source. Reactant solutions were pH balanced to 9.5, filtered to removal potential heterogeneous nucleation sites, and mixed in a drop-wise fashion at an initial temperature of 4 °C in an ice-water bath under rapid stirring. Further stirring was conducted at room temperature. Changes in ionic strength and pH variations over the course of the reaction were not controlled.

Although the pH of the starting reactants was kept at pH 9.5, the pH of the reacting solution changes during the course of the reaction. These changes are dependent in part on the reactants used and are linked with the rate of the reaction [37, 38]. For reactions containing sodium phosphate, HA particles tend to appear more plate-like while reactions containing ammonium phosphate have a rounded morphology. These differences are tied to the influence on pH of the P counterion rather than C, however other studies have indicated that the presence of chloride increases the formation of plate-like HA [39].

In addition to reactants and pH, the reaction volume also plays a role in the phase of the resulting precipitate as demonstrated by reacting Na_2HPO_4 with $CaCl_2$ at reaction volumes 240 mL and 800 mL. Increasing the reaction volume favors the formation of kinetic CaP products such as DCPD or ACP, over the thermodynamic product, HA. Phosphate was added drop-wise into the Ca solution under rapid stirring. Even with the stirring, such an addition process leads to localized areas of high concentration before dilution into the bulk. These mixing conditions result in local changes in supersaturation and ion speciation over the duration of the reaction. Such variations are greatly reduced in more controlled systems such as titration and constant composition methods [40, 41]. The effects of the mixing conditions are amplified for larger volumes since the stirring is not sufficient to reach homogeneous solutions rapidly. With addition of P to Ca, localized areas within the reaction flask are at higher P to Ca ratios than those favorable for HA, and favor the formation of Ca-deficient, kinetic products. By increasing the stirring time in solution, these precipitates are able to hydrolyze into Ca-deficient HA. Similar trends are also reported in the literature for increases in reactant concentrations [42]. With increasing reactant concentrations, the resulting precipitate may contain mixtures of ACP or DCPD with HA [38, 43].

Although not examined in this thesis chapter, the order of addition of the reactants has been show to affect the size and Ca to P ratio of resulting precipitate [44, 45]. Calcium solutions added into phosphate solutions often yielded ACP at concentrations above 10 mM [46]. Phosphate solutions added to calcium solutions were observed to produce DCPD in addition to HA and yield smaller precipitate particles [37, 45]. In this work, precipitation reactions were consistently conducted by adding P solutions to the Ca solution.

Post-processing methods such as dry annealing, hydrothermal aging, and dialysis can further tune the properties of the HA precipitates obtained from precipitation reactions. Through dry annealing, the morphology of the particles is maintained while non-HA phases can be converted to HA and particles of HA can have changes in crystallinity. Water must be present to facilitate these changes [47, 48]. Further discussion on the effects of dry annealing of HA precipitate are discussed in Chapter 3. Hydrothermal aging changes the morphology and crystallinity of the precipitate while yielding particles with narrow size distributions [16, 49]. Further discussion of hydrothermal gaining is discussed in Chapter 4. Dialysis of precipitate from the reaction solution into other solutions can affect the morphology of the precipitate and also improve incorporation of the HA particles into aqueous media such as collagen hydrogels. Dividing the synthesis method of HA particles into two steps starting with the initial precipitation reaction followed by post-processing techniques allows for multiple points to fine tune HA properties during the synthesis process without the use of additional additives or fractionation techniques.

2.6 Conclusions

Conducting the synthesis of HA particles through two-step processes by forming the precipitate followed by different processing techniques allows for fine-tuning the formation of HA nanoparticles. Through these techniques, a wide range of HA nanoparticles can be obtained with defined size, shape, and crystallinities, which allows for the study of specific HA properties. Furthermore, these nanoparticles can be introduced into culture systems to examine cell-mineral interaction. In the following chapters, Chapter 3 reports a method to present dry annealed HA particles (Section 2.3.2.2) onto glass substrates for culture with primary human osteoblasts to examine how changes in HA from dry-annealing can affect OB response. Chapter 4 utilizes hydrothermally aged HA particles to investigate how changes in size and crystallinity can effect bone metastatic response of breast cancer cells in 3-D porous scaffolds.

References

[1] Weiner S, Wagner HD. The material bone: structure-mechanical function relations. Ann Rev Mat Sci 1998;28:271-98.

[2] Weiner S, Veis A, Beniash E, Arad T, Dillon JW, Sabsay B, Siddiqui F. Peritubular dentin formation: crystal organization and the macromolecular constituents in human teeth. J Struc Biol 1999;126:27-41.

[3] Weska Rf, Aimoli CG, Noqueira GM, Leirner AA, Maizato MJ, Jiga OZ, Polakievicz B, Pitombo RN, Beppu MM. Natural and prosthetic heart valve calcification: morphology and chemical composition characterization. Artif Organs 2010;34(4):311-8.

[4] Lee YS. Morphogenesis of calcification in porcine bioprosthesis: insight from high resolution electron microscopic investigation at molecular and atomic resolution. J Electron Microsco 1993;42(3):156-65.

[5] Lange C, Li C, Manjubala I, Wagermaier W, Kuhnisch J, Kolanczyk M, Mundios S, Knaus P, Fratzl P. Fetal and postnatal mouse bone tissue contains more calcium than is present in hydroxyapatite. J Struc Biol 2011;176(2):159-67.

[6] Kuhn LT, Grynpas MD, Rey C, Wu Y, Ackerman JL, Glimcher MJ. A comparison of the physical and chemical differences between cancellous and cortical bovine bone mineral at two ages. Calcif Tissue Int 2008;83(2):146-54.

[7] Boskey AL. Bone mineral crystal size. Osteoporosis International 2003;14:S16-20.

[8] Rohanizadeh R, LeGeros RZ, Bohic S, Pilet P, Barbier A, Daculsi G. Ultrastructural properties of bone mineral of control and tiludronate-treated osteoporotic rat. Calcif Tissue Int 2000;67:330-6.

[9] Donnelly E, Meridth DS, Ngyuyen JT, Gladnick BP, Rebolledo BJ, Shaffer AD, Lorich DG, Lane JM, Boskey AL. Reduced cortical bone compositional heterogeneity with bisphosphonate treatment in postmenopausal women with intertrochanteric and subtrochanteric fractures. J Bone Min Res 2012;27(3):672-8.

[10] Balasundaram G, Sato M, Webster TJ. Using hydroxyapatite nanoparticles and decreased crystallinity to promote osteoblast adhesion similar to functionalizing with RGD. Biomaterials 2006;27(14):2798-805.

[11] Pathi SP, Kowalczewski C, Tadipatri R, Fischbach C. A novel 3-d mineralized tumor model to study breast cancer bone metastasis. PLoS One 2010;5(1):e8849.

[12] Sun JS, Tsuang YH, Liao CJ, Liu HC, Hang YS, Lin FH. The effects of calcium phosphate particles on the growth of osteoblasts. J Biomed Mater Res 1997;37(3):324-34.

[13] Nagano M, Nakamura T, Kokubo T, Tanahashi M, Ogawa M. Differences of bone bonding ability and degradation behaviour in vivo between amorphous calcium phosphate and highly crystalline hydroxyapatite coating. Biomaterials 1996;17(18):1771-7.

[14] Detsch R, Mayr H, Ziegler G. Formation of osteoclast-like cells on HA and TCP ceramics. Acta Biomaterialia 2008;4(1):139-48.

[15] Lundqvist M, Stigler J, Elia G, Lynch I, Cedervall T, Dawson KA. Nanoparticle size and surface properties determine the protein corona with possible implications for biological impacts. Proc Natl Acad Sci U S A 2008;105(38):14265-70.

[16] Pathi SP, Lin DW, Dorvee JR, Estroff LA, Fischbach C. Hydroxyapatite nanoparticle-containing scaffolds for the study of breast cancer bone metastasis. Biomaterials 2011;32(22):5112-22.

[17] Kim HW, Kim HE, Salih V. Stimulation of osteoblast responses to biomimetic nanocomposites of gelatin-hydroxyapatite for tissue engineering scaffolds. Biomaterials 2005;26:5221-30.

[18] Liu H, Yazici H, Ergun C, Webster Tj, Bermek H. An in vitro evaluation of the Ca/P ratio for the cytocompatibility of nano-to-micron particulate calcium phosphate for bone regeneration. Acta Biomater. 2008;4:1472-9.

[19] Sawyer AA, Hennessy KM, Bellis SL. The effect of adsorbed serum proteins, RGD and proteoglycan-binding peptides on the adhesion of mesenchymal stem cells to hydroxyapatite. Biomaterials 2007;28(3):383-92.

[20] Woo KM, Seo J, Zhang R, Ma PX. Suppression of apoptosis by enhanced protein adsorption on polymer/hydroxyapatite composite scaffolds. Biomaterials 2007;28(16):2622-30.

[21] Gilbert M, Shaw WJ, Long JR, Nelson K, Drobny GP, Giachelli CM, Stayton PS. Chimeric peptides of statherin and osteopontin that bind hydroxyapatite and mediate cell adhesion. J Biol Chem 2000;275(21):16213-8.

[22] Conz MB, Granjeiro JM, Soares GdA. Physicochemical characterization of six commercial hydroxyapatites for medical-dental applicatons as bone graft. J App Oral Sci 2005;13:136-40.

[23] Dorozhkin SV. Nanosized and nanocrystalline calcium orthophosphates. Acta Biomaterialia 2010;6(3):715-34.

[24] Cai YR, Tang RK. Calcium phosphate nanoparticles in biomineralization and biomaterials. J Mat Chem 2008;18(32):3775-87.

[25] Cunniffe GM, O'Brien FJ, Partap S, Levingstone TJ, Stanton KT, Dickson GR. The synthesis and characterization of nanophase hydroxyapatite using a novel dispersant-aided precipitation method. J Biomed Mat Res Part A 2010;95A(4):1142-9.

[26] Martins MA, Santos C, Almeida MM, Costa MEV. Hydroxyapatite micro- and nanoparticles: Nucleation and growth mechanisms in the presence of citrate species. J Colloid Interface Sci 2008;318(2):210-6.

[27] Tao J, Pan H, Zeng Y, Xu X, Tang R. Roles of amorphous calcium phosphate and biological additives in the assembly of hydroxyapatite nanoparticles. J Phys Chem B 2007;111:13410-8.

[28] ICDD PDF: International Centre for Diffraction Data, Powder Diffraction File, Newtown Square, Pennsylvania, USA.

[29] Weiner S, Bar-Yosef O. States of preservation of bones from prehistoric sites in the Near East: A survey. J Archaeol Sci 1990;17:187-96.

[30] Termine JD, Posner AS. Infra-red determination of percentage of crystallinity in apatitc calcium phosphates. Nature 1966;211(5046):268-70.

[31] Blumenthal NC, Posner AS. Effect of preparation conditions on the properties and transformation of amorphous calcium phosphate. Mat Res Bull 1972;7:1181-90.

[32] Hanna f, Hamid ZA. Electrodeposition of biomedical hydroxyapatite coatings on titanium alloy substrate. Pigment Resin Tech 2003;32(5):319-25.

[33] Richards J, Lin DDW. Dispersion of hydroxyapatite nanoparticles into collagen gels. 2012; unpublished.

[34] Tiselius A. Protein chromatography on calcium phosphate columns. Arch Biochem Biophys 1956;65:132-55.

[35] Elliott JC. Structure and chemistry of the apatites and other calcium orthophosphates. Elsevier, 1994.

[36] Reyes-Gasga J, García-García R, Arellano-Jiménez MJ, Sanchez-Pastenes E, Tiznado-Orozco GE, Gil-Chavarria IM, Gómez-Gasga G. Structural and thermal behavior of human tooth and three synthetic hydroxyapatites from 20 to 600 ºC. J Phys D: Appl Phys. 2008;41(22):225407-17.

[37] Johnsson MS, Nancollas GH. The role of brushite and octacalcium phosphate in apatite formation. Crit Rev Oral Biol Med 1992;3(1-2):61-82.

[38] Bouyer E, Gitzhofer F, Boulos MI. Morphological study of hydroxyapatite nanocrystal suspension. J Mat Sci: Mat in Med 2000;11:523-31.

[39] Koutsoukos PG, Nancollas GH. The morphology of hydroxyapatite crystals grown in aqueous solution at 37 ºC. J Crys Growth 1981;55(2):369-75.

[40] Ebrahimpour A, Johnsson M, Richardson F, Nancollas GH. The characterization of hydroxyapatite preparations. J Colloid Inter Sci 1993;159:158-63.

[41] Nancollas GH. The involvement of calcium phosphates in biological mineralization and demineralization processes. Pure Appl Chem 1992;64(11):1673-8

[42] Nancollas GH, Mohan MS. The growth of hydroxyapatite crystals. Archs Oral Biol 1970;15:731-45.

[43] Liu C, Huang Y, Shen W, Cui J. Kinetics of hydroxyapatite precipitation at pH 10 to 11. Biomaterials 2001;22:301-6.

[44] Santos MH, de Oliveira M, de Freitas Souza LP, Mansur HS, Vasconcelos WL. Synthesis control and characterization of hydroxyapatite prepared by wet precipitation process. Mat Res 2004;7(4):625-630.

[45] Cunniffe GM, O'Brien FJ, Partap S, Levingstone TJ, Stanton KT. The synthesis and characterization of nanophase hydroxyapatite using a novel dispersant-aided precipitation method. J Biomed Mat Res Part A 2010;95(4):1142-9.

[46] Boskey AL, Posner AS. Formation of hydroxyapatite at low supersaturation. J Phys Chem 1976;80(1):40-5.

[47] Blumenthal NC, Betts F, Posner AS. Effect of carbonate and biological macromolecules on formation and properties of hydroxyapatite. Calcif Tiss Res 1975;18:81-90.

[48] Boskey AL, Posner AS. Conversion of amorphous calcium phosphate to microcrystalline hydroxyapatite. A pH-dependent, solution-mediated, solid-solid conversion. J Phys Chem 1973;77(19):2313-7.

[49] Yoshimura M, Suda H, Okamoto K, Ioku K. Hydrothermal synthesis of biocompatible whiskers. J Mat Sci 1994;29(13):3399-402.

CHAPTER 3
EFFECTS OF HYDROXYAPATITE CRYSTALLINITY ON HUMAN OSTEOBLAST MATRIX PRODUCTION ON SURFACES

Contributors: Anna Taubenberger, Siddharth Pathi, Dietmar Hutmacher, Claudia Fischbach-Teschl, Lara Estroff

3.1 Abstract

Commercially available and synthetic hydroxyapatite (HA) nanoparticles were dry-annealed at 0, 1, and 3 days at 200 ºC. This technique afforded HA nanoparticles of similar morphology and different crystallinities. These particles were combined with poly(lactide-co-glycolide) (PLG) in tetrahydrofuran (THF) to form HA-PLG solutions. The solutions of HA-PLG were spin-coated onto glass substrates to form thin polymer films with exposed HA particles on the surface. Control surfaces without HA were also fabricated with PLG solutions. The resulting substrates had variable surface roughness and compositions dictated via the type of HA nanoparticle present. Primary human osteoblasts were obtained and seeded onto the substrates. Attachment rate, spreading, metabolic activity, and fibronectin (FN) production were examined at various time points during the culture period. Osteoblasts were shown to be sensitive to the surface properties of the substrate with increased FN production on surfaces containing HA with longer dry annealing treatment regardless of crystallinity. Further examination of the HA surfaces must be conducted to obtain conclusive results.

3.2 Introduction

Many biomaterials used for hard tissue repair today have difficulties in being fully incorporated into native tissues [1, 2]. While the surfaces of the biomaterials are textured, chemically functionalized, and/or loaded with proteins that can direct cellular response and mineralization, the materials are often homogeneous in composition, as compared to the very heterogeneous native tissues. Complete incorporation of these homogenous materials into the tissue is often a challenge [3]. Designing surfaces that are better able to promote the formation of bone-matrix material may lead to better incorporation of materials into hard tissues as well as provide platforms to better understand the mineralization and healing processes of bone.

Bone-matrix formation as discussed in Chapter 1 is dictated by the activity of osteoblasts (OBs), the cells responsible for the production of new bone [4]. The interaction of OBs with the surrounding extracellular matrix (ECM) regulates cellular processes such as cell differentiation and gene expression, leading to changes in adhesion, ECM remodeling, and mineralization activity [5-7]. Factors such as roughness, charge, surface chemistry, and topography can affect cellular behavior and interaction with the material and will affect cell attachment, adhesion, and spreading on surfaces [8-10].

Many studies have been conducted to examine the effects of coatings and patterning of non-biological surfaces to enhance biocompatibility, adhesion, and cellular activity [11, 12]. More recent works examine the effect of hydroxyapatite ($Ca_{10}(PO_4)_6(OH)_2$, HA), which has a similar composition to bone mineral, on cellular functions in the context of grain size, charge, roughness, and density on surfaces [13, 14]. The presence of HA has been demonstrated to promote adhesion of proteins relevant to cell attachment [15-18]. However, much of this work does not take into account the material properties of HA, such as crystallinity, size, and

composition of the mineral. HA crystals in bone are typically thin platelets on the nanometer length scale [19]. These crystals change in size, shape, and crystallinity with age, composition, location, and disease progression [20-24]. To date, little work has been done to examine the effects of highly monodispersed HA particles of different crystallinity, sizes, and composition on OBs adhesion and activity.

In previous work, Reichert and Hutmacher demonstrated a method to form 2-D mineralized OB matrices mimicking the bone microenvironment from primary human osteoblast (hOBs) cells [25]. These matrices were formed on a variety of surfaces such as polystyrene tissue culture plastic, collagen I coated tissue culture plastic, and thermonox coverslips (Nunc®). The hOBs proliferated on the surfaces to form sheets of hOBs and matrix. This work demonstrated the sensitivity of OBs to their culture surface as well as a means to produce surfaces similar to the bone microenvironment. Design of OB culture surfaces containing different types of HA particles can lead to well-characterized platforms to determine the effects of different properties of HA, such as crystallinity, chemistry, size, and roughness, on cellular activity and, ultimately, bone formation. This study aims to develop model HA surfaces and introduce OBs onto the surfaces to evaluate OB ECM production and mineralization as a function of HA mineral properties.

3.3 Materials & Methods

3.3.1 Hydroxyapatite Nanoparticles

3.3.1.1 Synthesis

Hydroxyapatite nanoparticles were synthesized through an aqueous precipitation reaction via drop-wise addition of 300 mL of 10 mM Na_2HPO_4 into 500 mL of 10 mM $CaCl_2$ under rapid

stirring at 4 °C. Precipitate was collected after 72 hrs, washed twice with 15 mM NH_4OH, then once with acetone, and allowed to air dry for 2 days. The precipitate was then annealed at atmosphere in air (GS Blue M Electric model no. OV12A) at 200 °C for 0, 1, and 3 days. These HA nanoparticles will be designated as Type A particles in the rest of the chapter. Commercial HA nanoparticles (designated as Type B) (Sigma Aldrich Hydroxyapatite nanopowder, manufacturer measured < 200 nm) were dry annealed at 200 °C for 0, 1, and 3 days for comparison, indicated as D0, D1, and D3 respectively.

3.3.1.2 Powder X-ray Diffraction

Powder x-ray diffraction (pXRD) was used to characterize the particles (Scintag Inc. PAD-X theta-theta X-ray Diffractometer, CuKα 1.54 Å, accelerating voltage 45 kV, current 40 mA, continuous scan, 2.0 deg/min). Bulk particle size along the c-axis was determined by Scherrer's analysis of the {002} peak [26]:

$$\tau = \frac{K \bullet \lambda}{\beta \bullet \cos(\theta)} \tag{3.1}$$

Where τ is the particle size, K is the shape factor (0.9), λ is the CuKα wavelength of 1.54 Å, β is the full width at half max of the peak of interest, and θ is the Bragg angle of the peak for {002}. Degree of crystallinity was determined from XRD following the formula [27]:

$$X_C = \left(1 - \frac{V_{112/300}}{I_{300}}\right) * 100 \tag{3.2}$$

Where X_C is the degree of crystallinity, $V_{112/300}$ is the intensity of the valley between the peaks for HA indices Miller indices {112} and {300}, and I_{300} is the intensity of the peak for HA Miller index {300}.

3.3.1.3 Fourier Transform Infra-red Spectroscopy

Samples were combined with KBr (Sigma) and ground to a fine powder and pressed into pellets for transmission FTIR (Mattson Instruments 2020 Galaxy Series FT-IR) to obtain FTIR spectra (res 4.0 cm^{-1}, 64 scans). Particle crystallinity was determined qualitatively from sample splitting factor calculated following the method of Weiner and Bar-Yosef, [28] modified from the methods developed by Blumenthal, Termine, and Posner [29, 30] as described in Chapter 2.

$$SF = \frac{A_1+A_2}{A_3} \quad (3.3)$$

Where SF is the splitting factor determined by the sum of the intensities at peaks 602 cm^{-1} (A_1) and 563 cm^{-1} (A_2) divided by the intensity of the minima between the two peaks (A_3).

3.3.1.4 Transmission Electron Microscopy

The morphology of the particles was examined via TEM. Particles were combined with ethanol and dripped onto carbon-coated copper grids (Electron Microscopy Sciences) and allowed to dry. Samples were examined with brightfield TEM (FEI Tecnai T-12 Spirit, 120 kV).

3.3.2 Surfaces

3.3.2.1 Fabrication

HA particles were mixed into acetone, chloroform, and tetrahydrofuran (THF) and particle distribution on substrates from spin coating was examined visually by light microscope

(TE2000-U, Nikon). Glass substrates were prepared by glass microscope slides cut into 25 X 23 mm^2 by diamond scribe. Glass substrates were cleaned by sonicating substrates in isopropyl alcohol for 1 min, followed by 1 min sonication in ethanol, followed by 1 min sonication in acetone and allowed to air-dry in a dust-free environment. Control surfaces without HA were made by dissolving 2 wt% poly(lactide-co-glycolide) (PLG, Lakeshore Biomaterials) in THF and 300 μL of this solution was spin-coated (60 s, 2000 rpm) onto cleansed 25 x 23 mm^2 glass substrates to obtain a film of PLG with a Model PG6700 Series Spincoater (Specialty Coating Systems, Inc). Surfaces containing HA were made by adding 2 wt% HA particles to the PLG-THF solution and sonicating for 30 s. 300 μL of the mixture was spin-coated onto a 25 X 23 mm^2 glass slide. All surfaces were placed in an oven (model no. OV12A, GS Blue M Electric) at 60 °C for 2 hrs until the scent of the THF solvent was not detectable.

3.3.2.2 Characterization

Surfaces were characterized by light microscope. HA accessibility on the surfaces was determined qualitatively via Alizarin Red staining of the surfaces etched for 0, 1, 5, and 10 min in 0.25 M NaOH. For Alizarin Red staining, surfaces were rinsed with phosphate buffered saline (PBS) then fixed with ice cold methanol for 10 min. A 1% alizarin red S (Sigma Aldrich) in DI-H_2O solution was prepared and pH adjusted to4.1 with 10% acetic acid. Surfaces were incubated in the solution for 5 min at room temperature before gently rinsing with DI-H_2O until the water remained clear. Images were taken with a digital camera (Sony DXW).

3.3.2.3 Integrity

Cell-seeded and cell-free surfaces were examined through 28 day culture period under culture conditions. Surfaces were placed in 6-well plates, one surface per well, submerged in 3 mL of complete DMEM (cDMEM, DMEM [Invitrogen] supplemented with 10% fetal bovine serum [Tissue Culture Biologicals] and 1% penicillin/streptomycin [Invitrogen]) at 37 ºC, 5% CO_2 in a cell culture incubator. Media was changed twice a week.

3.3.3 Osteoblasts

3.3.3.1 Harvest

Primary human osteoblasts were obtained from the tibial plateau of female patients undergoing knee replacement surgery (Queensland University of Technology institutional ethics committee approved) following the protocol established by Reichert [25]. Bone chips were removed from the trabecular bone with a spatula then washed with phosphate buffered saline (PBS) until the solution remained clear. Cleaned bone chips were placed into culture flasks with culture media (α-MEM, minimum essential medium, 12561, Invitrogen, supplemented with 10% FBS (fetal bovine serum, Invitrogen), 1% AB/AM (antibiotic/antimycotic, Invitrogen) and incubated. By two weeks, hOBs grew out of the bone chips onto the flasks.

3.3.3.2 Culture

Surfaces were placed in 70% ethanol for 1 hr, air-dried, and then sterilized by irradiation with UV for 15 min. No visible effect was observed through light microscopy, further examination was not conducted. Surfaces were then immersed in culture media for 1 hr. The media was removed before introducing the hOBs. Cells were harvested from the tissue-culture

flasks and seeded via three methods: 1) Filling the well containing the surface with 3 mL of 16,000 cells/mL, 2) placing a 1 mL droplet of media containing 3,000/cm^2 cells onto the surface before adding 2 mL of media 3 hrs or 3) 12 hrs later.

3.3.3.3 Attachment and Spreading on Platforms

Cells were incubated in staining solution (2 μL of 4 mM calcein in 8 mL media) to better visualize the cells before seeding. Optical light microscope (TE2000-U, Nikon) images were taken of the surfaces at 4 and 15 hrs to track attachment and spreading on the coated slides after cell seeding and quantified via ImageJ. Attachment was confirmed by determining number of cells that were spherical (unattached) and the number of cells that were non-spherical (attached). Spreading was quantified by area fraction of coverage by cells within a defined field of view.

3.3.3.4 Osteoblast Metabolic Response Characterization via AlamarBlue

The alamarBlue® assay was done to compare metabolic activity of cells. AlamarBlue® reagent was prepared with 2 mL alamar (Invitrogen) in 20 mL media. Media was aspirated from surfaces, replaced with 200 μL droplets of alamarBlue® reagent and allowed to incubate for 1 hr. AlamarBlue solution was removed from the surfaces and placed into a 96-well plate and fluorescent signals (excitation 544 nm, emission 590 nm) detected with a fluorescent plate reader (Polar Star Optima plate reader (BMG Labtech) to determine metabolic activity. Cell-free surfaces were used as controls. Time points were taken at Day 1, 3, 5, 7, 14, and 20.

Surfaces were immunofluorescently stained to study spreading morphology and fibronectin (FN) production. To prepare surfaces for staining, surfaces were washed twice with PBS (phosphate buffered saline) containing 0.5 mM $MgCl_2$ and 0.9 M $CaCl_2 \cdot 2H_2O$ and fixed

with 4% formaldehyde solution in PBS for 30 min at room temperature. Samples were rinsed once with 3 mL PBS and cells permeabilized for 5 min with 0.2 % Triton X-100 (Sigma) in PBS. Surfaces were then rinsed twice with 3 mL PBS before incubating surfaces in 0.5% BSA (bovine serum albumin, blocking buffer) and incubated for 10 min. Primary antibody solution FN DSEC.DHN antibody was prepared at 1:300 in 0.5% BSA in PBS. 200 uL of the primary antibody solution was placed on surfaces for 45 min then washed three times with 3 mL PBS. 200 μL of the secondary antibody solution containing 1:300 Alexa Fluor 633 goat-antihuman IgG, 1:250 rhodamine-phalloidin (Invitrogen) for staining actin filaments, and 1:1000 DAPI nuclear stain in 0.5% BSA in PBS onto the surfaces for 45 min. Surfaces were washed twice with 3 mL PBS and dipped into DI-H_2O for removing salts. Excess liquid was blotted with a Kimwipe^{TM} (Kimberly-Clark®) before mounting coverslips onto the surface with mounting medium (ProLong Gold, Invitrogen). Surfaces were dried overnight away from light. Surfaces after 5 and 20 days of culture were examined under confocal microscopy (Leica TCS SP5). Each condition was examined in triplicate.

3.4 Results

To examine how HA nanoscale properties could affect cellular activity, HA nanoparticles were synthesized from an aqueous chemical precipitation (A) and obtained commercially from Sigma Aldrich (B). As described in chapter 2, these particles were dry-annealed at 200 °C for 0, 1, and 3 days (AD0, AD1, AD3, BD0, BD1, BD3). These particles were then combined with a solution of PLG dissolved in THF. The mixtures were spin-coated onto glass substrates to present different HA particles to the cells. After characterization and analysis of the particles

and the surfaces, primary hOBs were then seeded onto these surfaces. The adhesion, spreading, and FN production of the hOBs were examined for each of these platforms.

3.4.1 Materials Analysis

3.4.1.1 Particle Analysis

Hydroxyapatite particles were synthesized through aqueous precipitation of $CaCl_2$ and Na_2HPO_4 then dry annealed for 0, 1, and 3 days. Synthesized particles were designated as AD0, AD1, and AD3 respectively. Commercial particles were also dry annealed for 0, 1, and 3 days and designated as BD0, BD1, and BD3 respectively. The dry annealing of the A and B particles at 200 ºC allowed the particles to maintain their original shape as confirmed through TEM. The A particles remained as small, thin platelets while the B particles retained their spherical morphology (Fig. 3.1).

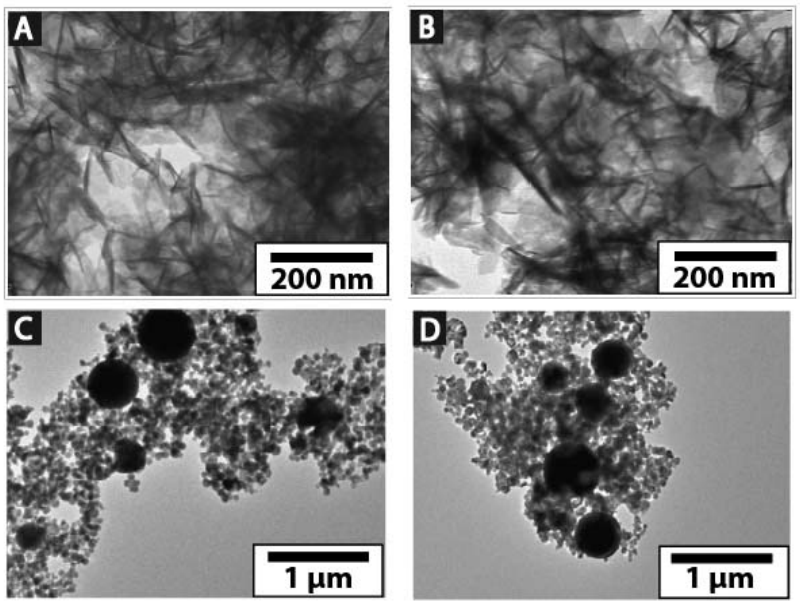

Figure 3.1: Synthetic as-precipitated AD0 HA particles (A) and synthetic AD3 HA particles dry-annealed for 3 days at 200 ºC (B). Commercial BD0 HA particles (C) and commercial BD3 HA particles after annealing at 200 ºC for 3 days (D).

XRD confirmed the phases of the particles to be HA showing the characteristic peaks for HA crystal indices {002}, {211}, {300}, and {202} (Fig. 3.2). XRD spectra for B particles showed the presence of more peaks which were sharper and more defined compared to A particles. With the heat treatment, a slight decrease in particle size was observed for A and B particles as well as a slight decrease in degree of crystallinity for B particles (Table 3.1). Degree of crystallinity could not be determined for A particles due to the absence of a valley between the {112} and {300} peaks using the equation (2).

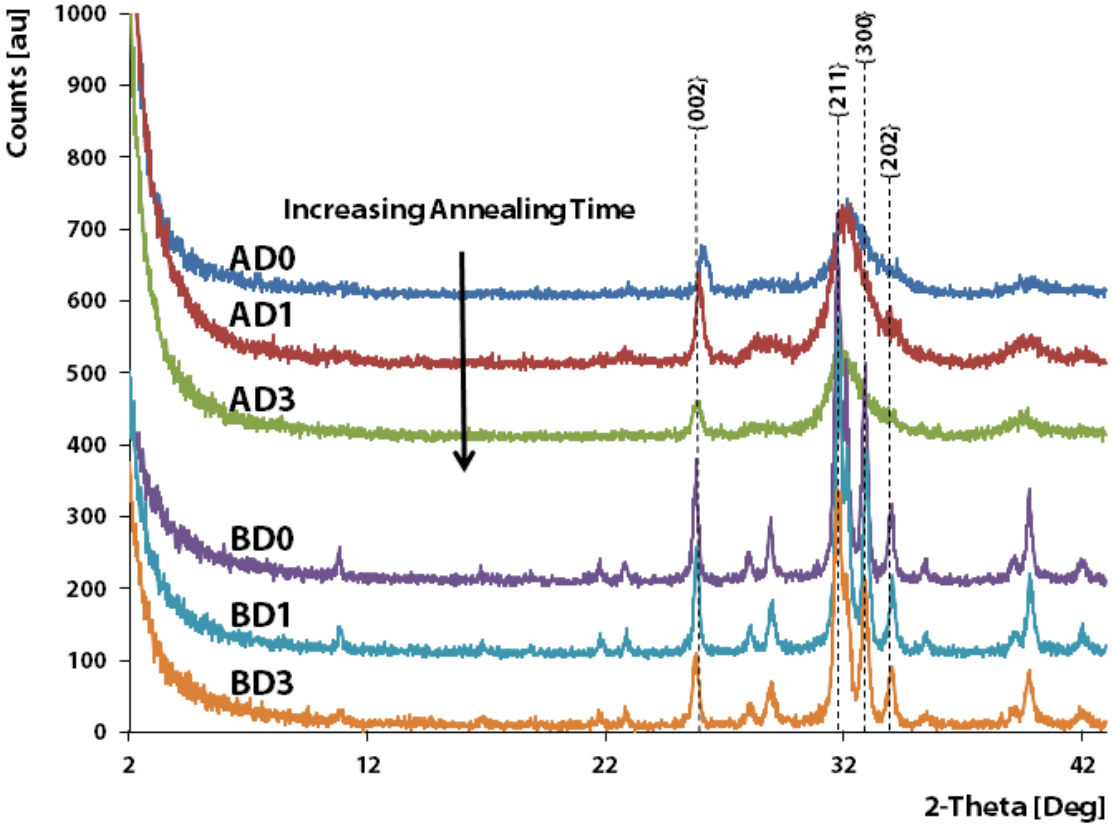

Figure 3.2: pXRD spectra of A annealled at 0 (AD0), 1 (AD1), and 3 (AD3) days and B particles annealled at 0 (BD0), 1(BD1), and 3 (BD3) days at 200 ºC. Hydroxyapatite Miller indicies are indicated by the dotted lines as identified by ICDD PDF no. 09-0432. crystal [31].

Table 3.1: HA particle size and fraction of crystallinity

Particle	Size [nm][a]	Degree of Crystallinity[b]	Splitting Factor[d]
AD0	26	---[c]	3.8
AD1	27	---	4.1
AD3	14	---	4.2
BD0	35	84	3.6
BD1	34	83	3.6
BD3	28	79	3.5

[a]Size along {002} c-axis of HA determined by Scherrer's Analysis, (Eq. 3.1) [26].
[b]Degree of crystallinity calculated from the difference in intensity at {300} and the valley between {112} and {300} divided by the intensity at {300} times 100, (Eq. 3.2) [27].
[c]Degree of crystallinity could not be determined for A particles due to the absence of a valley between {112} and {300}.
[d]Splitting factor calculated from peaks attributed to phosphate ν_4, (Eq. 3.3) [28].

FTIR of the particles also showed the characteristic peaks for phosphate ν_4 antisymmetric bending (570-602 cm^{-1}) and phosphate ν_3 antisymmetric stretching modes (1032-1048 cm^{-1}) for HA (Fig. 3.3) [32, 33]. The phosphate ν_1 peak at 961 cm^{-1} was also present for all particles. Less peak broadening was observed for B particles compared to A particle spectrum. A particles also have the presence of carbonate peaks at 1384 cm^{-1}, absent for B particles. Increased crystallinity with increasing annealing time is evidenced by the decrease in peak broadening and appearance of a peak at 630 cm^{-1} for AD1 and AD3 indicative of structural –OH, which increases in intensity with more crystalline materials (Fig. 3.2) [34]. A small peak at 630 cm^{-1} was also observed for BD3 particles for acid phosphate. Calculation of the splitting factor of the ν_4 phosphate bond bending peaks at 562 cm^{-1} and 602 cm^{-1} corroborated a slight increase in splitting factor with annealing time for A particles [28, 32]. No significant changes in splitting factor were observed for B particles (Table 3.1).

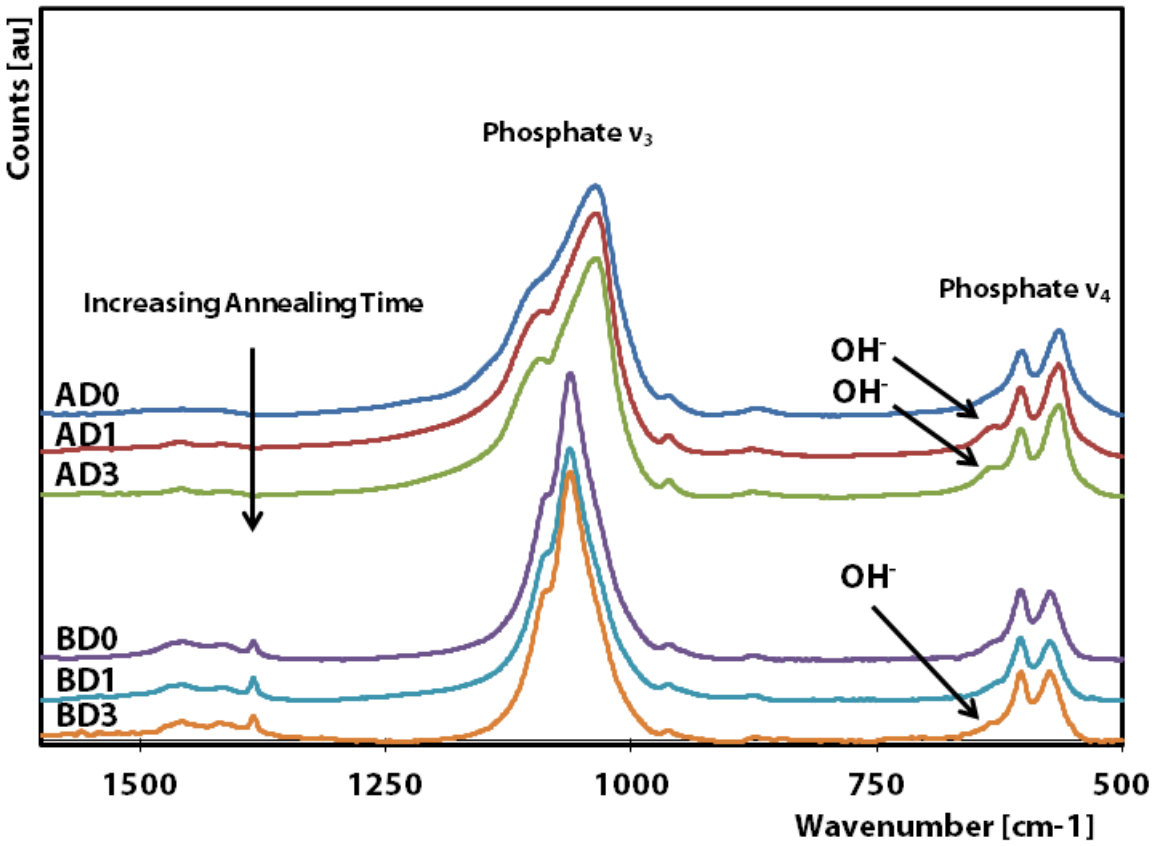

Figure 3.3: FTIR spectra of A and B particles annealed for 0, 1, and 3 days show the characteristic phosphate ν_3 and ν_4 peaks of HA. The increase in crystallinity with annealing time was confirmed for A particles with the appearance of peak at 630 cm^{-1} for structural –OH. BD3 particles also show the presence of a small peak at 630 cm^{-1}.

3.4.1.2 HA-PLG Surface Coating

Spin-coating was used to form substrates coated with PLG-HA (A and B) or PLG only (O) surfaces for cell culture (Fig. 3.4). Surfaces coated in PLG without HA were used for controls (O). Particles were suspended in a variety of organic solvents capable of dissolving including acetone, THF, and chloroform to determine which solvent would be most suitable for dispersing the HA. Particle distribution in the spin-coated films of A-type particles was highly dependent upon the particle dispersity in the PLG-Solvent-HA mixture where B particles had a

similar dispersity regardless of solvent. THF was most effective in forming the PLG and PLG-HA films on the 25 x 23 mm glass substrates through spin coating due to better particle dispersion and slower evaporation time compared to chloroform and acetone. One possible explanation is that the A particles have a different surface charge or retained different amounts of water than B particles. Based on these results, subsequent work used THF for preparing surfaces.

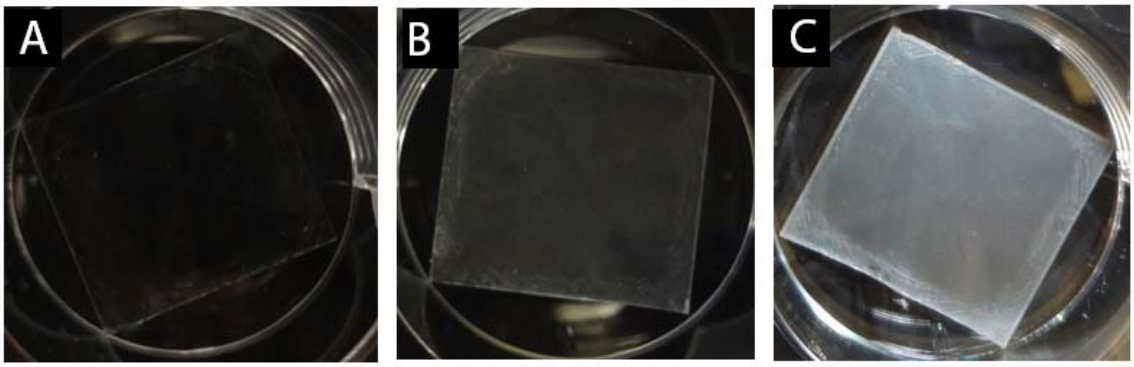

Figure 3.4: Photographs of control PLG–only (A), synthetic HA Type A (B) and commercial HA Type B (C) surfaces fabricated by spin-coating HA-PLG in THF onto glass substrates followed by 1 hr of heat treatment at 60 ºC to remove THF.

3.4.1.3 Surface Analysis

Optical microscope and SEM observations of the surfaces showed how A particles tended to aggregate together instead of spreading evenly throughout the surfaces (Fig. 3.5A-C). Surfaces containing both particle types showed indications of spin-coating artifacts where particles were distributed more densely towards the center of the surfaces compared to the edges. For surfaces containing B particles, streaks of areas with low and high particle density radiating out from the center of the surfaces to the edge were visible (Fig. 3.5D-F). Comparing surfaces containing the same type of particles annealed for different durations, however, showed the

surfaces to be very similar in appearance (Fig. 3.5A-F). The particles were distributed inhomogenously across the surface, however A particles had similar distributions regardless of annealing time as did B particles (Fig. 3.5G-I).

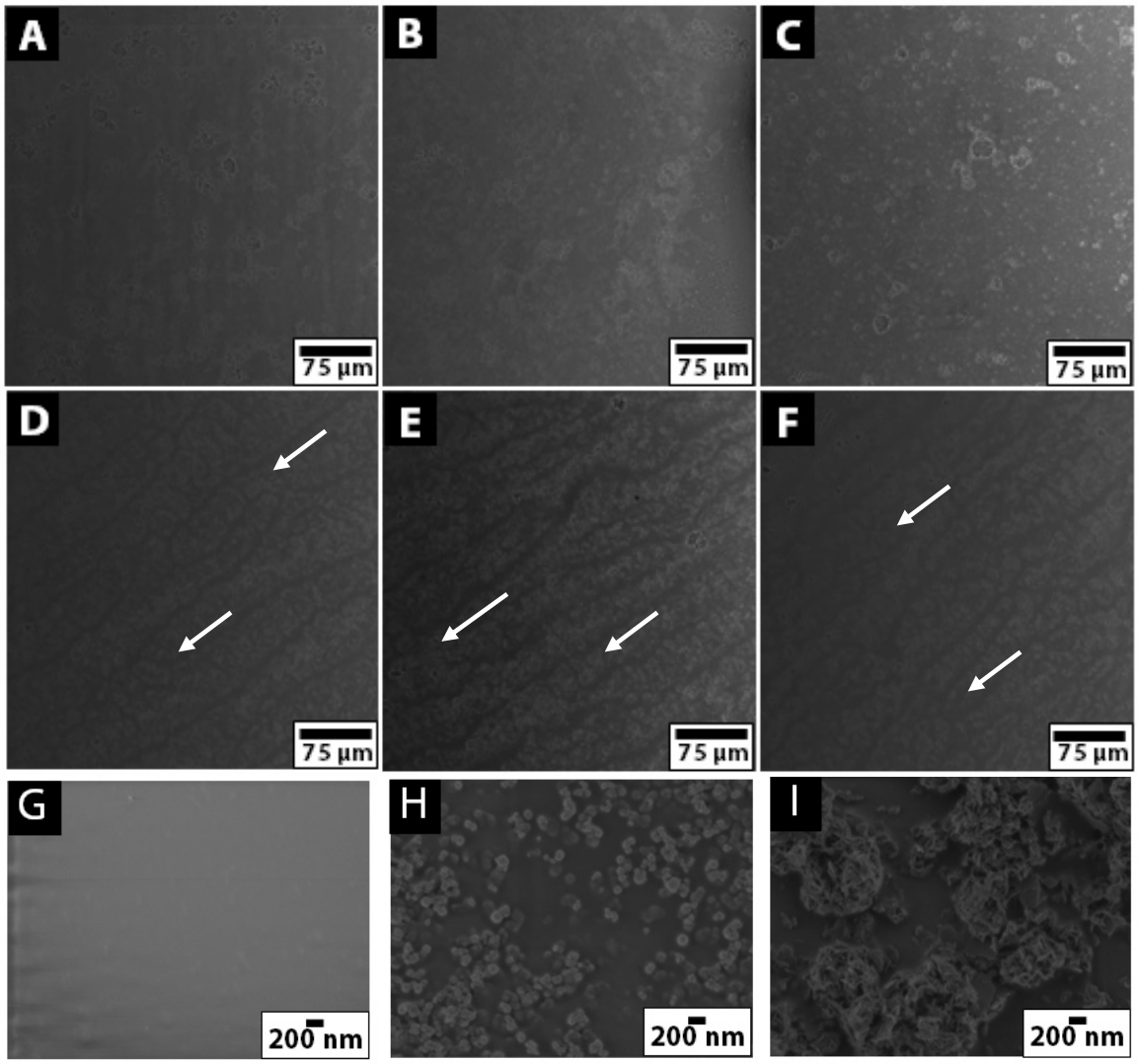

Figure 3.5: Optical microscope images of AD0 (A), AD1 (B), AD3 (C), BD0 (D), BD1 (E), and BD3 (F) surfaces showing distribution of particles after spin-coating. White arrows show HA distribution as streaks as a spin-coating artifacts further from the center of B-containing surfaces. SEM images show higher magnification of particle distribution in control (G), AD0 (H), and BD0 (I) surfaces. *SEM courtesy of Jason Dorvee.*

3.4.1.4 HA Accessibility for Cells

To assess the surface exposure of HA, Alizarin Red staining was performed on as-prepared surfaces as well as NaOH etched surfaces. The etching process was designed to dissolve the polymer and further expose HA on the surface. HA surfaces were etched in 0.25 M NaOH for 0, 1, 5, and 10 min to determine if etching treatments were necessary to improve access of hOBs to HA. Surfaces were stained after the etching process with Alizarin Red. Control surfaces retained no color as expected while all other surfaces turned red after the staining process, showing that HA was exposed at the surface. A-surfaces degraded with longer etching times while B-surfaces retained surface films (Fig. 3.6). Based upon this evaluation, no etching was applied to surfaces before cell culture experiments.

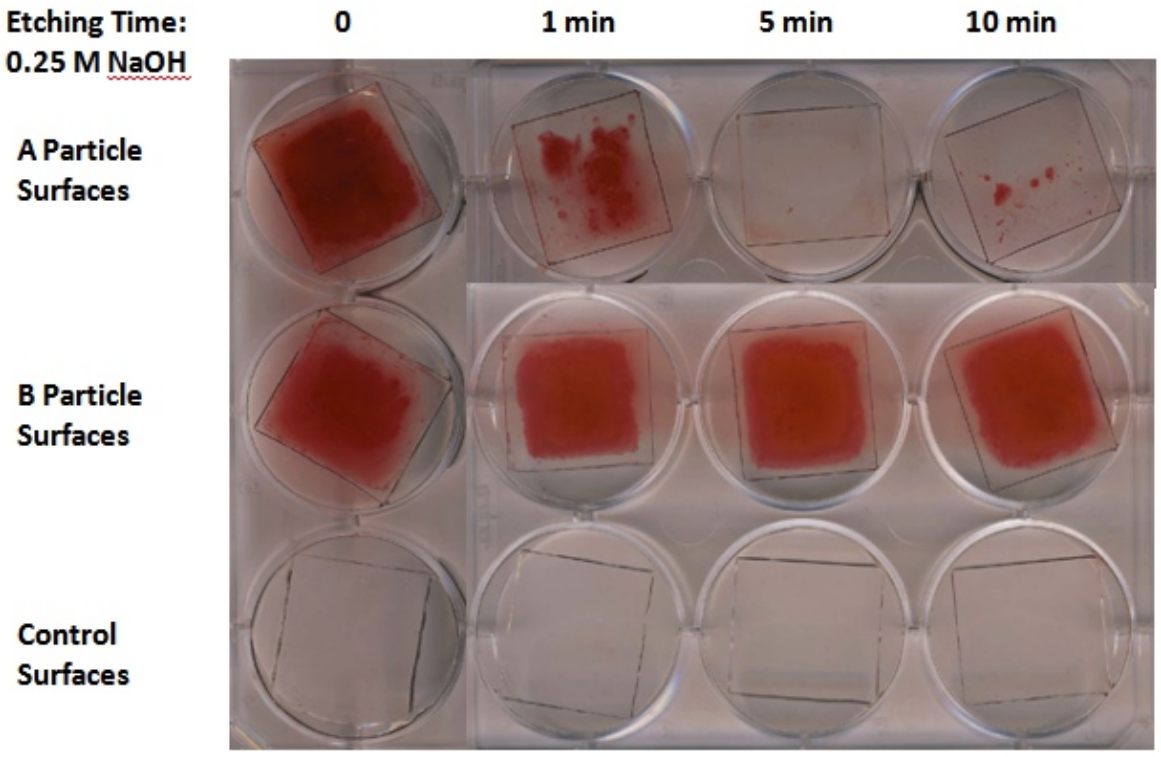

Figure 3.6: Photographs of Type A HA, Type B HA, and control substrates stained with Alizarin Red after 0, 1, 5, and 10 min of etching in 0.25 M NaOH to determine surface exposure of HA.

3.4.2. Assessment of Osteoblast Interaction with Surfaces

3.4.2.1 Culture Methods on Surfaces

Surfaces were placed into 6-well plates prior to culture. Due to the rectangular shape of the surfaces and height from the bottom of the well, quantifying the number of cells seeded onto the surfaces was challenging due to cells attaching to the 6-well plate rather than the surfaces. To optimize cell seeding onto the surfaces, three methods were tested: 1) Cells were seeded via filling the well containing the surface with 3 mL of 16,000 cells/mL, or 2) placing a 1 mL droplet of media containing 3,000/cm^2 cells onto the surface before adding 2 mL of media 3 hrs or 3) 12 hrs later. Method 1 often resulted in higher concentration of cells near the middle of the surface due to the media forming a meniscus in the well. Method 2 did not allow sufficient time for the cells to adhere to the surfaces before adding additional media, which resulted in the cells being washed off the surface. Method 3 was able to provide more uniform seeding of the cells but the droplet was difficult to maintain for all samples through the 12 hr period. Experiments were conducted with cell seeding method 1 or 3. Method 1 was used if the initial number of cells was not relevant for the experiment. Method 3 was used if the initial number was important for the experiments.

3.4.2.2 Surface Integrity In Culture Conditions

Osteoblasts were cultured onto surfaces to evaluate PLG and PLG-HA surface integrity under culture conditions submerged in media, at 37 °C, 5% CO_2, with humidity. Cell-free surfaces were used as controls. Cell-free HA-containing PLG films remained intact throughout the 28 day integrity tests under culture conditions. Control surfaces without HA, PLG-only

films, delaminated from the corners of the glass substrates by day 12. In comparison, all of the cell-seeded surfaces showed evidence of degradation (Fig. 3.7).

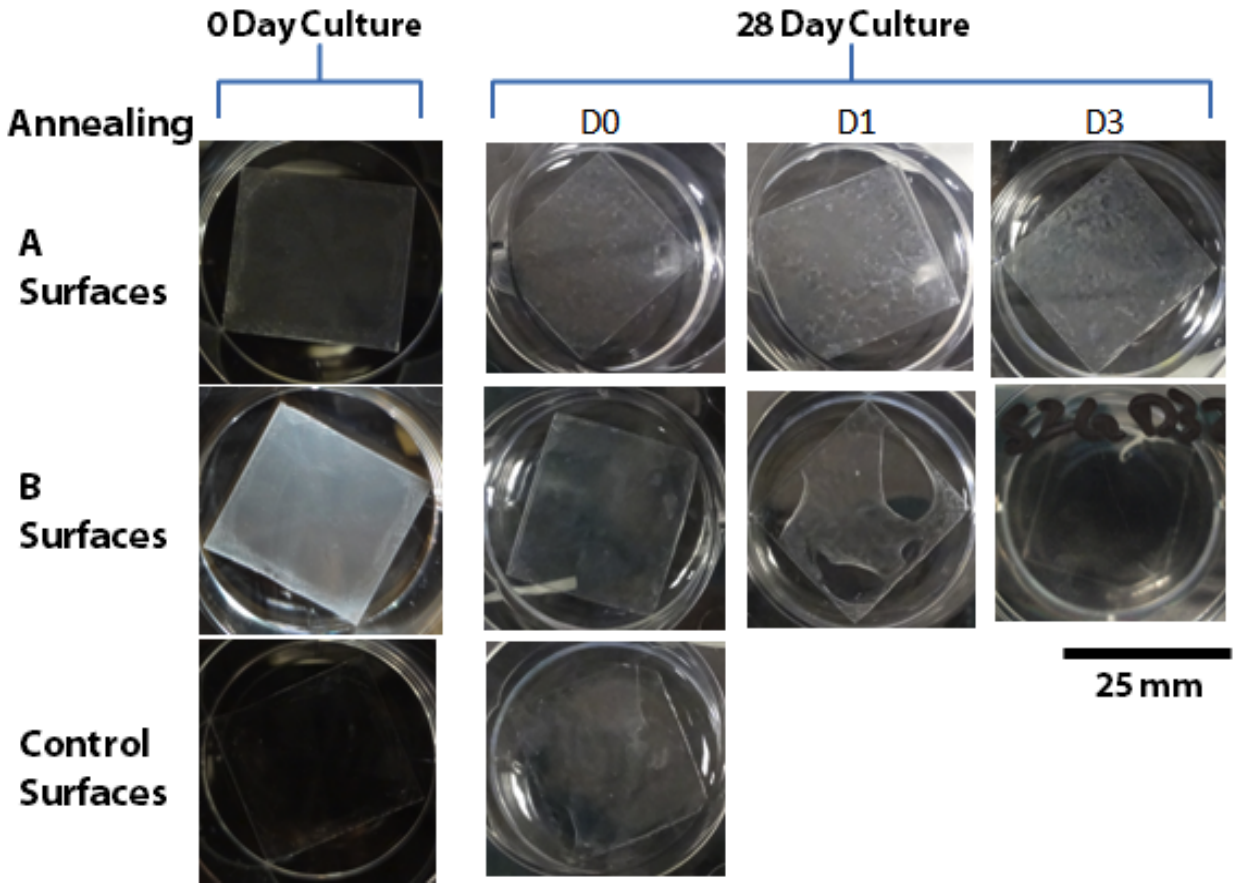

Figure 3.7: Photographs of osteoblast-seeded A-, B-, and control substrates before culture and at 28 days of culture to assess surface integrity under osteoblast culture. Representative surfaces shown from n=3.

Although surfaces containing A particles remained on the glass substrates, small holes appeared in the PLG-HA substrates by day 20. The surfaces containing the B particles remained intact for non-annealed HA. However, large holes appeared on the surfaces containing 1 and 3 day annealed HA particles on day 7 and 2 out of 3 films curled up and completely detached from the

glass substrates by day 12. The PLG-only films detached part way from one corner of the substrates, but remained stable through the rest of the culture period. On closer inspection of the surfaces via optical microscopy, it appeared that holes were forming on the film and were widened once the hOBs had proliferated to cover the entire surface to form a sheet of cells (confluence) on the surfaces. Additionally, the increased amounts of film detachment from surfaces containing the annealed commercial HA indicate that the hOBs appeared to be placing strain onto the films and areas of the film detached to relax the strain. The experiment was repeated with a lower seeding density for cell cultured surfaces. Cells did not proliferate enough to reach confluency within the first 4 weeks and were able to remain intact through 34 days of culture. Further studies cultured cells onto the surfaces were not cultured past 25 days

3.4.2.3 Proliferation and Spreading on Surfaces

OB attachment and spreading on surfaces were assessed through 15 hrs. Cells were cultured onto surfaces then stained with calcein staining solution and examined via optical microscope. OBs attached to control and B-surfaces sooner than surfaces containing A particles. At 15 hrs, most cells have attached to the surfaces. Greater percentage of spreading was observed for control surfaces that did not contain HA and at 15 hrs, A- and B-surfaces see similar OB spreading areas (Fig. 3.8).

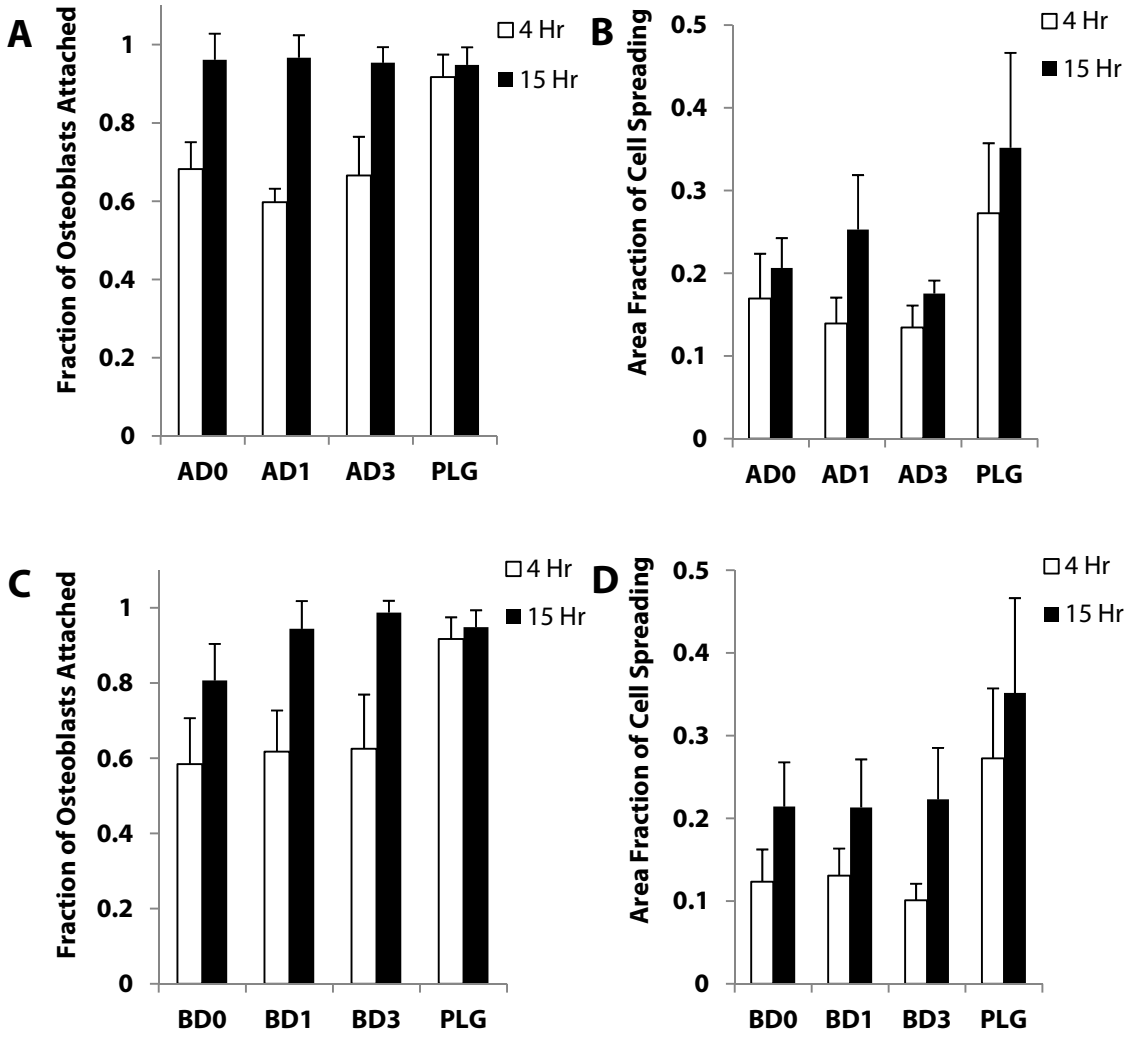

Figure 3.8: Osteoblast attachment after 4 (white) and 15 hrs (black) of seeding on AD0, AD1, AD3 (A) and BD0, BD1, BD3 (C) surfaces. PLG surfaces were used as controls. Osteoblast spreading area was determined after 4 and 15 hrs of culture on the same surfaces (B, D). Area fraction was normalized to the number of cells present in the field of view

3.4.2.4 Metabolic Activity

Metabolic activity was assessed by alamarBlue®. Increased metabolic activity was observed around day 8 for the hOBs grown on B particle surfaces while increased metabolic activity was detected after day 8 on A particle surfaces (Fig. 3.9). The earlier increase in

metabolic activity for cells grown on B particles indicate that hOBs proliferate faster on B particle surfaces compared to A particle surfaces.

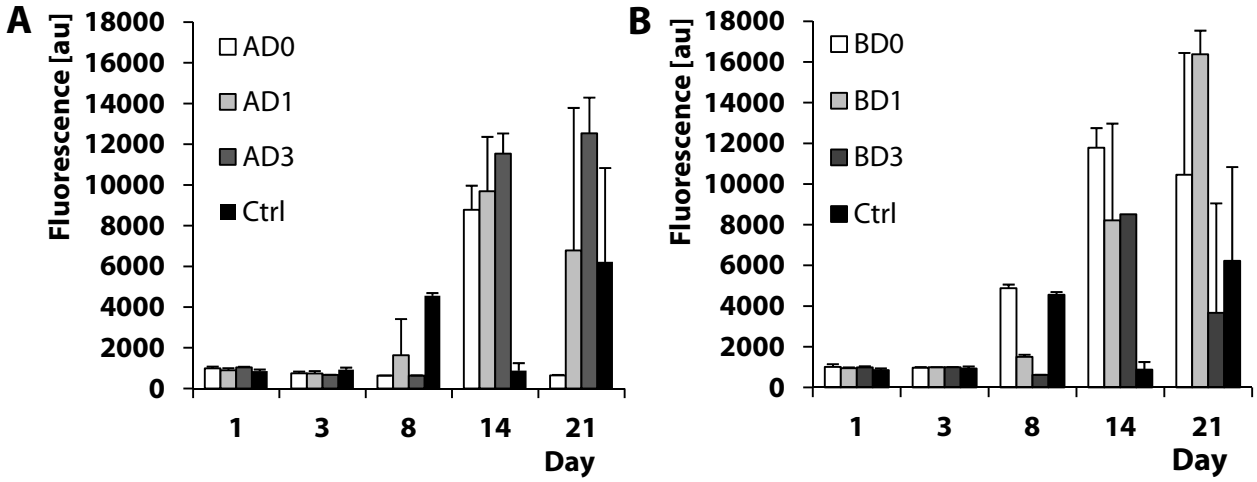

Figure 3.9: Metabolic activity of osteoblasts cultured on AD0, AD1, AD3 (A) and BD0, BD1, BD3 (B) surfaces at 1, 3, 8, 14, and 21 days of culture as determined via relative fluorescence from alamarBlue® assays. PLG surfaces were used as controls (Ctrl).

3.4.2.5 Fibronectin Production

The cell-seeded surfaces were immunofluorescently stained for actin (red), the cytoskeleton of the cells to examine spreading on the surfaces, the nucleus (blue), and FN (green), a protein associated with matrix production and adhesion (Fig. 3.10). After staining, the surfaces were imaged with confocal microscopy to examine the cell spreading and FN production. Initial images of the surfaces show that hOBs grown on PLG surfaces have larger nuclei and spreading area on day 5 compared to HA-containing surfaces. The larger cell size is maintained as the cells reach confluency as seen in cells cultured through day 28. The increased green fluorescence indicates increased production of FN production on surfaces containing 3 day annealed HA particles.

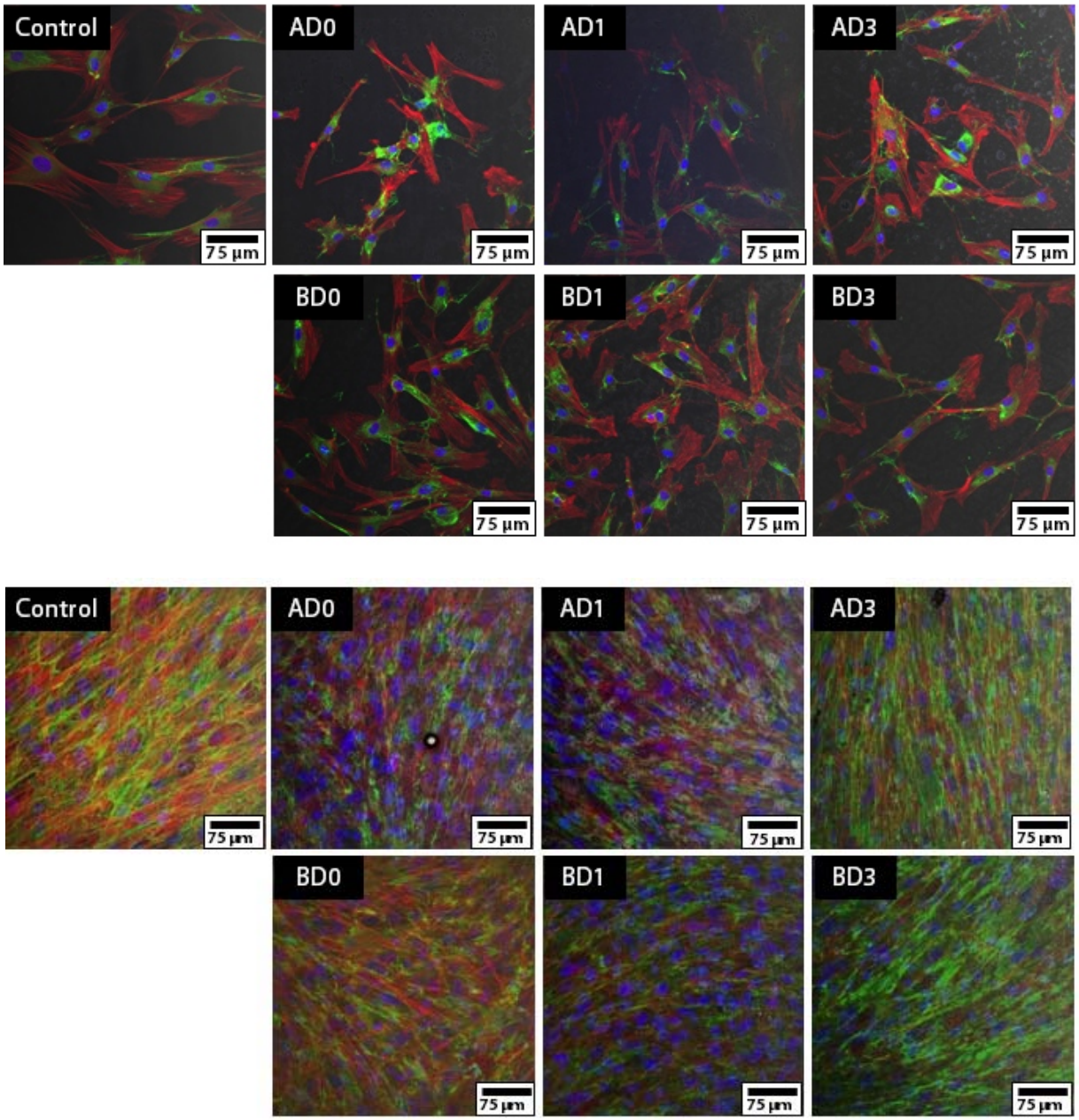

Figure 3.10: Immunofluorescent staining of osteoblast actin (red), nucleus (blue), and fibronectin (green) after 5 (Top) and 28 (Bottom) days of culture on AD0, AD1, AD3, BD0, BD1, BD3, and control PLG surfaces. *Confocal microscopy images courtesy of Anna Taubenberger.*

3.5 Discussion

Osteoblast sensitivity to the bone microenvironment is necessary for OB function in remodeling and healing bone [17]. It has been observed that with time, age, location, and disease pathology, HA crystals in bone change in size, shape, and crystallinity [20-25]. To understand OBresponse to changes in the bone microenvironment with regards to the changes in bone crystals, HA nanoparticles were synthesized from an aqueous precipitation reaction and obtained commercially. Particles were dry-annealed for 0, 1, and 3 days at 200 °C and incorporated into polymer films on glass slides. Surfaces were prepared by spin-coating dry-annealed synthetic (A) and commercial (B) HA nanoparticles in PLG onto glass substrates. These surfaces were then seeded with primary hOB cells to determine how hOBs respond to HA differences from heat treatment. Surfaces spin-coated with PLG without HA were used as controls. The resulting surfaces were heterogeneous in nature with regions of high and low mineral density dispersed through the polymer. The distribution of particles on the surfaces was similar for the particle type (A or B) regardless of dry-annealing time and allows for comparison of the effect of annealing HA particles on hOB response on surfaces with similar features.

Osteoblasts have increased attachment and proliferation on HA nanoparticles with increased crystallinity, however, many of these studies often examine crystallinity in the context of comparing other phases such as amorphous calcium phosphate [35], change in processing methods [37], or HA size [38]. The synthesis of the HA particles by aqueous precipitation (A particles) followed by dry annealing was aimed to introduce changes in crystallinity with minimal changes to HA shape and size. TEM images confirmed the maintenance of shape, however XRD indicates a small decrease in size for particles annealed for 3 days. Increase in crystallinity for A particles was observed from increase in splitting factor calculated from

phosphate v_4 peaks [32] and the appearance of –OH libration peak at 630 cm^{-1} with longer annealing times [34, 29]. For the commercially obtained B particles, an increase in crystallinity is not observed with longer annealing time, rather a slight decrease is observed from degree of crystallinity determined from XRD and splitting factor from FTIR. The synthesis method for commercial B particles is unknown, however the higher number of narrow peaks in the XRD indicate B to be the more crystalline material compared to A. Synthetic A particles may retain water and heat treatment allows for removal of excess water and increased crystallinity while for B particles this treatment may introduce more disorder by facilitating carbonate incorporation into the lattice [40]. Examining the FTIR spectra more closely, carbonate is present in both A and B particles, indicated by peaks at carbonate v_4 around 1450 cm^{-1}, and carbonate v_2 around 870 cm^{-1} but appears to be greater for B particles [39, 41-43]. The increase in intensity at 630 cm^{-1} with annealing time for A particles is indicative of increased lattice order, which allows for detection of the –OH libration mode at 630 cm^{-1} (acid phosphate). With increased disorder and increased carbonate substitution in the lattice, the –OH becomes undetectable, which may be the case for B particles. Additionally, the presence of the peak at 1384 cm^{-1} indicative of carbonate stretching [44] is absent in A particles. The lower splitting factor values of B particles compared to A particles may be due to the disruption of highly crystalline lattice with heat treatment in air [45], the wide range of sizes from 20-600 nm [46], and/or the increased carbonate content of B particles [47, 48]. The splitting factors of A and B particles corresponds poorly with the pXRD spectrum in terms of "crystal quality" where peaks of B are clearly more distinct than A. This discrepancy may be due to the smaller particle size of A particles.

Primary human osteoblasts were chosen as the cell-type to examine on these surfaces, as they are prominent bone cells, sensitive to the bone microenvironment and taken directly from

human bone. Osteoblast attachment to the surfaces was higher for control PLG surfaces and surfaces containing B particles and AD3 particles after 4 hrs, however, after 15 hrs, the number of cells attached to the surface was roughly the same. The spreading of the hOBs after 4 hrs appear to be greater for control surfaces, BD0, and BD1 surfaces compared to BD3, and A particle surfaces. After 15 hrs, the spreading area is similar for all HA-containing surfaces and highest for control surfaces. The increased spreading of hOBs on HA-free surfaces is maintained through culture and the hOBs are observed to have larger nuclei from immunofluorescent staining of cultures on day 5 and 28. The difference in hOB spreading area and nuclei size between control and HA-containing surfaces indicate the presence of HA may affect the spreading of hOBs. Visual inspection of surfaces through the duration of culture showed that surfaces containing annealed B particles would start to curl away from the glass substrate onto itself on day 7 as hOBs proliferated to cover the surfaces while other surfaces remained stable. Inspecting the results of alamarBlue assay for metabolic activity showed an earlier increase in metabolic activity for cells seeded on B particles compared to A, however as BD0 surfaces had the higher increase in activity while the surface remained intact, it is unclear whether the film removal from the surface is due to increased interaction of hOBs with the heat-treated B-particles or if the heat-treatment changes the manner that PLG interacts with the HA on deposition to the glass substrate.

Fibronectin is an extracellular matrix (ECM) glycoprotein produced early on after the proliferative phase of osteoblasts [49]. This protein has been shown to regulate adhesion and migration [50] and is necessary for the function and survival of mature osteoblasts [51] and bone development [52]. Immunofluorescent staining of hOB-seeded surfaces after 28 days of culture indicate FN production on all surfaces with increased amount of FN on the surfaces containing

AD3 and BD3 particles with a more fibrillar appearance. The increased FN production on the surfaces cannot be completely attributed to increased crystallinity of HA as AD1 and AD3 have similar levels of crystallinity according to the calculated splitting factor. OB cultures have shown to deposit FN in more organized network pattern in the presence of HA [50]. Heat treatment of particles may enhance the molecular interaction of FN with HA on the surface and provide signals to encourage FN deposition by the OBs.

Dry annealing of HA particles appear to increase FN deposition on the surface and enhance OBs interaction with the surface. However, these effects cannot be completely attributed to an increase in crystallinity, if at all, as demonstrated from FTIR studies. At 3 days of annealing, surface roughening may also be occurring and on removal from the oven, incorporate water. Additionally, similarity in cellular response to A and B particles after 3 days of annealing may be attributed to A-particle tendency to aggregate and form crystal clusters similar in size to B particles to minimize surface roughness differences on the glass substrate. The carbonate content of the HA particles has yet to be thoroughly investigated and may play a role in molecular-level interaction with OBs. Further investigation is necessary to elucidate the interaction of OBs with annealed HA particles and may be better achieved with the development of more uniform surfaces.

3.6 Conclusions

Osteoblasts are sensitive to their surrounding environment as observed in the experiments described above. Changes in the nanomaterial properties of HA can affect how bone cells interact with the bone microenvironment. In this study, cells attached and spread more readily to surfaces without HA, however, with time, metabolic activity was enhanced for cells seeded on

HA-containing surfaces. With longer culture periods, increased presence of FN was observed for cultures containing HA with longer heat treatments indicating that heat treatment, crystallinity, along with size and morphology can affect OB response to their microenvironment. Additional studies are needed to better understand the effects of HA crystallinity on cellular activity and exploring larger distributions in size and crystallinity may be necessary depending on the sensitivity of cells to smaller or larger differences for better comparison. These investigations should be coupled with techniques to prepare more uniform surfaces to minimize effects from heterogeneity between conditions.

References

[1] Mikos, AG, Herring, SW, Ochareon, P, Elisseeff, J, Lu, HH, Kandel, R, Schoen, FJ, Toner, M, Mooney, D, Atala, A, Van Dyke, ME, Kaplan, D, Vunjak-Novakovic, G. Engineering complex tissues. Tissue Eng 2006;12(12):3307-39.

[2] Moffat, KL, Wang, INE, Rodeo, SA, Lu, HH. Orthopedic interface tissue engineering for the biological fixation of soft tissue grafts. Clin Sports Med 2009;28(1):157-76.

[3] Blueno, EM, Glowacki, J. Cell-free and Cell-based approaches for bone regeneration. Nat Rev Rheumatol 2009;5(12):685-97.

[4] Olah, A.J. Quantitative relations between osteoblasts and osteoid in primary hyperparathyroidism, intestinal malabsorption and renal osteodystrophy. Virchows Arch A Pathol Pathol Anat 1973;358(4):301-8.

[5] Vogel V, Baneyx G. The Tissue engineering puzzle: a molecular perspective. Annu Rev Biomed Eng 2003;5:441-63.

[6] Grinnell F. Fibroblast biology in three-dimensional collagen matrices. Trends Cell Biol 2003;13:264-9.

[7] Cukierman E, Pankove R, Yamada KM. Cell interactions with three-dimensional matrices. Curr Opin Cell Biol 2002;14:633-9.

[8] Anselme K. Osteoblast adhesion on biomaterials. Biomaterials 2000;21:667-81.

[9] Hott M, Noel B, Bernache-Assolant D, Rey C, Marie PJ. Proliferation and differentiation of human trabecular osteoblastic cells on hydroxyapatite. J Biomed Mater Res 1997;37:508-16.

[10] Shah AK, Lazatin J, Sinha RK, Lennox T, Hickok NJ, Tuan RS. Mechanism of BMP-2 stimulated adhesion of osteoblastic cells to titanium alloy. Biol Cell 1999;91(2):131-42.

[11] Lloyd AW. Interfacial bioengineering to enhance surface biocompatibility. Med Device Technol 2002;13(1):18-21.

[12] Lee KB, Park SJ, Mirkin CA, Smith JC, Mrksich M. Protein nanoarrays generated by dip-pen nanolithography. Science 2002;295(5560):1702-5.

[13] Dorozhkin SV. Nanosized and nanocrystalline calcium orthophosphates. Acta Biomater 2010;6(3):715-34.

[14] Cai YR, Tang RK. Calcium phosphate nanoparticles in biomineralization and biomaterials. J Mater Chem 2008;18(32):3775-87.

[15] Ribeiro N, Sousa, SR, Monteiro FJ. Influence of crystallite size of nanophased hydroxyapatite on fibronectin and osteonectin adsorption and on MC3T3-E1 osteoblast adhesion and morphology. J Colloid Interface Sci 2010;351(2):398-406.

[16] Deligianni DD, Katsala ND, Koutsoukos PG, Missirlis YF. Effect of surface roughness of hydroxyapatite on human bone marrow cell adhesion, proliferation, differentiation, and detachment strength. Biomaterials 2001;22(1):87-96.

[17] Palin E, Liu H, Webster TJ. Mimicking the nanofeatures of bone increases bone-forming cell adhesion and proliferation. Nanotechnology 2005;16:1828-1835.

[18] Di Silvio L, Dalby MJ, Bonfield W. Osteoblast behavior on HA/PE composite surfaces with different HA volumes. Biomaterials 2002;23:101-107.

[19] Rey C, Combes C, Drouet C, Glimcher MJ. Bone mineral: update on chemical composition and structure. Osteoporos Int 2009;20(6):1013-21.

[20] Boskey AL. Bone mineral crystal size. Osteoporos Int 2003;14(S5):S16-S21.

[21] Lange C, Li C, Manjubala I, Wagermaier W, Kuhnisch J, Kolanczyk M, Mundios S, Knaus P, Fratzl P. Fetal and postnatal mouse bone tissue contains more calcium than is present in hydroxyapatite. J Struc Biol 2011;176(2):159-67.

[22] Kuhn LT, Grynpas MD, Rey C, Wu Y, Ackerman JL, Glimcher MJ. A comparison of the physical and chemical differences between cancellous and cortical bovine bone mineral at two ages. Calcif Tissue Int 2008;83(2):146-54.

[23] Donnelly E, Meridth DS, Ngyuyen JT, Gladnick BP, Rebolledo BJ, Shaffer AD, Lorich DG, Lane JM, Boskey AL. Reduced cortical bone compositional heterogeneity with bisphosphonate treatment in postmenopausal women with intertrochanteric and subtrochanteric fractures. J Bone Miner Res 2012;27(3):672-8.

[24] Rohanizadeh R, LeGeros RZ, Bohic S, Pilet P, Barbier A, Daculsi G. Ultrastructural properties of bone mineral of control and tiludronate-treated osteoporotic rat. Calcif Tissue Int 2000;67:330-6.

[25] Reichert JC, Quent VMC, Burke LJ, Stansfield SH, Clements JA, Hutmacher DW. Mineralized human primary osteoblast matrices as a model system to analyse interactions of prostate cancer cells with the bone microenvironment. Biomaterials 2010;31:7928-36.

[26] Jenkins R, Synder RL. Introduction to X-ray powder diffractometry. New York: John Wiley & Sons, 1996;123.

[27] Sanosh KP, Chu MC, Balakrishnan A, Kim TN, Cho SJ. Preparation and characterization of nano-hydroxyapatite powder using sol–gel technique. Bull Mater Sci 2009;32(5):465.

[28] Weiner S, Bar-Yosef O. States of preservation of bones from prehistoric sites in the near-east – a survey. J Archaeol Sci 1990;17(2):187-96.

[29] Termine JD, Posner AS. Infra-red determination of the percentage of crystallinity in apatitic calcium phosphates. Nature 1966;211:268-70.

[30] Blumenthal NC, Posner AS, Holmes JM. Effect of preparation conditions on the properties and transformation of amorphous calcium phosphate. Mater Res Bull 1972;7:1181-90.

[31] ICDD PDF: International Centre for Diffraction Data, Powder Diffraction File, Newtown Square, Pennsylvania, USA.

[32] Mahamid J, Sharir A, Addadi L, Weiner S. Amorphous calcium phosphate is a major component of the forming fin bones of zebrafish: indications for an amorphous precursor phase. PNAS 2008;105(35):12748-53.

[33] Pleshko N, Boskey A, Mendelsohn R. Fourier Transform Infrared Spectroscopy study of hydroxyapatite crystallinity. Biophys. J 1991;60(4):786-93.

[34] el Feki H, Rey C, Vignoles M. Carbonate ions in apatites: infrared investigations in the upsilon 4 CO_3 domain. Calcif Tissue Int 1991;49(4):269-74.

[35] Hu Q, Tan Z, Liu Y, Tao J, Cai Y, Zhang M, Pan H, Xu X, Tang R. Effect of crystallinity of calcium phosphate nanoparticles on adhesion, proliferation, and differentiation of bone marrow mesenchymal stem cells. J Mater Chem 2007;17:4690.

[36] Hahn BD, Lee JM, Park DS, Choi JJ, Ryu J, Yoon WH, Choi JH, Lee BK, Kim JW, Kim HE, Kim SG. Enhanced bioactivity and biocompatibility of nanostructured hydroxyapatite coating by hydrothermal annealing. Thin Solid Films 2011;519:8085-90.

[37] Shi Z, Huang X, Cai Y, Tang R, Yang D. Size effect of hydroxyapatite nanoparticles on proliferation and apoptosis of osteoblast-like cells. Acta Biomater 2009;5(1):338-45.

[38] LeGeros RZ, Trautz OR, Klein E, LeGeros JP. Two types of carbonate substitution in the apatite structure. Experientia 1969;25(1):5-7.

[39] Sauer GR, Wuthier RE. Fourier-transform infrared characterization of mineral phases formed during induction of mineralization by collagenase-released matrix vesicles *in vitro*. J Biol Chem 1988*;*263(27):13718–24.

[40] Panda RN, Hsieh MF, Chung RJ, Chin TS. FTIR, XRD, SEM and solid state NMR investigations of carbonate-containing hydroxyapatite nano-particles synthesized by hydroxide-gel techniques. J Phy Chem Solids 2002;64:193-9.

[41] Termine JD and Lundy DR. Hydroxide and carbonate in rat bone mineral and its synthetic analogs. Calcif Tissue Res 1973;13(1):73-82.

[42] Emerson WH and Fischer EE. The infra-red absorption spectra of carbonate in calcified tissues. Arch Oral Biol 1962;7:671-83.

[43] Elliot JC. Structure and chemistry of the apatites and other calcium orthophosphates. Elsevier 1961.

[44] Bertinetti L, Tampieri A, Landi E, Ducati C, Midgley PA, Coluccia S, and Martra G. Surface structure, hydration and cationic sites of nanohydroxyapatite: UHR-TEM, IR, and Microgravimetric studies. J Phys Chem C 2007;111:4027-35.

[45] Mercioniu I, Ciuca S, Pasuk I, Slav A, Morosanu, C Bercu, M. Thickness dependence of crystallization process for hydroxyapatite thin films. J Optoelectronics Adv M 2007;9(8):2535-38.

[46] Pathi SP, Lin DDW, Dorvee JR, Estroff LA, Fischbach C. Hydroxyapatite nanoparticle-containing scaffolds for the study of breast cancer bone metastasis. Biomaterials 2011;32(22):5112-22.

[47] Nelson DG. The influence of carbonate on the atomic structure and reactivity of hydroxyapatite. J Dent Res 1981;Spec No C:1621-9.

[48] Landi E, Celotti G, Logroscino G, Tampieri A. Carbonated hydroxyapatite as bone substitute. J Euro Soc 2003;23:2931-37.

[49] Moursi AM, Winnard AV, Winnard PL, Lannutti JJ, Seghi RR. Ehanced osteoblast response to a polymethylmethacrylate-hydroxyapatite composite. Biomaterials 2002;23:133–44.

[50] Yamada, K., Aota, S., Akiyama, A. and LaFlamme, S. Mechanisms of fibronectin and integrin function during cell adhesion and migration. Cold Spring Harb Symp Quant Biol 1992;57:203-12.

[51] Globus RK, Doty SB, Lull JC, Holmuhamedov E, Humphries MJ, Damsky CH. Fibronectin is a survival factor for differentiated osteoblasts. J Cell Sci 1998;111:1386-93

[52] Bentmann A, Kawelke N, Moss D, Zentgraf H, Bala Y, Berger I, Gasser Ja, Nakchbandi IA. Circulating fibronectin affects bone matrix, whereas osteoblast fibronectin modulates osteoblast function. J Bone Miner Res 2010;25(4):706-15.

CHAPTER 4
HYDROXYAPATITE NANOPARTICLE-CONTAINING SCAFFOLDS FOR THE STUDY OF BREAST CANCER BONE METASTASIS

Contributors: Siddharth Pathi, Jason Dorvee, Lara Estroff, Claudia Fischbach-Teschl

4.1 Abstract

Breast cancer frequently metastasizes to bone, where it leads to secondary tumor growth, osteolytic bone degradation, and poor clinical prognosis. Hydroxyapatite $Ca_{10}(PO_4)_6(OH)_2$ (HA), a mineral closely related to the inorganic component of bone, may be implicated in these processes. However, it is currently unclear how the nanoscale materials properties of bone mineral, such as particle size and crystallinity, which change as a result of osteolytic bone remodeling, affect metastatic breast cancer. We have developed a two-step hydrothermal synthesis method to obtain HA nanoparticles with narrow size distributions and varying crystallinity. These nanoparticles were incorporated into gas-foamed/particulate leached poly(lactide-co-glycolide) scaffolds, which were seeded with metastatic breast cancer cells to create mineral-containing scaffolds for the study of breast cancer bone metastasis. Our results suggest that smaller, poorly-crystalline HA nanoparticles promote greater adsorption of adhesive serum proteins and enhance breast tumor cell adhesion and growth relative to larger, more crystalline nanoparticles. Conversely, the larger, more crystalline HA nanoparticles stimulate enhanced expression of the osteolytic factor interleukin-8 (IL-8). Our data suggest an important role for nanoscale HA properties in the vicious cycle of bone metastasis and indicate that mineral-containing tumor models may be excellent tools to study cancer biology and to define design parameters for non-tumorigenic mineral-containing or mineralized matrices for bone regeneration.

*****Portions reproduced with permission from S.P. Pathi, D.D.W. Lin, J.R. Dorvee, L.A. Estroff, C. Fischbach, Biomaterials, **2011**, 32, 5112-5122. Copyright 2011 Elsevier.

4.2 Introduction

The bone microenvironment is defined by a composite matrix that consists primarily of organic collagen and inorganic mineral. Bone mineral is closely related structurally to geologic hydroxyapatite (HA) ($Ca_{10}(PO_4)_6(OH)_2$); however, bone apatites are less crystalline, more soluble, and vary in their molecular composition as carbonate ions often substitute for the hydroxide and phosphate ions ($Ca_{10-2x/3}(PO_4)_{6-x}(CO_3)_x(OH)_{2-x/3}$) [1]. Furthermore, the size and crystallinity of bone apatite crystals change during development, growth, and as a result of bone pathologies [2, 3]. While HA is largely known for its role in conferring structural and mechanical properties to bone, it also functions as a bioactive material that directly regulates the behavior of both normal and transformed cells [4, 5]. For example, HA has been shown to enhance normal bone formation [6] and to alter growth and expression profiles of bone metastatic tumors [5, 7]. Nevertheless, it remains unclear whether or not apatite crystal properties directly modulate the pathogenesis of bone diseases, in general, and bone metastasis, in particular. This lack of understanding is partly due to a paucity of culture systems that recreate 3-D tumor microenvironmental conditions to study changes in tumor cell behavior as a function of varying HA nanoscale properties. Therefore, we sought to utilize synthetically prepared HA nanoparticles to determine the impact of particle size and crystallinity on mammary cancer cell activity.

The vast majority of advanced stage breast cancers metastasize to the skeleton, forming secondary tumors and interfering with bone remodeling to create predominantly osteolytic lesions [8]. These lesions can lead to severe bone pain, pathological fracture, hypercalcaemia, and an overall poor clinical prognosis [9]. Osteolysis due to bone metastasis is linked to tumor-derived soluble factors, such as interleukin-8 (IL-8) and parathyroid hormone related peptide

(PTHrP), that de-couple the homeostatic balance between bone formation and bone resorption [8, 10]. In particular, IL-8, a molecular mediator of osteolysis [5, 10] and tumor progression [11, 12], is dramatically upregulated in breast cancer tissue relative to normal breast tissue in patients [13], and in breast cancer cells that preferentially metastasize to bone rather than lungs [14].

Though the exact mechanisms by which breast cancer cells preferentially target bone and induce pathological remodeling remain unclear, mounting evidence implicates the bone microenvironment and specifically HA in this pathogenesis. For example, mammary tumor cells increase expression of osteoclastogenic factors upon colonizing bone *in vivo* [14]. Additionally, IL-8 secretion by breast cancer cells is enhanced through cell-HA interactions, and stimulates osteoclast-mediated osteolysis [5, 10]. These studies illustrate the important role that bone mineral might play in influencing osteolytic metastasis. Since the size and crystallinity of biogenic apatite nanocrystals change as a function of age and disease [2, 3], further study is required to evaluate the role of these nanoscale properties of HA itself on metastatic bone disease.

Tissue engineered (TE) systems, originally created for regenerative medicine, can be used as tools to recreate tumor microenvironmental conditions *in vitro*. Tumor cells seeded in scaffold-based TE systems assemble into tumor-like tissues [11] and exhibit phenotypes that more closely mimic *in vivo* behavior as compared to conventional two-dimensional (2-D) cultures [7]. Furthermore, biologically active materials or molecules, such as mineral particles or proteins, can be incorporated into TE scaffolds and presented to cells in a spatially controlled manner [15]. Bone-like TE systems, including silk-based scaffold systems [16], decellularized osteoblast matrices [7], and polymer-HA composites [5, 6, 17] have been created to mimic certain features of bone, and several of these systems have been used to study tumor cell

behavior [5, 7]. Since bone metastasis can modify the crystallinity and particle size of the mineral component of bone [2], a controllable platform is needed to independently interrogate cellular responses to a wide range of HA particle sizes and crystallinities in a pathologically-relevant culture microenvironment.

4.3 Materials and Method

4.3.1 Particle Preparation

HA nanoparticles were synthesized through a two-step process in which a typical precipitation reaction of a calcium salt with a phosphate salt was followed by hydrothermal aging of the precipitate to obtain particles with a narrow size distribution (Fig. 4.1).

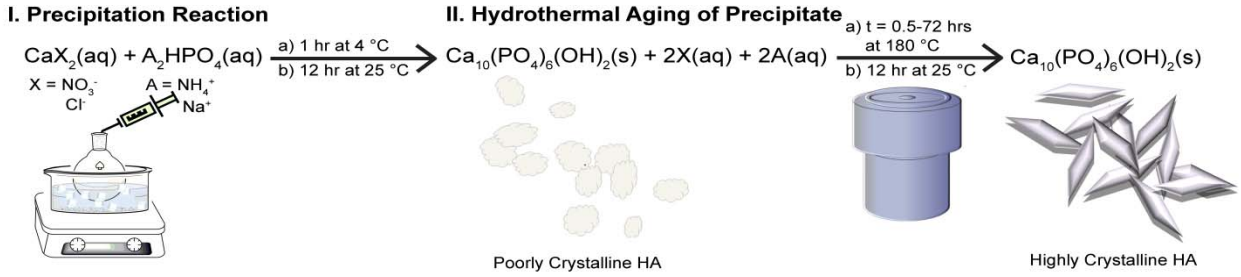

Figure 4.1: HA nanoparticle synthesis schematic showing the two-step precipitation reaction to obtain poorly crystalline HA followed by hydrothermal aging of the precipitate to obtain crystalline HA nanoparticles.

All chemicals for these reactions were obtained from Sigma Aldrich and used as received. A solution of $(NH_4)_2HPO_4$ (90 mL, 10 mM) was added drop-wise into a solution of $Ca(NO_3)_2$ (150 mL, 10 mM) under rapid stirring at 4 °C in an ice-water bath for a final calcium to phosphate ratio of 1.67 (A1-A3 particles). The pH of the starting solutions was adjusted to 9-9.5 with 0.1 M

NH_4OH. In a second reaction, particles were synthesized from a different set of precursors. A solution of Na_2HPO_4 (90 mL, 10 mM) was added drop-wise into a solution of $CaCl_2$ (150 mL, 10 mM) under rapid stirring at 4 °C until the calcium to phosphate ratio was 1.67 (B1 particles). The pH of the starting solutions was adjusted to 9-9.5 with 0.1 M NaOH. In both cases, the reactions were allowed to proceed for 1 hr, and then stirred at 20 °C for an additional 12 hrs. The resulting opaque suspensions were concentrated 3-fold by centrifugation (Thermo Scientific Sorvall Legend RT+ Centrifuge, 3600 g, 5 min) of 45 mL aliquots. After centrifugation, two-thirds of the clear supernatant was decanted. The remaining suspension (15 mL) was sonicated for 30 mins (Bransonic 1510R-MT), placed into a pressure vessel (Parr Instrument Company 276AC-7304), and aged at 180 °C for the indicated time periods (Table 4.1) in an oven (model no. OV12A, GS Blue M Electric). After aging, the particles were removed from the pressure vessel, washed with NH_4OH (0.1 M) and deionized water (DI-H_2O) to remove soluble salts, rinsed with acetone, and then dried at 20 °C (A2, A3, and B1 particles). Poorly crystalline particles were collected following the precipitation reaction of $Ca(NO_3)_2$ and $(NH_4)_2HPO_4$. The precipitate was washed with NH_4OH and DI-H_2O, rinsed with acetone, and dried at 20 °C (A1 particles). Commercial HA nanopowder obtained from Sigma Aldrich (provider specified particle size <200 nm) was used for comparison.

4.3.2 Particle Characterization

Particles were characterized by Transmission Electron Microscopy (TEM) for shape and morphology, and X-ray Diffraction (XRD) and Fourier Transform Infrared (FTIR) Spectroscopy for crystallinity and phase information. For TEM, particles were suspended in acetone and dropped onto a carbon-coated grid (Electron Microscopy Sciences). Samples were examined by

brightfield TEM (FEI Tecnai T-12 Spirit, 120 kV), and particle sizes were determined by image analysis of the TEM images through ImageJ (NIH). Dried particles were examined via powder XRD (PAD-X theta-theta X-ray Diffractometer, Scintag Inc., CuKα 1.54 Å, accelerating voltage 45 kV, current 40 mA, continuous scan, 2.0 deg/min). Particle sizes were determined from the peak broadening of the {002}peak of HA (25.88°) by application of the Scherrer equation using a Al_2O_3 standard (Software: JADE 9, Materials Data, Inc.). For FTIR (2020 Galaxy Series FT-IR, Mattson Instruments), KBr pellets were prepared from dried particles and spectra acquired (res 4.0 cm^{-1}, 253 scans). Particle crystallinities were determined from the splitting factor obtained via normalizing the sum of the absorbance at 562 cm^{-1} and 600 cm^{-1} to the minimum between the doublet following Weiner and Bar-Yosef [18].

4.3.3 Scaffold Fabrication

Porous mineral-containing scaffolds were fabricated by a gas-foaming/particulate leaching technique as previously described [5, 6]. Briefly, 4 mg of poly(lactide-co-glycolide) (PLG) particles (Lakeshore Biomaterials, ground and sieved, average diameter 250 μm), 4 mg of PLG microspheres (formed through a double emulsion process, average diameter 5-50 μm), 8 mg of HA nanoparticles (A1-A3, B1, SIG), and 152 mg of NaCl (J.T. Baker, sieved to a diameter of 250-400 μm) were mixed and subsequently cold pressed in a Carver Press (Fred S. Carver). The resulting matrices (8.5 mm diameter, 1 mm in thickness) were exposed to high-pressure carbon dioxide gas (800 psi) inside a non-stirred pressure vessel (Parr Instruments 4677). Following rapid release of pressure that allowed polymer foaming, scaffolds were soaked in de-ionized water for 24 hrs to leach out porogenic NaCl particles. Non-mineral-containing

(NM) scaffolds that did not contain HA were also fabricated as controls. Prior to cell culture, scaffolds were sterilized in 70% ethanol for 30 min and washed five times in sterile PBS.

4.3.4 Microscopic Characterization of Scaffolds

Scaffolds were characterized through TEM, scanning electron microscopy (SEM) and brightfield light microscopy to assess particle distribution throughout the polymer matrix. For TEM (FEI Tecnai T-12 Spirit, 120 kV), scaffolds were embedded in a UV-active Quetal resin (EM Sciences, Fort Washington, PA) and sectioned with a microtome (MT2-B Ultra-Microtome, Sorvall Porter-Blum) prior to analysis. For SEM, scaffolds were fractured to expose inner pore surfaces and mounted on aluminum SEM stubs (Electron Microscopy Sciences) with carbon tape in a manner that allowed subsequent imaging of the exposed surfaces. Particle distribution on PLG surfaces were examined on exposed pore surfaces within the scaffold that were unaffected by the sample preparation (i.e., not on the fractured surface) and imaged uncoated using a Field-Emission SEM (Zeiss LEO 1550, 1 kV). Brightfield microscopy of scaffolds was performed on an Axio Observer.Z1 (Zeiss).

4.3.5 Analysis of Protein Adsorption on Scaffolds

To quantify the degree of protein adsorption as a function of HA nanoparticle characteristics, scaffolds were incubated in complete DMEM (cDMEM ; i.e., DMEM [Invitrogen] supplemented with 10% fetal bovine serum [Tissue Culture Biologicals] and 1% penicillin/streptomycin [Invitrogen]). Following 30 min of incubation, scaffolds were washed twice in PBS (Invitrogen) and then sonicated (Branson Sonifier 150) in RIPA buffer (Sigma).

After centrifugation, total protein in the supernatant was quantified using a Bicinchonic Acid (BCA) Kit (Thermo) and colorimetric analysis on a plate reader (Tecan M1000) according to manufacturer's instructions. Additionally, scaffolds were incubated in DMEM supplemented with 20 μg/mL of fibronectin (Sigma) and adsorbed fibronectin was analyzed by immunofluorescence. Briefly, scaffolds were fixed with 10% formalin, rinsed twice in PBS, and then incubated with a polyclonal rabbit anti–fibronectin antibody (Sigma). After a second wash with PBS containing bovine serum albumin, scaffolds were incubated with an Alexa Fluor 488 secondary antibody (Molecular Probes). Whole-mount scaffolds were imaged using an epi-fluorescence microscope (Zeiss Axio Observer.Z1).

4.3.6 Cell Culture

Human MDA-MB231 breast cancer cells (ATCC) were maintained under standard culture conditions (37°C, 5% CO_2) in cDMEM. For 3-D cell culture, scaffolds were statically seeded with 1.5 million MDA-MB231 cells and subsequently maintained under dynamic culture conditions on an orbital shaker for up to 10 days as previously described [5].

4.3.7 Analysis of Ion Content in Media from Scaffolds

To determine changes in calcium and phosphate content in media during culture, acellular NM- and A1-scaffolds were incubated in cDMEM under standard culture conditions (37°C, 5% CO_2). The media was harvested after 2 days, digested in 5% nitric acid, and analyzed with inductively coupled plasma spectroscopy (ICP; ICAP 61E Trace Analyzer, Thermo).

Additionally, ICP analysis was performed with media harvested from tumor cell-seeded NM- and A1-scaffolds after 2 days of 3-D culture.

4.3.8 Characterization of Tumor Cell Behavior

To measure tumor cell growth, tumor constructs were harvested 30 min after seeding (day 0) and again after 72 hrs. Constructs were washed five times in PBS and mechanically disintegrated, before being sonicated (Branson Sonifier 150) in lysis buffer (25 mM Tris-HCl, 0.4 M NaCl, 0.5% SDS). Subsequently, lysates were centrifuged, and the supernatant was assayed for DNA content using PicoGreen® assay (Invitrogen) and a fluorescence plate reader (Tecan M1000) according to manufacturer's instructions. Protein secretions in media from constructs were also analyzed 72 hrs after seeding. Briefly, breast cancer cell-seeded scaffolds were transferred to fresh well plates 24 hrs prior to harvesting media for analysis, and culture medium was changed to DMEM containing 1% FBS. IL-8 of harvested media was measured via ELISA (R&D) according to manufacturer's instructions and normalized to DNA content to account for differences in cell number. For analysis of IL-8 expression, RNA was collected by dissolving tumor cell-seeded scaffolds in TRIzol® (Invitrogen) and then extracting total RNA according to manufacturer protocol. Total RNA (1 μg) was then reverse transcribed to cDNA (High Capacity cDNA Reverse Transcription Kit with random hexamers [(Applied Biosystems)]), and subjected to real-time RT-PCR (25 ng template, run in triplicate) using SYBR green detection (Quanta) on an Applied Biosystems 7500 System. Primer sequences for human IL-8 (fwd: 5'-agaaaccaccggaaggaaccatct-3', rev: 5'-agagctgcagaaatcaggaaggct-3') and β-actin (fwd: 5'-aatgtggccgaggactttgattgc-3', rev: 5'-aggatggcaagggacttcctgtaa-3') were

synthesized by IDT Technologies. β-actin was used as an endogenous loading control gene, and relative quantification was performed using the $\Delta\Delta C_t$ method as previously described [19].

4.3.9 Statistical Analysis

One-way ANOVA and Student's t-test were used to determine statistical significance between conditions. Tukey's post test was used for pairwise comparisons. Significance between groups and NM, A2, and B1 scaffolds (see Table 1) are denoted by (*), (#), and (o) respectively. In all cases, $P<0.01$ is indicated by a single symbol and $P<0.005$ is denoted by double symbols. For all experiments, sample conditions were run in triplicate or greater. Data are presented as averages, and error bars represent standard deviations.

4.4 Results

4.4.1 Particle Synthesis and Characterization

Synthetic HA (sHA) with varying nanoscale characteristics can be formed via solution-based precipitation reactions, hydrothermal synthesis, electrodeposition, or sintering [1, 20]. The sHA nanoparticles used for the fabrication of mineral-containing scaffolds were obtained from either a two-step synthesis involving a precipitation reaction followed by hydrothermal aging or a commercial source for comparison (Fig. 4.1, Table 4.1). To synthesize poorly crystalline particles (A1), solutions of calcium and phosphate salts were mixed together rapidly at low temperature. Remaining particles (A2, A3, and B1) were prepared by hydrothermally aging a suspension of the particles from the precipitation reaction. The size and crystallinity of the

particles increased with aging time (A2, A3), and could also be varied by changing the precursor salts (B1).

Particle shape and size distributions of both the sHA and commercial HA were determined by TEM (Fig. 4.2).

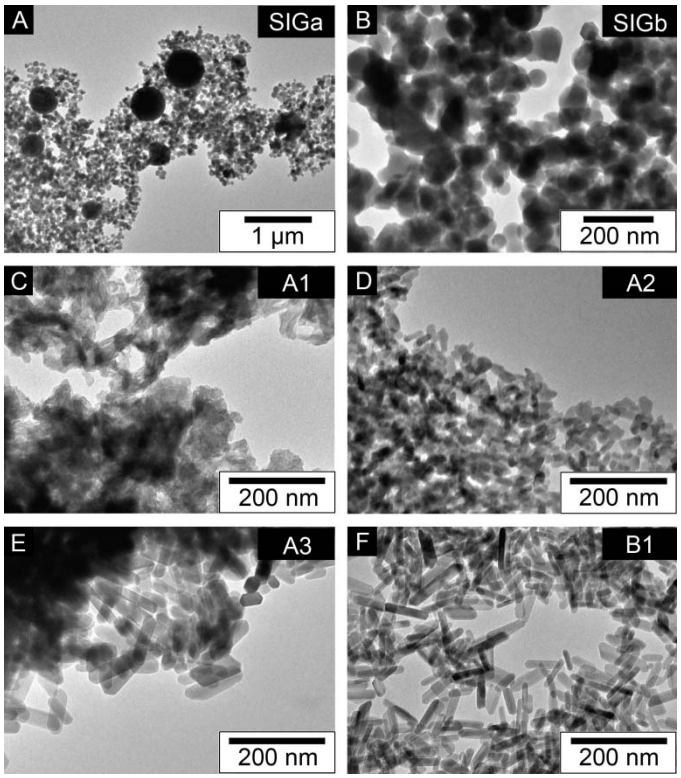

Figure 4.2: TEM images of the different HA particles used to prepare mineral-containing PLG-scaffolds: Commercial Sigma Aldrich particles, (shown at low [SIGa], and high [SIGb] magnification), HA particles synthesized from $Ca(NO_3)_2$ and $(NH_4)_2HPO_4$ precursors with hydrothermal aging times of 0 hrs (A1), 0.5 hrs (A2), and 72 hrs (A3), and particles synthesized from $CaCl_2$ and Na_2HPO_4 precursors aged for 1.5 hrs (B1).

The sHA particles that were formed from the initial precipitation reaction (A1) were small and poorly crystalline; however, hydrothermally aging these same particles resulted in the formation of uniform, larger, faceted, and elongated particles with a narrow size distribution (A2 and A3). Similar to previous observations [1], the length of the rod-like particles increased with aging

time from 20-40 nm after 0.5 hrs of aging (A2) to 60-170 nm after 72 hrs of aging (A3). Using a different set of precursor salts and shorter aging time (1.5 hrs), rod-like particles (B1), with lengths similar to A3 (50-150 nm), were also obtained. In contrast to the sHA particles, the SIG particles were spherical and exhibited a wide range of sizes (20-600 nm in diameter).

All of the synthetic particles were pure HA according to powder X-ray diffraction (pXRD) (Fig. 4.3). The diffraction pattern of the SIG particles, however, contained unidentified peaks in addition to those indexed to HA (ICDD PDF no. 09-0432). The pXRD also provides information regarding the particle size and crystallinity. Scherrer analysis of the {002} peak width (25.88°) revealed that the average length of the particles to be 24 nm (A1), 32 nm (A2), 103 nm (A3), 100 nm (B1), and 125 (SIG) (Table 4.1). The increase in the number of clearly resolvable peaks at higher angles for A3 and B1 particles suggest an increase in crystallinity compared to A1 and A2 particles.

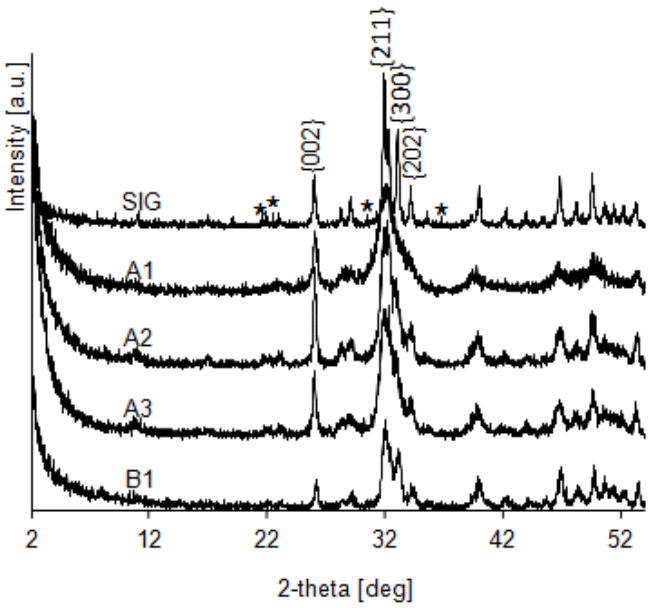

Figure 4.3: pXRD patterns of particles SIG, A1-A3, and B1. All samples are confirmed to be HA. Major peaks have been labeled with HA crystal indices. Peaks not characteristic of HA pXRD pattern in SIG are indicated by (*). (ICDD PDF no. 09-0432)

FTIR results confirmed the increase in crystallinity for the larger particles obtained from longer hydrothermal aging times and varying precursor salts (A3, B1). The absorbance at 630 cm^{-1} is attributed to structural hydroxides in HA and is known to increase with enhanced crystallinity (Fig. 4.4) [21]. This absorbance was undetectable for the poorly crystalline HA (A1), and increased in intensity for nanoparticles A2, A3, and B1. The increase in crystallinity was further confirmed from calculation of the splitting factor (Table 4.1). The splitting factor, which quantifies the degree of splitting of the PO_4 bond bending (ν_4) peaks (562 cm^{-1} and 600 cm^{-1}), is known to increase with increasing crystallinity [18]. Interestingly, although A3 and B1 are similar in length, B1 had nearly twice as large a splitting factor, indicating differences in crystallinity between the two similarly sized particles made from different precursor salts (Table 4.1).

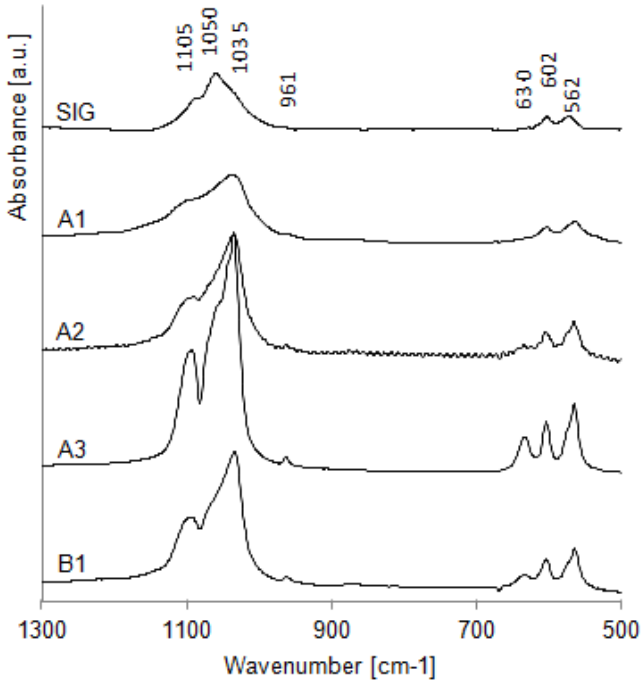

Figure 4.4: FTIR spectra of particles SIG, A1-A3, and B1. Positions of characteristic HA peaks are indicated.

Table 4.1: Summary of particle characterization, detailing precursor material, hydrothermal aging time, size of particles determined via TEM and XRD, and splitting factor determined via FTIR.

Sample ID	Precipitation Precursors	Aging time [h]	Length [nm][a] (TEM)	Bulk Length [nm][b] (pXRD)	Splitting Factor (FTIR)[c]
SIG	Commercial Sigma	N/A	20-600	125	2.07
A1	$Ca(NO_3)_2$, $(NH_4)_2HPO_4$	0	---	24	2.56
A2	$Ca(NO_3)_2$, $(NH_4)_2HPO_4$	0.5	20-40	32	3.61
A3	$Ca(NO_3)_2$, $(NH_4)_2HPO_4$	72	60-170	103	3.99
B1	$CaCl_2$, Na_2HPO_4	1.5	50-150	99	6.60

[a]The range of particle lengths observed from TEM micrographs along the *c*-axis. Lengths of A1 particles could not be determined from TEM.
[b]Average lengths of the particles were obtained via Scherrer analysis of the {002} peak from pXRD.
[c]Splitting factors were obtained from FTIR spectra by normalizing the sum of the absorbance at 562 cm^{-1} and 602 cm^{-1} from PO_4 bond bending (ν_4) to the minima between the two peaks.

4.4.2 Scaffold Characterization

The micro- and nano-architecture of the scaffolds was analyzed via brightfield light microscopy, SEM and TEM. Mineral-free (NM-scaffolds), SIG-scaffolds, and A3-scaffolds were compared to assess the integration of different particles into the bulk-PLG. Incorporation of the SIG and A3 nanoparticles did not change the microarchitectural characteristics (i.e., pore size and wall thickness) of the scaffolds compared to the NM-scaffold as shown by brightfield light microscopy (Fig. 4.5).

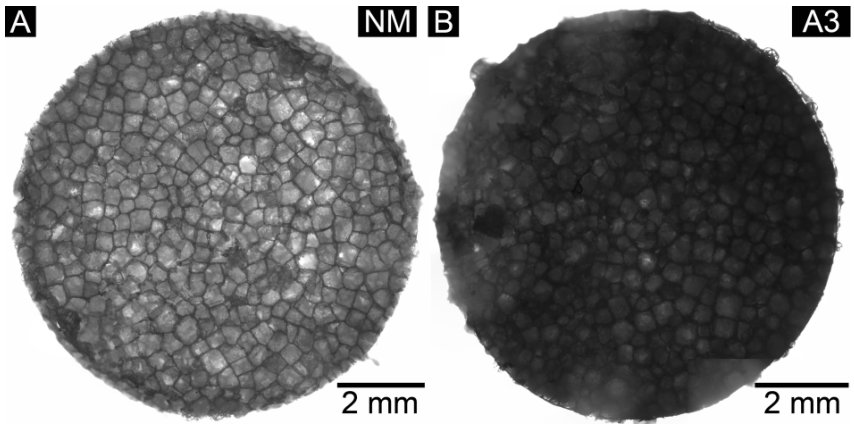

Figure 4.5: Light microscope images showing the pore distribution of NM-scaffold (A) and A3-scaffold (B).

The distribution of both A3 and SIG particles on pore surfaces within the scaffolds was revealed by SEM micrographs. Despite the differences in particle morphology, similar surface coverage was observed for both the rod-like A3 particles and spherical SIG particles. Both scaffold types contained regions of high and low particle density, as well as areas without surface-associated HA (Fig. 4.6). High magnification SEM images of the A3 and SIG scaffolds (Fig. 4.6C, D) further illustrated that the surface topography is dictated by the morphology of the incorporated particles and reflects the rod-like and spherical morphology of A3 and SIG particles.

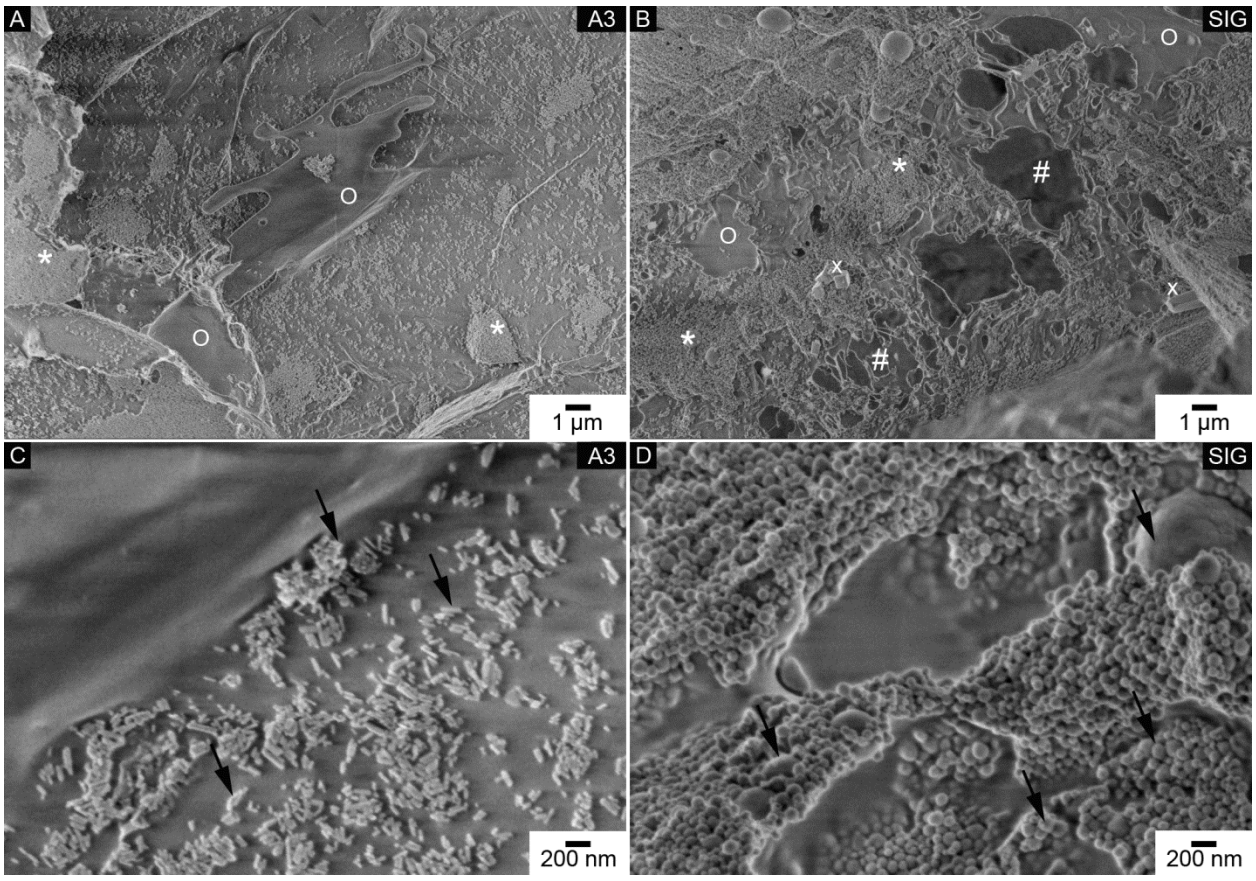

Figure 4.6: SEM micrographs of A3-scaffold (A, C) and SIG-scaffold (B,D) show the distribution of A3 and SIG particles on pore surfaces exposed after fracture of a scaffold. Regions of high particle density (*), low particle density (O), and pores in the scaffold (#) were observed for both scaffolds (A, B). Residual salt crystals are indicated (x). Arrows point to individual A3 particles (C) and SIG particles (D).

TEM micrographs of sectioned A3-scaffolds revealed that HA particles were localized at or near the pore surfaces, with a small number of particles completely embedded within the bulk-PLG (Fig. 4.7). This distribution of particles suggests that a majority of the particles are accessible for interaction with seeded cancer cells.

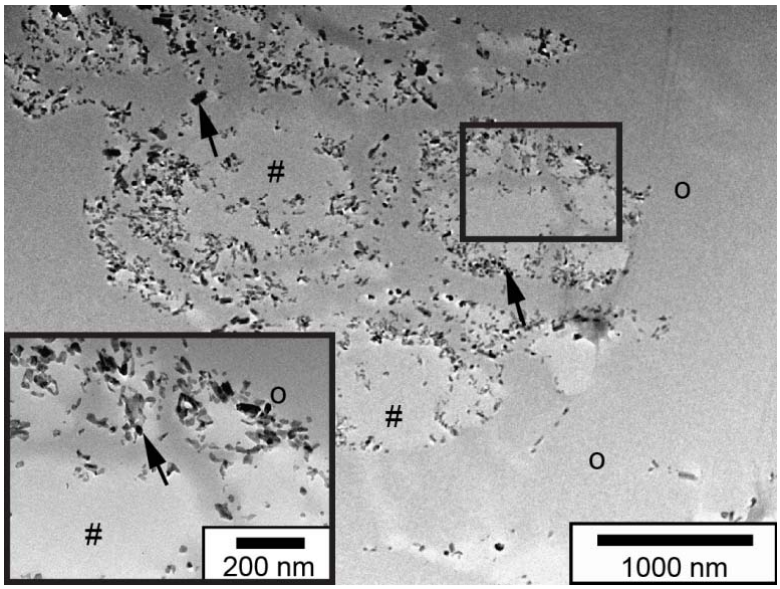

Figure 4.7: TEM micrograph of an A3-scaffold shows the distribution of the particles (indicated by arrows) in the bulk (indicated by 'O') and the pores (indicated by '#') of the polymeric matrix. Inset: Higher magnification image of the area indicated by a box.

4.4.3 Serum Protein Adsorption

To assess whether the HA nanoscale characteristics modulate cellular interactions with scaffolds, we next determined the capacity for protein adsorption of the different mineral-containing scaffolds. When incubated in serum-containing media (DMEM + 10% FBS), mineral-containing scaffolds adsorbed significantly more protein than control NM-scaffolds, and furthermore, the scaffolds with the smallest and least crystalline HA nanoparticles (A1) adsorbed

the most serum proteins, as determined by a colorimetric assay (Fig. 4.8A). Specifically, scaffolds with poorly crystalline particles (A1) adsorbed two-fold more serum protein as scaffolds with 103 nm long particles (A3). Furthermore, A3-scaffolds adsorbed significantly more protein than the more crystalline B1 scaffolds, yet these two particles did not vary in size. Incubating scaffolds in pure solutions of fibronectin, an adhesive serum protein that readily adsorbs onto most biomaterial surfaces [22], yielded similar trends as indicated by fibronectin immunofluorescence (Fig. 4.8B).

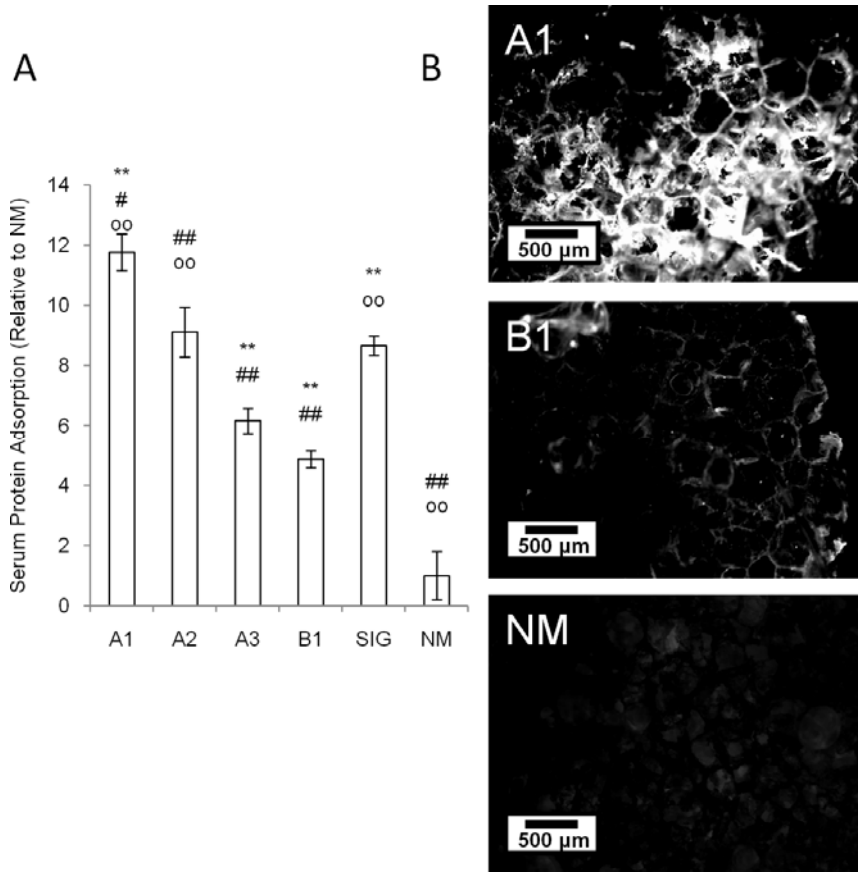

Figure 4.8: (A) Serum protein adsorption on non-mineral-containing (NM) and mineral-containing (A1-A3, B1, SIG) scaffolds as quantified via colorimetric BCA analysis of scaffold lysates prepared after incubation with serum-containing cell culture media. (B) Immunofluorescence analysis of fibronectin (FN) adsorption onto non-mineral-containing (NM) and mineral-containing scaffolds containing small, poorly crystalline (A1) and highly crystalline HA particles (B1). Significance between groups and NM, A2, and B1 scaffolds are denoted by (*), (#), and (o) respectively. In all cases, $P<0.01$ is indicated by a single symbol and $P<0.005$ is denoted by double symbols.

To control for changes in surface area as a function of particle size and/or shape, fibronectin adsorption experiments were repeated with scaffolds containing HA nanoparticles in amounts normalized to surface area. Under these conditions, scaffolds containing smaller, poorly crystalline nanoparticles (i.e. 20 nm long) adsorbed significantly more fibronectin relative to those with longer, more crystalline particles (i.e. 80 nm and 100 nm long) (Fig. 4.9A).

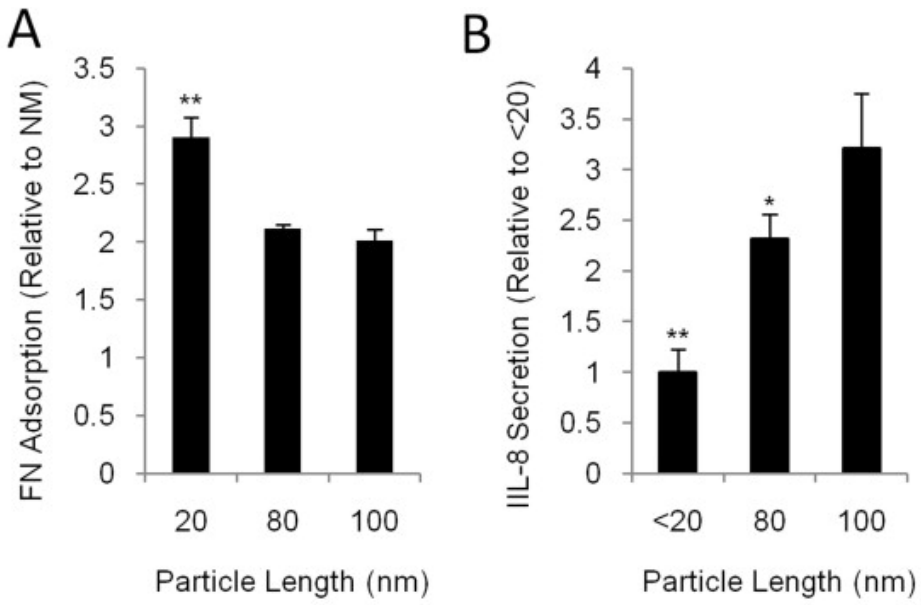

Figure 4.9: Effect of HA nanoparticle characteristics on fibronectin adsorption (A) and IL-8 secretion (B) following surface normalization. Separate sets of hydrothermally prepared nanoparticles were used for each experiment and the amount of HA in each scaffold was normalized to surface area assuming a prismatic geometry with lengths and widths estimated from TEM micrographs. (A) Fibronectin (FN) adsorption on mineral-containing scaffolds as determined via colorimetric analysis of scaffold lysates prepared after incubation with fibronectin solution. (B) IL-8 secretion by MDA-MB231 breast cancer cells as analyzed through ELISA of conditioned media collected from mineral-containing scaffold cultures. IL-8 levels were normalized to cell numbers as determined via PicoGreen DNA assay to account for changes in cell proliferation. Significance between groups and 100 nm particle lengths are denoted by (*). In all cases, $P<0.01$ is indicated by a single symbol and $P<0.005$ is denoted by double symbols.

These results suggest that HA particle characteristics, in addition to purely surface area, regulate the adsorption of serum proteins that may in turn modulate cell behavior.

4.4.4 Scaffold and Particle Integrity in Culture Conditions

To determine if HA nanoparticle solubility contributes to calcium and phosphate content in media, which during cell culture could lead to differences in cell behavior, the elemental composition of media harvested from scaffolds was analyzed via ICP (Fig. 4.10).

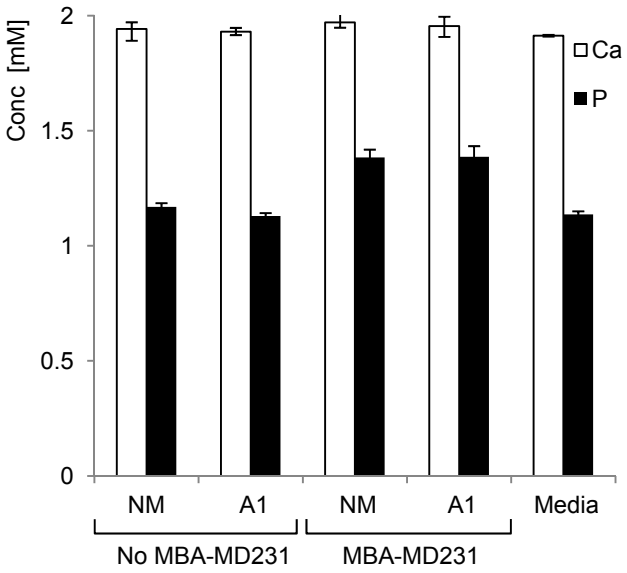

Figure 4.10: Calcium (white) and phosphorus (black) content of media harvested from non-mineral-containing (NM) and mineral-containing (A1) scaffolds after 2 days of culture in the presence and absence of MDA-MB231 breast cancer cells as determined by ICP. Culture media incubated for the same period of time, but not exposed to scaffolds or cells was used as a control (Media).

A1-scaffolds were used for this experiment since poorly crystalline HA has increased solubility compared to more crystalline HA [1] and would be most susceptible to potential dissolution. Analysis was performed on both cell-seeded and cell-free scaffolds, revealing that the calcium

concentrations remained unchanged for all conditions and matched concentrations found in cDMEM. Similarly, non-seeded scaffolds exhibited unfettered phosphorous levels equal to concentrations found in cDMEM. In contrast, phosphorus concentrations increased for both the NM and A1-scaffolds that were seeded with cells. This increase was attributed to the presence of the cancer cells rather than the dissolution of HA particles. Overall, our findings show that any observed effects of mineral-containing scaffolds on cell behavior are related to cell-material interactions with HA nanoparticles and not the presence of increased levels of soluble calcium and phosphorous.

4.4.5 Effect of HA Crystallinity and Particle Size on MDA-MB231 Adhesion and Growth

To determine the relevance of mineral characteristics to breast cancer cell colonization and growth within bone, we seeded MDA-MB231 breast cancer cells into mineral-containing PLG scaffolds and evaluated their adhesion and proliferation as a function of HA nanoparticle characteristics. In comparison to NM scaffolds, all of the mineral-containing scaffolds enabled significantly more cell adhesion as detected by DNA quantification following initial cell seeding (Fig. 4.11A). Similar to the increased protein adsorption (Fig. 4.8), cell adhesion was greatest within scaffolds containing small, poorly-crystalline nanoparticles (A1) as compared to larger and more crystalline HA scaffolds (A2, A3, and B1) suggesting a possible link between HA-regulated protein adsorption and cell adhesion. Likewise, significantly more cells adhered to A3 scaffolds than B1 scaffolds, suggesting that increased HA crystallinity inhibits breast cancer cell adhesion by suppressing protein adsorption. Importantly, tumor cell proliferation was also affected by the presence of different HA nanoparticles and followed similar trends as observed for cell adhesion (Fig. 4.11B).

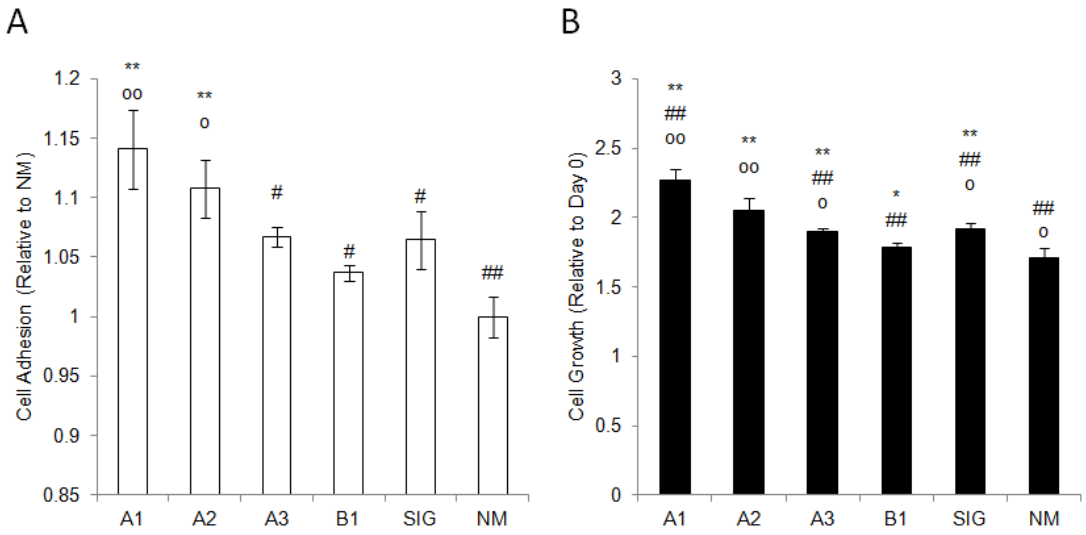

Figure 4.11: (A) MDA-MB231 cell adhesion onto non-mineral-containing (NM) and mineral-containing scaffolds (A1-A3, B1, SIG) as quantified via PicoGreen DNA assay of cell lysates 3 hours after seeding. (B) MDA-MB231 growth 3 days after seeding of non-mineral-containing (NM) and mineral-containing scaffolds (A1-A3, B1, SIG) as analyzed by PicoGreen DNA assay. Values are depicted relative to day 0 to account for variations in initial cell adhesion between the individual groups. Significance between groups and NM, A2, and B1 scaffolds are denoted by (*), (#), and (o) respectively. In all cases, $P<0.01$ is indicated by a single symbol and $P<0.005$ is denoted by double symbols.

4.4.6 IL-8 Secretion by MDA-MB231 Cells as a Function of HA Crystallinity and Particle Size

To evaluate the effect of HA nanoparticle characteristics on the osteolytic capability of breast cancer cells, we analyzed IL-8 secretion by MDA-MB231 cells in the different scaffolds. Interestingly, in contrast to cell adhesion and proliferation, IL-8 secretion was inversely regulated by HA crystallinity and size. Specifically, cellular secretion of IL-8 was greatest in scaffolds that incorporated highly crystalline HA (B1) (Fig. 4.12A), while scaffolds that contained similarly sized, but less crystalline HA (A3) secreted significantly less IL-8. Furthermore, tumor cells cultured in scaffolds with the smaller and less crystalline particles (A1, A2) secreted less IL-8 relative to the highly crystalline particles (B1). These changes in secretion

were mimicked at the expression level, as real-time RT-PCR demonstrated upregulation of IL-8 in cells seeded in scaffolds containing larger HA crystals as compared to less crystalline HA conditions or NM controls (Fig. 4.12B).

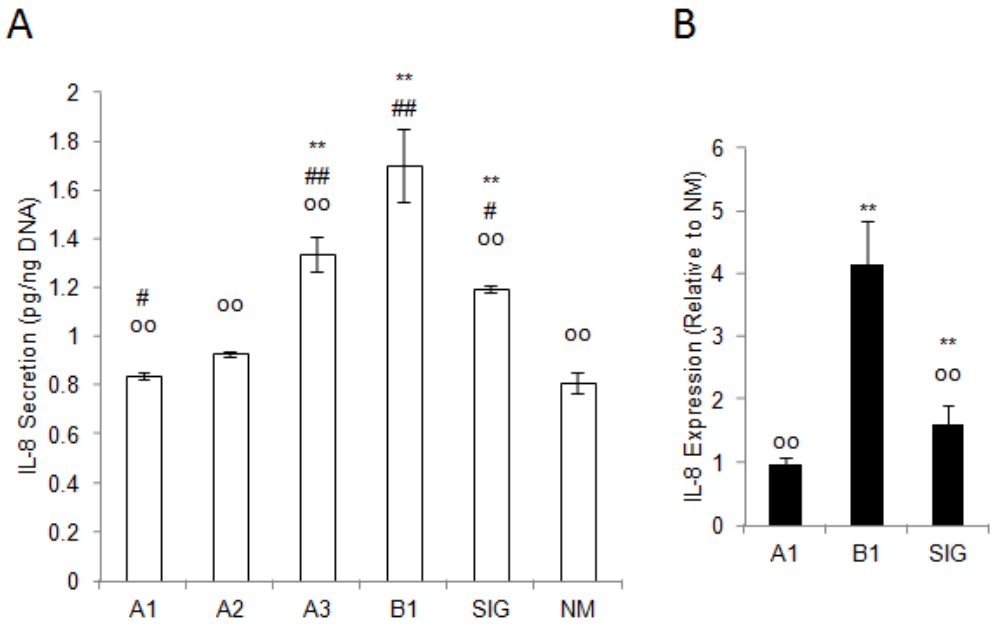

Figure 4.12: (A) IL-8 secretion by MDA-MB231 breast cancer cells as analyzed through ELISA of conditioned media collected from non-mineral-containing (NM) and mineral-containing scaffold cultures (A1-A3, B1, SIG). Values were normalized to cell numbers as determined via PicoGreen DNA assay to account for changes in cell proliferation. (B) IL-8 mRNA expression by MDA-MB231 breast cancer cells as analyzed through quantitative real-time RT-PCR of lysates collected from non-mineral-containing (NM) and representative mineral-containing scaffold cultures (A1, B1, SIG). Values are shown as normalized to expression levels in NM scaffold cultures. Significance between groups and NM, A2, and B1 scaffolds are denoted by (*), (#), and (o) respectively. In all cases, $P<0.01$ is indicated by a single symbol and $P<0.005$ is denoted by double symbols.

To confirm that these outcomes resulted from nanoparticle characteristics and not a change in surface area due to particle size and/or shape, experiments were repeated with scaffolds containing HA nanoparticles in amounts normalized to surface area. In these experiments, the scaffolds containing larger, more crystalline HA still increased IL-8 secretion (Fig. 4.9B). Taken

together, these data suggest a role of HA nanoparticle characteristics, beyond size, in regulating the osteolytic potential of MDA-MB231 breast cancer cells.

4.5 Discussion

Since bone metastasis often leads to the formation of osteolytic lesions [8] that are characterized by less crystalline and smaller apatite particles relative to healthy bone [2], studies of breast cancer bone metastasis would benefit from HA-containing scaffold systems in which particle size and crystallinity can be independently varied. While 3-D culture approaches have enhanced the physiological relevance of *in vitro* studies [11, 23], models to investigate cell-mineral interactions in response to specific HA nanoparticle characteristics currently do not exist. Commercially available HA particles, which are routinely employed for the fabrication of mineral-containing scaffolds [5, 6], are heterogeneous in size, shape, and chemical composition as shown by us (Fig. 2A, B) and others [24]. Gas-foamed/particulate-leached polymer composite scaffolds have previously been used to effectively present mineral to cultured cells [5, 6], and we have applied this platform to present hydrothermally grown HA particles with tunable nanoscale characteristics to cells in a 3-D culture context. Specifically, we have used these scaffolds to study the effects of HA particle size and crystallinity on breast cancer cell behavior and have demonstrated that altering the crystal properties of HA may control the osteolytic and metastatic phenotype of breast cancer cells.

Several methods have previously been used to synthesize HA nanoparticles with narrow size distributions [20, 25]. Many of these methods depend on the presence of surfactants or fractionation to control the size distribution, and the resulting particles have organic impurities

and are produced in low yields [26, 27]. Here, we describe an optimized technique for the synthesis of HA nanoparticles, which does not require additives or elaborate separation techniques to obtain narrow size distributions. The two-step process involves a wet chemical precipitation followed by hydrothermal aging and yields hydroxyapatite nanoparticles of tunable sizes, crystallinity, and, possibly, composition. Compared to conventional hydrothermal HA particle synthesis methods whereby particles are made directly in hydrothermal reactions [1, 20], the division of the process into two steps ensures size uniformity by separating the nucleation and growth processes of the HA particles. The precipitation step nucleates HA seed crystals, while the hydrothermal aging step controls the growth of the seed crystals into larger particles [28]. To generate HA nanoparticles of systematically varying crystallinity and size, we varied the hydrothermal aging times (A1, A2, A3) and utilized different precursor salts (B1), while maintaining temperature and pH. Extensive characterization via TEM, SEM, FTIR, and pXRD defined the specific nanoscale properties of the resulting particles (Table 4.1). In particular, the importance of the choice of precursor salts is evident in comparing A3 particles and B1 particles, which exhibited similar length, but varied in crystallinity. The resulting particles ranged from having biologically relevant lengths and crystallinities (A1) [2, 3] to longer dimensions and higher crystallinities (A2, A3, B1), enabling us to systematically evaluate the effects of nanoparticle size on tumor cell behavior. Incorporation of these well-defined particles into PLG scaffolds resulted in the presentation of the particles at the porous surface of the scaffolds, enabling interactions with seeded cells (Fig. 5). Such scaffold systems will be critical for the identification of parameters for the design of non-tumorigenic mineral-containing and mineralized matrices for bone regeneration.

It has been shown that HA and other calcium phosphate surfaces efficiently adsorb adhesive and serum proteins (e.g. fibronectin) that are crucial in mediating cell attachment and tissue formation [5, 29-31]. Other studies with different material systems have demonstrated that nanoparticle size modulates protein adsorption [32], and our results further indicate that altering the nanoscale properties of HA affects overall protein adsorption behavior (Fig. 4.7). Specifically, our studies reveal that the overall magnitude of protein adsorption decreases monotonically with increasing HA crystal size. Additionally, decreasing the crystallinity of HA nanoparticles (assessed by the IR splitting factor) independent of overall size also increases the protein adsorption capacity of the scaffolds, as indicated by differences in serum protein adsorption between scaffolds fabricated from particle sets A3 and B1 (Fig. 4.7A). Overall available scaffold surface area may vary based on particle size and shape, and these changes may contribute to the observed differences in protein adsorption. Nevertheless, our results measured with scaffolds in which the amount of HA was normalized to surface area indicate that nanoparticle characteristics also modulate total adsorption capacity (Fig. 9A). These changes in protein adsorption may have important implications for general bone function as well as metastatic bone disease, as altered protein adsorption broadly modulates cell adhesion, proliferation, and survival of osteoclasts [33], osteoblasts [4, 29, 30], and breast cancer cells [5]. It is likely that adsorbed RGD-containing proteins, such as fibronectin, may be involved in these effects, as these biomolecules regulate cell attachment [34], focal adhesion formation [35], and proliferative signaling pathways [36].

Cell behavior is affected by mineral characteristics. For example, osteoblasts respond differently to HA as compared to tricalcium phosphate (TCP) [37], and amorphous calcium phosphate and highly crystalline HA exhibit varying levels of osteoconductivity [38]. Similarly,

HA and TCP elicit varying levels of differentiation in pre-osteoclasts [39] and resorptive activity in mature osteoclasts [40]. Additionally, the results of our study indicate that nanoscale mineral properties are crucial regulators of tumor cell behavior. In particular, scaffolds that contained smaller and less crystalline particles and adsorbed more adhesive proteins out of serum also supported more initial breast cancer cell adhesion and proliferation (Fig. 8A, B). While enhanced secondary tumor formation in the bone is generally attributed to resorptive release of growth factors and other soluble cues [8], our data support the idea that direct interactions with the mineral matrix could give rise to increased tumor formation and cancer cell growth in the bone microenvironment. Pathologically, our data suggest that exogenously introduced HA may regulate cellular adhesion and growth through adhesive protein adsorption, and thereby serve as a high affinity-substrate for metastasizing breast cancer cells. *In vivo*, TE bone has been observed to serve as a metastasis target [16], and recent evidence indicates that cancer cell-bone matrix interactions activate invasive and proliferative potential [7], further supporting the contention that HA may be involved in the breast cancer cell avidity for bone.

IL-8 secretion is linked closely to osteoclast-mediated osteolysis in metastatic breast cancer [10] and is known to be enhanced through cell-HA interactions [5]. Our current study suggests that the nanoscale properties of HA strongly affect overall IL-8 expression, with larger and more crystalline HA stimulating significant IL-8 upregulation in breast cancer cells (Fig. 4.10). This finding is somewhat surprising since IL-8 expression may be expected to correlate with protein adsorption, as integrin engagement affects IL-8 transcription in certain cancers [41]. However, upon adsorption onto surfaces, in particular crystals, protein conformation, and possibly the presentation of cellular binding sites, may change [31, 42]. Therefore, it is possible that though more protein is adsorbed to the smaller, less crystalline particles, these proteins no

longer have their native conformation and do not trigger IL-8 expression. It is also possible that the cell-mineral interactions affect IL-8 production by breast cancer cells through other mechanisms. For example, nanoparticles could become loosened from the scaffold during cell growth and induce an inflammatory reaction, as environmental particles are known to activate proinflammatory signaling [43]. Although not clear from the current study, our mineral-containing system could be further employed to investigate these possibilities.

While the insights provided by our system have pathological significance, future studies can take into account the broader complexity of breast cancer and the bone microenvironment. For example, in this study we have solely tested the cellular response of a highly metastatic breast cancer cell line, but it is possible that non-metastatic breast cancer cells may also be responsive to HA. In fact, HA may promote growth and invasiveness in non-metastatic breast cancer cell lines, and this response may be clinically significant, as microcalcifications in the breast are associated with malignancies and could potentially play a role in driving tumor progression [44]. Furthermore, this platform could be used to investigate interactions between breast cancer cells and osteoblasts and osteoclasts to fully recapture the cellular aspect of bone. Both of these cell types induce the osteolytic capability of breast cancer cells [5, 10, 45], and both may be affected by nanoscale HA characteristics [46, 47]. Mineral-containing tumor models incorporating hydrothermally-aged HA nanoparticles provide the capability to address these aspects of the bone microenvironment and thereby have the potential to improve our understanding of the molecular mechanisms underlying bone metastasis that may ultimately enable the discovery of novel therapeutic targets for patient care. Moreover, the use of sHA in culture models could broadly provide insight into basic bone biology and the potential risks of new classes of mineralized and mineral-containing matrices for bone regenerative technologies.

4.6 Conclusions

We have created a mineral-containing platform that recreates certain aspects of the 3-D bone microenvironment by incorporating well-defined sHA nanoparticles into a TE biomaterial scaffold. We have used this platform to investigate the effect of nanoscale HA characteristics on breast cancer cell behavior, and our study indicates that the nanoscale properties of HA play a key role in regulating breast cancer cell behavior. In conjunction with previous evidence that osteolytic lesions are sites of low-crystallinity and smaller mineral particles [2], this work suggests that altering the nanoscale properties of microenvironmental bone mineral could play a role in the formation of a metastatic niche in bone supporting enhanced tumor cell colonization and growth. Specifically, we have demonstrated that smaller, less crystalline HA particles increase cellular adhesion and growth, while larger and more crystalline HA enhances breast cancer cell expression of the osteolytic factor IL-8. Overall, our findings provide new evidence that the vicious cycle of bone metastasis is not only mediated by growth factors in the bone microenvironment, but also by the actual materials characteristics of the mineral matrix.

References

[1] Elliott JC. Structure and chemistry of the apatites and other calcium orthophosphates: Elsevier; 1994.

[2] Bi X, Patil C, Morrissey C, Roudier MP, Mahadevan-Jansen A, Nyman J. Characterization of bone quality in prostate cancer bone metastases using raman spectroscopy. Proceedings of SPIE 2010;7548:75484L.

[3] Boskey A. Bone mineral crystal size. Osteoporosis International 2003;14:S16-S20.

[4] Balasundaram G, Sato M, Webster TJ. Using hydroxyapatite nanoparticles and decreased crystallinity to promote osteoblast adhesion similar to functionalizing with RGD. Biomaterials 2006;27(14):2798-805.

[5] Pathi SP, Kowalczewski C, Tadipatri R, Fischbach C. A novel 3-d mineralized tumor model to study breast cancer bone metastasis. PLoS One 2010;5(1):e8849.

[6] Kim SS, Sun Park M, Jeon O, Yong Choi C, Kim BS. Poly(lactide-co-glycolide)/hydroxyapatite composite scaffolds for bone tissue engineering. Biomaterials 2006;27(8):1399-409.

[7] Reichert JC, Quent VM, Burke LJ, Stansfield SH, Clements JA, Hutmacher DW. Mineralized human primary osteoblast matrices as a model system to analyse interactions of prostate cancer cells with the bone microenvironment. Biomaterials 2010;31(31):7928-36.

[8] Mundy GR. Metastasis to bone: Causes, consequences and therapeutic opportunities. Nat Rev Cancer 2002;2(8):584-93.

[9] Kingsley LA, Fournier PG, Chirgwin JM, Guise TA. Molecular biology of bone metastasis. Mol Cancer Ther 2007;6(10):2609-17.

[10] Bendre MS, Montague DC, Peery T, Akel NS, Gaddy D, Suva LJ. Interleukin-8 stimulation of osteoclastogenesis and bone resorption is a mechanism for the increased osteolysis of metastatic bone disease. Bone 2003;33(1):28-37.

[11] Fischbach C, Chen R, Matsumoto T, Schmelzle T, Brugge JS, Polverini PJ, et al. Engineering tumors with 3D scaffolds. Nat Methods 2007;4(10):855-60.

[12] Ginestier C, Liu S, Diebel ME, Korkaya H, Luo M, Brown M, et al. CXCR1 blockade selectively targets human breast cancer stem cells in vitro and in xenografts. J Clin Invest 2010;120(2):485-97.

[13] Freund A, Chauveau C, Brouillet JP, Lucas A, Lacroix M, Licznar A, et al. IL-8 expression and its possible relationship with estrogen-receptor-negative status of breast cancer cells. Oncogene 2003;22(2):256-65.

[14] Kang Y, Siegel PM, Shu W, Drobnjak M, Kakonen SM, Cordon-Cardo C, et al. A multigenic program mediating breast cancer metastasis to bone. Cancer Cell 2003;3(6):537-49.

[15] Verbridge SS, Chandler EM, Fischbach C. Tissue-engineered three-dimensional tumor models to study tumor angiogenesis. Tissue Eng Part A 2010;16(7):2147-52.

[16] Moreau JE, Anderson K, Mauney JR, Nguyen T, Kaplan DL, Rosenblatt M. Tissue-engineered bone serves as a target for metastasis of human breast cancer in a mouse model. Cancer Res 2007;67(21):10304-8.

[17] Kothapalli CR, Shaw MT, Wei M. Biodegradable HA-PLA 3-D porous scaffolds: Effect of nano-sized filler content on scaffold properties. Acta Biomater 2005;1(6):653-62.

[18] Weiner S, Bar-Yosef O. States of preservation of bones from prehistoric sites in the near-east - a survey. Journal of Archaeological Science 1990;17(2):187-96.

[19] Schmittgen TD, Livak KJ. Analyzing real-time PCR data by the comparative C(t) method. Nat Protoc 2008;3(6):1101-8.

[20] Dorozhkin SV. Nanosized and nanocrystalline calcium orthophosphates. Acta Biomaterialia 2010;6(3):715-34.

[21] el Feki H, Rey C, Vignoles M. Carbonate ions in apatites: Infrared investigations in the upsilon 4 CO3 domain. Calcif Tissue Int 1991;49(4):269-74.

[22] Ruoslahti E. Fibronectin. J Oral Pathol 1981;10(1):3-13.

[23] Pampaloni F, Reynaud EG, Stelzer EH. The third dimension bridges the gap between cell culture and live tissue. Nat Rev Mol Cell Biol 2007;8(10):839-45.

[24] Conz MB, Granjeiro JM, Soares GdA. Physicochemical characterization of six commercial hydroxyapatites for medical-dental applicatons as bone graft. Journal of Applied Oral Science 2005;13:136-40.

[25] Cai YR, Tang RK. Calcium phosphate nanoparticles in biomineralization and biomaterials. Journal of Materials Chemistry 2008;18(32):3775-87.

[26] Cunniffe GM, O'Brien FJ, Partap S, Levingstone TJ, Stanton KT, Dickson GR. The synthesis and characterization of nanophase hydroxyapatite using a novel dispersant-aided precipitation method. Journal of Biomedical Materials Research Part A 2010;95A(4):1142-9.

[27] Martins MA, Santos C, Almeida MM, Costa MEV. Hydroxyapatite micro- and nanoparticles: Nucleation and growth mechanisms in the presence of citrate species. Journal of Colloid and Interface Science 2008;318(2):210-6.

[28] Murray CB, Kagan CR, Bawendi MG. Synthesis and characterization of monodisperse nanocrystals and close-packed nanocrystal assemblies. Annual Review of Materials Science 2000;30:545-610.

[29] Sawyer AA, Hennessy KM, Bellis SL. The effect of adsorbed serum proteins, RGD and proteoglycan-binding peptides on the adhesion of mesenchymal stem cells to hydroxyapatite. Biomaterials 2007;28(3):383-92.

[30] Woo KM, Seo J, Zhang R, Ma PX. Suppression of apoptosis by enhanced protein adsorption on polymer/hydroxyapatite composite scaffolds. Biomaterials 2007;28(16):2622-30.

[31] Gilbert M, Shaw WJ, Long JR, Nelson K, Drobny GP, Giachelli CM, et al. Chimeric peptides of statherin and osteopontin that bind hydroxyapatite and mediate cell adhesion. J Biol Chem 2000;275(21):16213-8.

[32] Lundqvist M, Stigler J, Elia G, Lynch I, Cedervall T, Dawson KA. Nanoparticle size and surface properties determine the protein corona with possible implications for biological impacts. Proc Natl Acad Sci U S A 2008;105(38):14265-70.

[33] Redey SA, Razzouk S, Rey C, Bernache-Assollant D, Leroy G, Nardin M, et al. Osteoclast adhesion and activity on synthetic hydroxyapatite, carbonated hydroxyapatite, and natural calcium carbonate: Relationship to surface energies. J Biomed Mater Res 1999;45(2):140-7.

[34] Yang Y, Cavin R, Ong JL. Protein adsorption on titanium surfaces and their effect on osteoblast attachment. J Biomed Mater Res A 2003;67(1):344-9.

[35] Cukierman E, Pankov R, Yamada KM. Cell interactions with three-dimensional matrices. Curr Opin Cell Biol 2002;14(5):633-9.

[36] Garcia AJ, Vega MD, Boettiger D. Modulation of cell proliferation and differentiation through substrate-dependent changes in fibronectin conformation. Mol Biol Cell 1999;10(3):785-98.

[37] Sun JS, Tsuang YH, Liao CJ, Liu HC, Hang YS, Lin FH. The effects of calcium phosphate particles on the growth of osteoblasts. J Biomed Mater Res 1997;37(3):324-34.

[38] Nagano M, Nakamura T, Kokubo T, Tanahashi M, Ogawa M. Differences of bone bonding ability and degradation behaviour in vivo between amorphous calcium phosphate and highly crystalline hydroxyapatite coating. Biomaterials 1996;17(18):1771-7.

[39] Lange T, Schilling AF, Peters F, Haag F, Morlock MM, Rueger JM, et al. Proinflammatory and osteoclastogenic effects of beta-tricalciumphosphate and hydroxyapatite particles on human mononuclear cells in vitro. Biomaterials 2009;30(29):5312-8.

[40] Detsch R, Mayr H, Ziegler G. Formation of osteoclast-like cells on HA and TCP ceramics. Acta Biomaterialia 2008;4(1):139-48.

[41] Fischbach C, Kong HJ, Hsiong SX, Evangelista MB, Yuen W, Mooney DJ. Cancer cell angiogenic capability is regulated by 3D culture and integrin engagement. Proc Natl Acad Sci U S A 2009;106(2):399-404.

[42] Addadi L, Rubin N, Scheffer L, Ziblat R. Two and three-dimensional pattern recognition of organized surfaces by specific antibodies. Acc Chem Res 2008;41(2):254-64.

[43] Park EJ, Park K. Oxidative stress and pro-inflammatory responses induced by silica nanoparticles in vivo and in vitro. Toxicol Lett 2009;184(1):18-25.

[44] Morgan MP, Cooke MM, Christopherson PA, Westfall PR, McCarthy GM. Calcium hydroxyapatite promotes mitogenesis and matrix metalloproteinase expression in human breast cancer cell lines. Mol Carcinog 2001;32(3):111-7.

[45] Thomas RJ, Guise TA, Yin JJ, Elliott J, Horwood NJ, Martin TJ, et al. Breast cancer cells interact with osteoblasts to support osteoclast formation. Endocrinology 1999;140(10):4451-8.

[46] Boyan BD, Lossdorfer S, Wang L, Zhao G, Lohmann CH, Cochran DL, et al. Osteoblasts generate an osteogenic microenvironment when grown on surfaces with rough microtopographies. Eur Cell Mater 2003;6:22-7.

[47] Geblinger D, Addadi L, Geiger B. Nano-topography sensing by osteoclasts. J Cell Sci 2010;123(Pt 9):1503-10.

CHAPTER 5
DEVELOPMENT OF A 3-D CULTURE SYSTEM FOR DIFFUSION-CONTROLLED GRADIENT FORMATION

Contributors: Omotunde Babalola, Jason Dorvee, Antoine Bordereau, Kevin Eckes, Adele Boskey, Lawrence Bonassar, Lara Estroff.

5.1 Abstract

Many biological tissues are formed and maintained in spatially and temporally graded environments that help regulate cellular function. Understanding how cells are affected by and how they control spatial and temporal chemical and physical gradients can lead to potential solutions for tissue growth and repair. This work shows a procedure for introducing cells into a simple 3-D culture system that allows for 1-D diffusion through the culture. The system was constructed from a gas-permeable tube, filled with 2 wt% agarose, connected to two reservoirs containing sodium bicarbonate ($NaHCO_3$) or HEPES buffered media. Bovine articular chondrocytes were selected as the cell type to examine for this study as they are under directional gradients of oxygen, nutrients, and pH in native cartilage due to the avascular nature of the tissue as well as the presence of a gradient of mineral at the osteochondral interface between cartilage and bone. Cellular viability was examined through 5, 9, and 12 days in the carbonate buffered system, and through 6 days for the HEPES system. $NaHCO_3$-buffered systems were able to sustain a viability of greater than 90% through 12 days. The viability of cells in HEPES buffered systems was much lower (below 16% through 6 days). The matrix production in $NaHCO_3$-buffered STRS was examined at 5 days via histological staining with safrinin-O. To examine mineral formation in the gels in the presence of chondrocytes, $CaCl_2$ and Na_2HPO_4 were introduced into opposing reservoirs. Bands of calcium phosphate mineral were unable to form in the gels for $NaHCO_3$-buffered systems due to the precipitation of calcium carbonate in the

calcium reservoirs. HEPES buffered systems were able to form mineralized bands of calcium phosphate at 50 mM $CaCl_2$ and Na_2HPO_4. Cell culture systems such as the one developed here that allow for dynamic development of 3-D physical and chemical gradients can provide controlled means to study the development and activity of cells under temporal and spatial gradients.

5.2 Introduction

This chapter describes the development of a dynamic 3-D cell culture system that allows for gradients of ions, gases, and other molecules to diffuse through the system in the presence of cells. Functionally graded systems are inherent in complex systems found in nature and regulate multiple cellular processes for tissue development, healing, and cancer metastasis in tissues [1]. The generation and maintenance of molecular, mechanical, and temporal gradients is a dynamic process that can involve multiple cell types, length scales, and signaling molecules. To improve understanding of graded systems, development of a dynamic system that allows for the presence of physical and chemical gradients can provide a controlled means to design materials as well as to provide platforms we could use to study the development and activity of different cell types under temporal and spatial gradients.

Developing cell culture systems allowing for the presence of spatial and temporal gradients is challenging. Ideally, the culture will be able to support cell proliferation and differentiation, as well as retain the extracellular matrix produced by the cells [2], while maintaining chemical and/or physical gradients. Hydrogels are good platforms for cell culture as they can structurally mimic the extracellular matrix of tissues, provide a scaffold for cells, and act as a medium for creating gradients [3-5]. Several systems have been developed to form gels

with gradients in mechanical properties by changing gel porosity [6], gel stiffness [7], or glass or ceramic content [8-10]. Chemical gradients have also been developed through covalently binding biomacromolecules to the gel [11], diffusing proteins from embedded beads [12], or culturing cells in wells spatially located on a gel [9]. These techniques have provided insights into how cells respond to physical and chemical gradients. However, tailoring gels for mechanical or chemical gradients spatially excludes the possibility of examining *temporal* changes, while diffusive techniques often allow for radial dispersion of the molecule of interest with little directional control.

Several hydrogel systems have been developed to examine crystal growth processes that occur in nature under the presence of ion gradients [13, 14]. Although crystal growth in gels is often done in the context of growing larger crystals via diffusion [15], the interest in the formation of mineralized tissues has stimulated advances in developing hydrogel diffusion systems to examine crystal growth processes in gels in the presence of non-collagenous proteins, which are associated with the mineralization process of bone and teeth [13, 16-19]. In particular, Boskey developed a system that utilizes gels with long (6 cm) path lengths in order to obtain *dynamic* diffusion gradients of ions. The creation of dynamic temporal and spatial gradients through a hydrogel suggests the possibility of adapting such a system for cell culture systems.

Introducing cells into a similar system allows for the study of cell activity in the presence of 1-D dynamic gradients and how changes in gradients can affect cellular function. Herein, a double diffusion system, called the Single Tube Reservoir System (STRS), was developed to support cell proliferation and viability by encapsulating cells into gas-permeable tubes filled with agarose gel and connecting the ends of the tube to two reservoirs. Initial tests have also been conducted to examine the effect of diffusing calcium (Ca) and phosphate (P) ions through

opposing reservoirs in this system. Such a system provides a means to apply different gradients of ions, nutrients, or gases to various cell types via diffusion and allows for examination of how cells respond to the presence of such gradients.

Bovine articular chondrocytes were selected as the cell source for evaluating the efficacy of the STRS. The osteochondral interface is an excellent example of a graded interface in biology. The avascular nature of cartilage and the presence of the mineral barrier between cartilage and bone [20, 21] make this system an ideal starting point to evaluate the diffusion system as a platform for studying cell-mediated biomineralization. Due to the lack of blood vessels and the mineral barrier, delivery of nutrients and oxygen to articular chondrocytes *in situ* is dependent upon diffusion of the molecules from the synovial fluid of the joints to the cartilage. Glucose and oxygen concentrations have been reported to decrease from the articular surface to the osteochondral interface [22, 23]. The directionality of this diffusion transport results in gradients of glucose, pH, and oxygen, from the proximal to distal end of cartilage tissues, which in turn subjects chondrocytes embedded within the cartilage matrix to the gradients as well. As a result, chondrocytes in the deep zone of cartilage experience a more hypoxic environment than cells located in the middle and superficial zones [20, 21]. In addition to the distance between the subchondral bone and the superficial zone and synovial fluid interface, chondrocytes located closest to the synovial fluid interface at the superficial zone have more access to nutrients than chondrocytes located in the deep zone of cartilage (closer to the bone).

The role of the mineralized region of articular cartilage is not limited to acting as a barrier for nutrients from bone. The region also provides a transition of mechanical properties from stiff bone to compliant cartilage via a gradient of mineral spanning approximately 100 μm [24]. Damage to cartilage is hard to repair due to this sharp transition in modulus, which necessitates

the development of biomaterials that are composed of compliant and stiff biomaterials matching the properties of both cartilage and bone [25]. From a tissue engineering standpoint, understanding the formation and regulation of the mineral interface would advance biomaterial development for cartilage repair. The role of articular chondrocytes on mineralization is unclear, however calcification of articular cartilage occurs predominately at the osteochondral interface [26] and studies have indicated that changes in the cartilage matrix such as collagen denaturation [27] and proteoglycan degradation [28] observed in osteoarthritis can lead to mineralization of cartilage. The presence of these gradients in cartilage as well as the complexity of the osteochondral interface make articular chondrocytes an ideal cell type for evaluating the STRS for cell culture under 1-D diffusion gradients for mineralization.

5.3 Materials & Methods

5.3.1 Single Tube Reservoir System (STRS) Design

The STRS is composed of a gel-filled tube connecting two reservoirs. To construct the reservoirs, pairs of 250 mL media bottles (Kimax® Kimball 250 mL Media Bottle, No. 14395) had hose fittings extruded from the bottle (Cornell University, Glass Shop) at the 50 mL mark on the bottle. Reservoirs were autoclaved at 125 ºC for 45 min before use (Tuttnauer 2540M). The STRS was assembled by attaching 2 cm of a 4 cm length of tubing (Nalgene, 8/12) onto the hose fittings on the reservoir to serve as a connecting tube between reservoirs to tubes to house gels (Fig. 5.1).

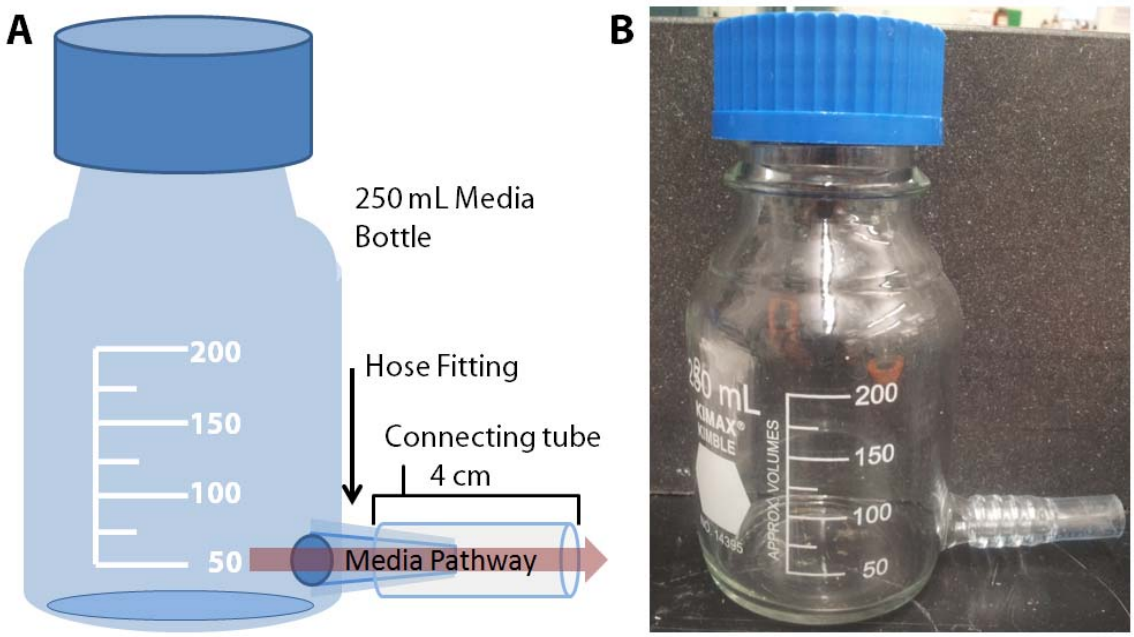

Figure 5.1: Schematic for reservoirs of the STRS constructed from 250 mL media bottles by extruding hose fittings at the 50 mL mark on the bottle (A). Photo of reservoir is shown with connecting tube attached (B).

Tubes connecting the reservoirs were constructed from polystyrene (PS-STRS) or silicone tubing (S-STRS) (Fig. 5.2). Polystyrene tubes were made by cutting 10 mL plastic pipettes (VWR) to 6 cm lengths (Fig. 5.2A). Silicone tubes (3/5 outer diameter, Biopharm®) were cut into 8 cm lengths. Glass inset tubes of 2 cm were cut from 10 mL glass pipettes (VWR) with a WELL 4020 Diamond Wire Saw. Silicone tubes and glass insets were plasma cleaned (Plasma Cleaner PDC-32G, Harrick Plasma) for 2 min before assembling glass insets 1 cm into the silicone tube (Fig. 5.2B). The plasma cleaning step helped to bond the silicone to the glass by exposing silanol groups.

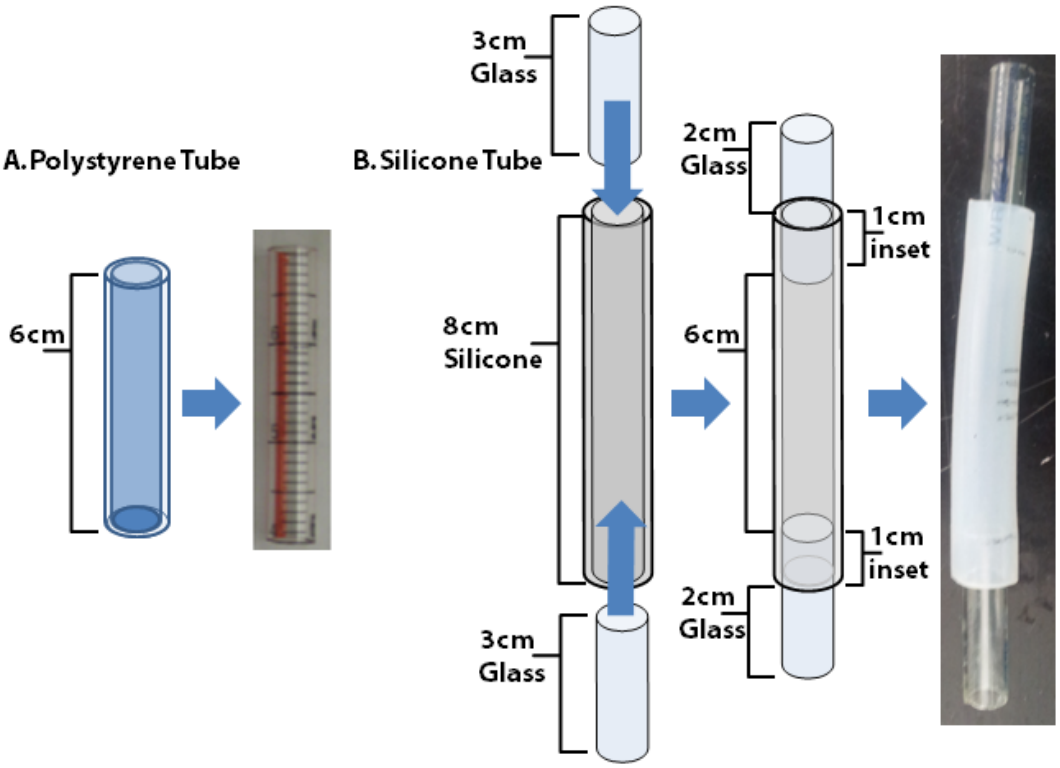

Figure 5.2: Schematics of PS-STRS tubes (A) and S-STRS tubes (B) are shown on the left and photos on the right. Polystyrene tubes were constructed by cutting 10 mL plastic pipettes into 6 cm lengths (A). Silicone tubes were assembled by connecting glass insets into 1 cm of the 8 cm length silicone tube to leave 6 cm of the tube length to house gel for STRS.

To improve agarose gel adhesion to the tubes, the interior of the S tubes were coated with 0.5% w/v% polyethylene-imine (PEI) in deionized water (DI-H_2O). A short section of the tube interior was kept PEI free for culturing cells. Tubes were sealed with parafilm (Parafilm® M, Pechiney Plastic Packaging) on one end, set up-right, and filled to the beginning of the cell section of the tube and set for 24 hrs. After 24 hrs, PEI was removed from the tubes and dried for 30 min (Precision® Gravity Correction Oven) while maintaining the upright position to avoid PEI coming in contact with the cell-holding section of the tube. Tubes were flipped and plugged on the other end and coated with PEI up to the cell containing section of the tube for 24 hrs, then dried as described before. This procedure resulted in PEI-free windows where the cell-seeded

gel layer would be placed. Fully PEI coated and uncoated S tubes were also prepared for comparison. Tubes were sterilized by brief immersion in 70% ethanol and dried in sterile conditions before use.

5.3.2 Preparation of Media for STRS

Dulbecco's Modified Eagle Media (DMEM, Gibco®) supplemented with 10% FBS (fetal bovine serum, PAA Laboratories), and 1% AM/AB (antibiotics/antimycotics, Cellgro) henceforth referred to as culture DMEM (cDMEM), was used for initial evaluation of the STRS. For mineralization experiments, custom powdered media (Formula No. 08-5083EB, Gibco™ Invitrogen Corporation) was ordered in 1L forming packets from Gibco modified from powder DMEM formulation 12100 where calcium, phosphate, and buffering compounds removed (Table 5.1).

Table 5.1: Custom powdered media Formula No. 08-5083EB for mineralization experiments modified form formulation 12100 DMEM (Gibco™).

	12100 DMEM	08-5083EB Media
D-glucose	O	O
L-glutamine	O	O
Calcium chloride anhydrous	O	X
Phenol red	O	X
Sodium bicarbonate	O	X
Sodium phosphate monobasic	O	X
Sodium pyruvate	O	X

O- included
X- removed

Two buffer systems were examined: 44 mM sodium bicarbonate ($NaHCO_3$) and 20 mM *N*-2-hydroxyethyl piperazine-*N*′-2-ethanesulfonic acid (HEPES) buffer. Sodium bicarbonate buffered media was made by adding 3.7 g of $NaHCO_3$ to each 1 L packet of powdered custom media, 10% FBS, and 1% AM/AB ($NaHCO_3$-custom media). The total volume of the media was brought to 1 L or 500 mL for twice concentrated (2X) media with DI-H_2O. The HEPES buffered media was prepared by adding HEPES buffer (Sigma) in place of the $NaHCO_3$ for final concentration of 20 mM or 40 mM for 2X concentrated media (HEPES-custom media). All media was pH balanced to 7.4 with 0.1 M NaOH or 0.1 M HCl. Ca and P-containing media were also made for mineralization experiments. $NaHCO_3$-custom media with 20 mM $CaCl_2$ or 20 mM Na_2HPO_4 were also made along with 50 mM $CaCl_2$ or 50 mM Na_2HPO_4 in HEPES-custom media. The concentration of Ca and P in the $NaHCO_3$-buffered media was limited to 20 mM as visible precipitation of calcium carbonate ($CaCO_3$) was observed at higher concentrations in the media and gel. Tris(hydroxymethyl)aminomethane (Tris) buffer containing 100 mM $CaCl_2$ or 100 mM Na_2HPO_4 were also made for establishing baseline mineralization. Media concentrated 2X was used in preparing gels for the STRS.

5.3.3 Bovine Articular Chondrocyte Harvesting from Bovine Joints

Full thickness cartilage from the condyles and the patellofemoral grove was cut from 1-3 day old bovine knee joints (Gold Medal Packing; Oriskany, NY). Cartilage tissue was rinsed thoroughly with PBS after harvesting and incubated at 37 ºC under constant rotation in cDMEM for 2 days. Cartilage tissue was diced into 2-4 mm cubes, washed with phosphate buffered saline (PBS) twice, and then placed into DMEM containing 0.3 wt% Type II collagenase (Worthington Biochemical Corporation) to digest for 18 hrs under constant rotation. Chondrocytes were

isolated through cell strainers (Falcon BD Cell strainers, 100 μm nylon) and washed with DMEM twice via centrifuge (Jounan 3Qi) for 5 mins at 1300 rpm. Cell viability and quantity were determined through counting live and dead cells on a hemocytometer after staining with 10 % Trypan Blue in PBS (Trypan Blue Solution 0.4% (w/v) in PBS, Mediatech, Inc., Cellgro). Only cell batches with viability above 93% were used for this study. Cells were mixed into 2X concentrated media, selected by experiment, at a density of 50e6 cells/mL and set in incubator until ready for loading into gel.

5.3.4 Agarose and Chondrocyte Loading into Tubes

Agarose gel (Cell culture grade, BP-165-25, Fischer Scientific) and agarose gel loaded with chondrocytes were loaded into the tubes in a layer-by-layer process (Fig. 5.3). Agarose was prepared at 4 wt% in DI-H_2O, autoclaved for 45 min at 125 °C, then pH adjusted to 7.4 with 0.1 M NaOH before autoclaving again to maintain sterility. Prepared agarose was placed into a 70 °C waterbath overnight to melt the gel. Agarose was removed from the waterbath and allowed cool for 2 min before loading into tubes. Polystyrene tubes were sealed at one end with parafilm before gel loading. The glass insets of the silicone tubes were plugged at one end with 3 cm custom-made plugs constructed from cutting 3 mL pipette tips sealed with parafilm . The 4 wt% agarose was mixed with 2X concentrated media to obtain 2 v/v% agarose in media. The 2 v/v% agarose was loaded as the first layer (layer I) via an 18-gauge syringe (PrecisionGlide®) into the tube and allowed to set for 15 min. Chondrocytes were gently mixed into 2 v/v% agarose in media at a concentration of 25e6 cells/mL and loaded into the tube in 0.4-2 cm lengths on top of Layer I to form Layer II and allowed to set for 15 min. The final layer (Layer III) of 2 v/v% agarose in media was loaded on top of Layer II and allowed to set for 15 min.

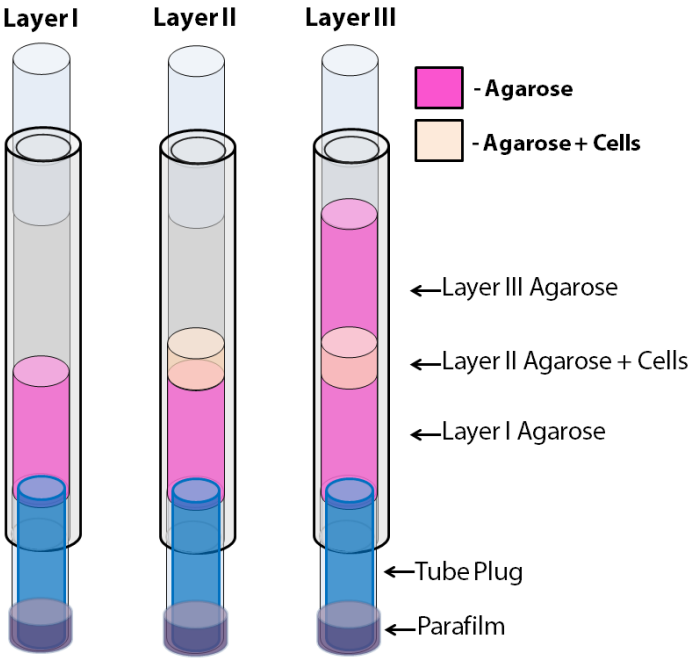

Figure 5.3: Schematic for the layer-by-layer process to load cell-seeded gels into the silicone tubes. Glass insets of tube are filled with a tube plug and held in place with parafilm. Layer I contains 2 v/v% agarose in media. After 15 min, Layer II containing 2 v/v% agarose in media with 25e6 cells/mL is loaded. After another 15 min, the last layer, Layer III of 2 v/v% agarose is loaded on top of Layer II and allowed to set for 15 min.

After 5 min, Layer III was topped off with more 2 v/v% agarose in media to minimize the presence of a meniscus. Gels were allowed to set for 1 hr before removal of the tube plug by breaking the parafilm seal with an 18-gauge needle and pulling the plug out of the glass insets. Agarose-filled PS tubes were then inserted into the STRS. Agarose-filled silicone tubes were inverted and a thin layer of gel was added to the plugged end of the gel and allowed to set for 30 min. Non-cell seeded agarose was also loaded into tubes for controls. Total length of gels for PS and S tubes was 6 ± 0.1 cm. Three STRSs were set up for each time point and condition.

5.3.5 STRS Cell Culture Control

For STRS controls, cell-seeded agarose gel plugs were made by loading non-PEI coated tubes with the cell-agarose-media mixture used for Layer II. The gel was allowed to set for 1 hr. After setting, cell-seeded gel was removed from the tube and sectioned into 0.4-2 ± 0.1 cm lengths. STRS controls were cultured along with cells in the STRS in triplicate.

5.3.6 Assembling the STRS

Gel-filled PS or S tubes were inserted into 1 cm of the Nalgene tubing attached to the hose fittings of two reservoirs to form PS- or S-STRS. Reservoirs were then filled with 200 mL of media. Air bubbles were removed from the system by gentle tilting of the reservoirs at the tubing connecting the gel-filled tubes to the reservoirs so that the media was in contact with the gel (Fig. 5.4).

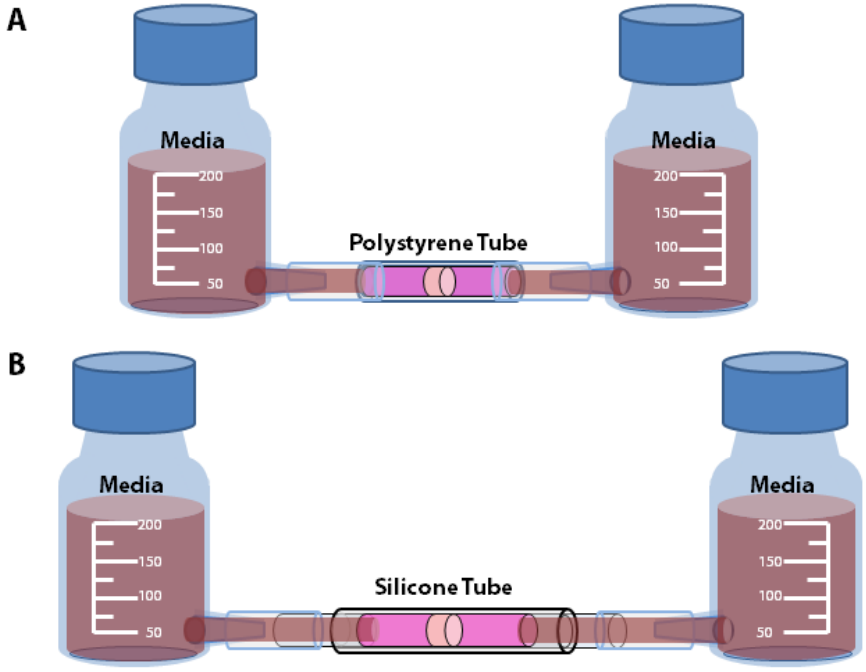

Figure 5.4: Assembly of STRS with polystyrene tube (A) and silicone tube (B). Tubes are inserted into hose fittings to connect two reservoirs. Reservoirs filled with 200 mL of media after assembly.

Systems were then placed into the incubator at 37 °C with 5% CO_2 atmosphere. For mineralization experiments, each STRS had Ca-containing media in one reservoir and P-containing media in the opposite reservoir.

5.3.7 Assessment of the STRS for Gel Adhesion to Tubes

The system was examined for leaks and ion diffusion through the agarose gel. Leaks were determined through a colormetric assay by connecting gel-filled tubes to two reservoirs, one filled with Allura Red AC dye, the other with Brilliant Blue FCF (McCormick) in DI-H_2O. The progression of the dye was tracked by time-lapse images (Sony 9DWX).

5.3.8 Determining the Effects of Replenishing Media in the STRS

To assess the need for replacing media for the STRS over extended culture periods, PS and silicone tube STRSs were cultured through ≥8 days. Reservoirs were filled with 200 mL $NaHCO_3$-custom media and was either replenished every 2 days or not replenished. Cell viability was determined through Alive/Dead staining.

5.3.9 Evaluating STRS Geometry on Chondrocyte Viability

The effect of culturing chondrocytes in a tube in or out of the STRS was examined by comparing the viability of chondrocytes seeded by 1) the layer-by layer process into PS tubes, 2) chondrocytes seeded by the layer-by-layer process into PS tubes, then removed from the tube, 3) a plug of agarose equivalent in size and shape to the cell-seeded sections of the layer-by-layer process, and 4) of chondrocytes loaded into PS tubes in the STRS (Fig. 5.5).

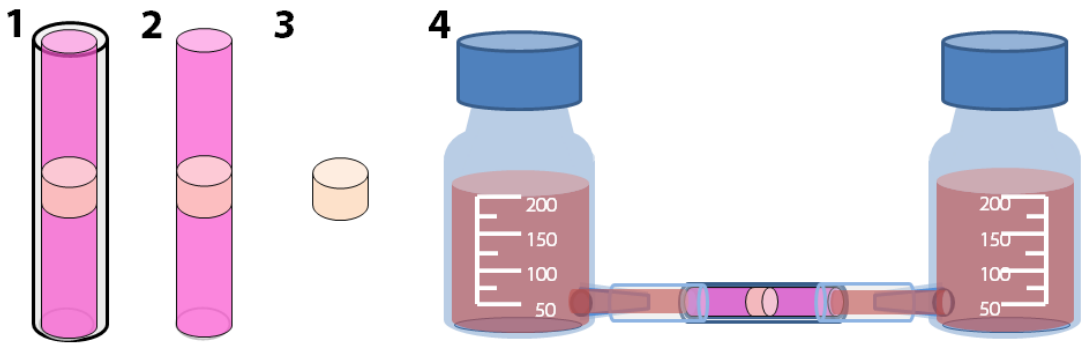

· Figure 5.5: Chondrocyte viability was examined under different culture geometries: 1) the layer-by layer process in PS tubes, 2) the layer-by-layer process outside of a tube, 3) a plug of agarose equivalent in size and shape to the cell-seeded sections of the layer-by-layer process, and 4) loaded into PS tubes in the STRS

Cells cultured in geometries 1, 2, and 3 were placed into 10 cm diameter sterile petri dishes (VWR) and covered in $NaHCO_3$-custom media. Media was replaced every 2 days. The reservoirs of the STRS were filled with 200 mL of $NaHCO_3$-custom media. Media in the STRS was not replenished. Cell viability was assessed at 1, 2, 4, and 6 days. Chondrocyte viability was compared to viability of cultures in silicone tube STRSs filled with $NaHCO_3$-custom media on days 1, 2, 4, 6, and 12 of culture.

5.3.10 Harvesting Cells for Assessment of Chondrocyte Response in STRS

Gels were removed at specific time points in triplicates from the STRS. For each STRS, the gel was sectioned to isolate the cell-seeded section of the gel. Then two 1 mm slices were removed from the cell-seeded section along the long axis of the gel through the center to obtain a cross section of the cell-seeded section. One of the 1 mm slices was used to assess chondrocyte viability and the other for matrix production. Slice I was taken for viability and divided into nine regions for examination (Fig. 5.6). Due to the symmetry of the STRS, regions 1, 4, and 7 were

seen as equivalents to region 3, 6, and 9 respectively and were only examined on one side after a preliminary examination showed little difference between the two areas. Slice II was examined at the edge, where non-cell-seeded gel and cell-seeded gel met and the center of the gel slice for differences in matrix production.

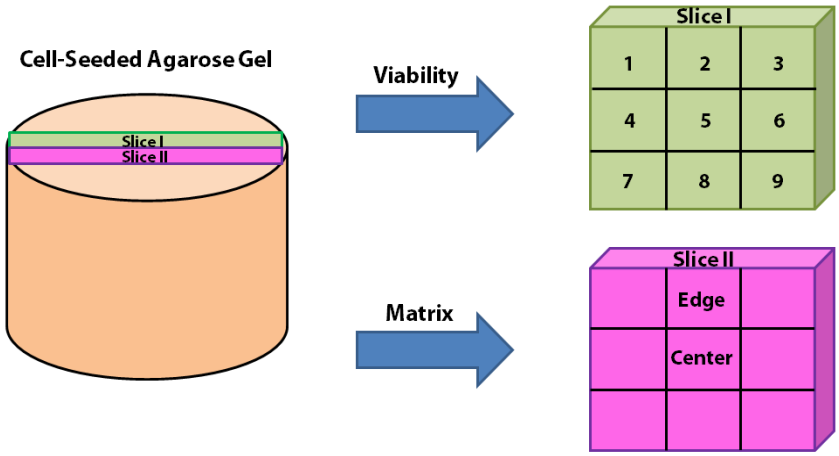

Figure 5.6: Schematic for sectioning the cell-seeded portion of the gel for viability and matrix assessment. Cell-seeded sections of the gel were harvested from the STRS system and sliced axially through the cylinder to remove two slices from the center. Viability was examined in 9 regions as shown in Slice I. Matrix production was evaluated for regions at the edge and center of the cell-seeded plug (Slice II).

Cell-seeded gel controls cultured in petri dishes were prepared as described in Section 5.3.5. Regions 5 and regions 1 or 3 were examined after initial studies showed differences only between the center of the cell-seeded gel and the edge, due to the gel exposure geometry to media. For quantification, each region had 3 images taken within the area of interest per sample. Each condition had an n = 3.

5.3.11 Determining Chondrocyte Viability and Cell Division

Viability of the chondrocytes was assessed from one of the 1 mm gel slices (Slice I) using Invitrogen's Live/Dead® cytotoxicity kit for mammalian cells. Stock solution of the dye was

made by adding 20 μL of 2 mM ethidium homodimer-1 and 2 μL of 4 mM calcien AM into 8 mL of phosphate buffered saline (PBS, Gibco). Gel slices were submersed for 1 hr at room temperature and then examined by a Nikon Eclipse TE2000-S with a Spot RT digital camera for capturing images and an epifluorescence attachment. To avoid photobleaching, samples were wrapped in aluminum foil and images taken in a dark room. Cell counting was done via image analysis software ImageJ. Viability was calculated from averaging the number of live cells over total cells in the field of view and displayed as a mean with +/- highest and lowest viability. Cell division was determined by the presence or absence of paired cells via brightfield microscope (Nikon Eclipse TE2000-S).

5.3.12 Assessing Matrix Production

Matrix production was assessed from a 1 mm slice (Slice II) harvested from the gel. The gel was immersed in 10% buffered formalin for at least 1 day before dehydration, embedded in paraffin and then sectioned into 10 μm thick layers via microtome and laid on glass slides. Sections were stained with safranin-O for glycosaminosglycans (GAGs) to assess matrix production and counter-stained with hematoxylin and eosin to visualize the cellular membrane and nucleus. Samples were examined via brightfield on an optical microscope (Nikon Eclipse TE2000-S) with image analysis done through ImageJ. Images were split by RGB color channels to determine fractional area stained positive for matrix production (blue channel). Amount of matrix production was determined by fractional area of the sample that had stained positive with safrinin-O over the field of view.

5.3.13 Addition of Ascorbic Acid in Media

A 50 µg/mL solution of L-ascorbic acid (Sigma) was sterile filtered and stored at 4 ºC. PS and silicone STRSs with $NaHCO_3$-custom media were supplemented with 200 µL every 3 days. Cells cultured in STRSs and PS tubes in petri dish were used as controls and not supplemented with ascorbic acid. Evidence of cell division was tracked through 9 days.

5.3.14 Assessment of Cell-seeded Layer Location

To examine if location within the gel affected chondrocyte viability, 0.4 cm cell-seeded gel sections were loaded after 2.8 cm layers of agarose gel or after 4 cm layers of agarose gel and filled with a third layer of agarose to obtain 6 cm length gels (Fig. 5.7). Reservoirs were filled with $NaHCO_3$-custom media.

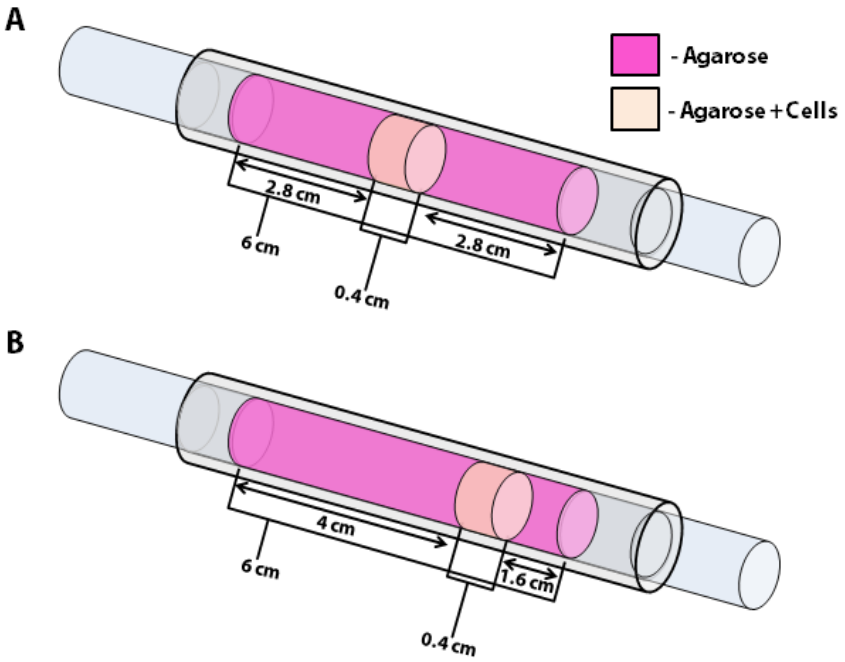

Figure 5.7: Schematic of gel loading demonstrating how the cell-seeded agarose section can be loaded at different locations along the tube by changing the initial amount of agarose loaded into the tubes before addition of the cell-seeded layer.

5.3.15 Assessment of Calcium and Phosphate Tolerance of Articular chondrocytes

Cell-seeded gel plug controls (Section 5.3.5) 4 mm in length were cultured in 6-well petri dishes (VWR) containing 5 mL of $NaHCO_3$-custom media . Media was supplemented with 0.25, 1.4, 8, 20 mM $CaCl_2$. Visible precipitation was observed for media containing 20 mM $CaCl_2$, therefore corresponding P concentrations were examined at concentrations below 20 mM in order to match reservoir concentrations for later studies. $NaHCO_3$-custom media was supplemented with 1.5, 3, 6, or 9 mM Na_2HPO_4 to examine P tolerance of cells. Media was replaced every 3 days. Cell viability was examined through 10 days.

5.3.16 Assessment of Calcium and Phosphate Diffusion through STRS

Reservoirs were filled with $NaHCO_3$-custom media with addition of 8 mM Ca, 20 or 50 mM of P on one side, and $NaHCO_3$-custom media without additional Ca or P in the opposing reservoir. Visible precipitation was observed for media containing 20 mM $CaCl_2$, limiting reservoir concentrations of calcium to 8 mM. NaCl was added to the reservoir without additional Ca or P to provide an equivalent osmolarity in the opposing reservoir. Ca and P diffusion through the gel was evaluated by examining Ca and P content of a 7 mm slice at the center of the 6 cm gel at various time points. Slices were placed into 10 mL of 5% nitric acid, heated for 1-2 days at 70°C (Precision® Gravity Correction Oven). The Ca and P content were determined from these hydrolyzed samples via inductively coupled plasma atomic emission spectrometry (ICP-AES).

5.3.17 Assessment of Mineralization in STRS

For mineralization experiments, 200 mL Tris buffer containing 100 mM $CaCl_2$ or 100 mM Na_2HPO_4 was placed in opposing reservoirs and band formation evaluated. Mineral formation was also examined in HEPES-custom media where 200 mL of media supplemented with 50 mM $CaCl_2$ or 50 mM Na_2HPO_4 was placed into opposing reservoirs. Gels were removed from silicone tubes on day 5 (Tris) and day 6 (HEPES) from the STRSs to examine the mineral. Full-length scans of the gel sliced along the axial direction were taken by a scanner (CanonScan 4200F) and mineral distribution analyzed with ImageJ. Mineral-containing regions of the gel were sectioned out and submerged in 0.15 M NH_4OH for 30 min with three changes of 0.15 M NH_4OH every 10 minutes. Samples were then freeze-dried (FreeZone$^{4.5}$) for two days and then examined by powder x-ray diffraction (Scintag Inc. PAD-X theta-theta X-ray Diffractometer, CuKa 1.54 Å, accelerating voltage 45 kV, current 40 mA, continuous scan, 2.0 deg/min).

5.3.18 Assessment of Mineralization in the Presence of Chondrocytes in the STRS.

After determination of the location of mineral formation in the S-STRS with HEPES-custom media, the cell-seeded agarose layer (Layer II) was seeded in the mineral location, at 1 cm away from the calcium reservoir at a length of 2 cm. Gels were removed from the silicone tubes 6 days after culture. Gels were treated for mineral analysis as in Section 5.3.14. Two 1 mm slices were removed from the cell-seeded gel portion and processed for viability analysis (Section 5.3.8) and matrix production (Section 5.3.9).

5.4 Results

5.4.1 Agarose Gel Adhesion in Polystyrene and Silicone Tubes

Polystyrene and silicone tubes coated and uncoated with PEI were examined for gel adhesion to the tubes to optimize diffusion conditions of ions from the reservoir through the gel rather than around the gel. The colormetric assay confirmed that the silicone tubes with PEI coating allowed for diffusion of the Allura Red and Brilliant Blue dyes through the gel rather than around the gel for the sodium bicarbonate system (Fig. 5.8). No streaks of dye were observed along the edge of the gel indicating that the gel was able to adhere to the tube walls to prevent reservoir solutions from moving between the gel and tube walls.

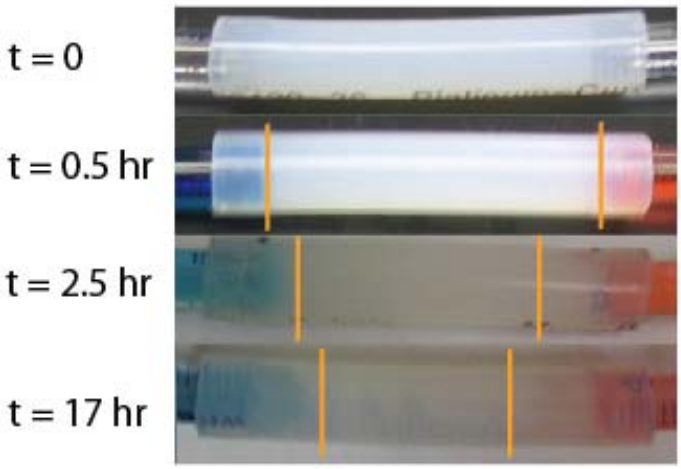

Figure 5.8: Colormetric assay of agarose gels loaded into 0.5% PEI-coated silicone tubes to track diffusion of Allura Red (right) and Brilliant blue (left). Lines on the tube show progression of dyes through the gel. The absence of dyes running along the side of the gel indicated dyes traveled through the gel and that agarose gels adhered well to the tubes.

For gels made with $NaHCO_3$–custom media, the PEI improved adhesion of the gel in the PS and silicone tubes. With the presence of mineral, gels had to be cut from the tubes. However, gels made with HEPES-custom media were similarly non-adherent to the silicone tubes with or without PEI.

5.4.2 Culture and Ion Restrictions of Buffered Media

$NaHCO_3$, HEPES, and Tris buffers were used in this work. Previous systems for HA formation in gels utilized Tris buffered systems for maintaining pH at 7.4 [13, 19]. Tris buffer is fat soluble and can permeate cellular membranes, leading to changes in internal chemistry and cytotoxic response in cells [29, 30]. Therefore $NaHCO_3$ and HEPES buffers, which are often used in cell culture, were used to maintain the pH in the STRS. In addition to the necessity of buffers to maintain a pH of 7.4, the cells need a source of nutrients that would not impact the calcium and phosphate content in the reservoirs for media studies. Towards this end, custom media without Ca and P was ordered through Gibco. A 2.1 mM +/- 0.3 mM baseline of calcium was present from the FBS (as determined by ICP-AES). The amount of Ca^{2+} that could be introduced to the $NaHCO_3$-buffered media was limited to 20 mM before visible precipitation of calcium carbonate $CaCO_3$ (confirmed through pXRD) was observed.

5.4.3 Culturing Chondrocytes in STRS with Sodium Bicarbonate Buffered Media

5.4.3.1 Experimental Design to Evaluate Chondrocyte Viability in the STRS

To utilize the STRS effectively, we sought to maintain cell viability above 80% over the course of the experiments. Towards this end, chondrocyte viability was compared in several set ups similar to the STRS and in the STRS. The importance of gas permeability of the STRS was investigated by examining the differences in viability when seeding chondrocytes in agarose gels inside gas-impermeable polystyrene tubes compared to gas-permeable silicone tubes. To further optimize the system, cell health and viability was determined in STRSs where media in the reservoir was replaced every 3 days or not replaced through the course of the experiment in the

presence and absence of ascorbic acid. These experiments were done in $NaHCO_3$-custom media as $NaHCO_3$ is most commonly used for cell culture.

5.4.3.2 Chondrocyte Response to PEI Coating on Silicone Tubes

The viability of chondrocyte cultures in the S-STRS with silicone tubes coated with PEI, coated with PEI with a PEI-free window for cell-seeded layer, and uncoated with PEI were examined in $NaHCO_3$ and HEPES—buffered custom media. Cultures were examined after 3 days. Optical microscope images showed a region of cell death from 100-250 μm into the gel for tubes coated in PEI (Fig. 5.9), while cells grown with the PEI-free window or without PEI had primarily live cells throughout the gel. As a result, S-tubes were coated with PEI with a PEI-free window when $NaHCO_3$-buffered media was used and not coated with PEI when HEPES-buffered media was used in the S-STRS systems.

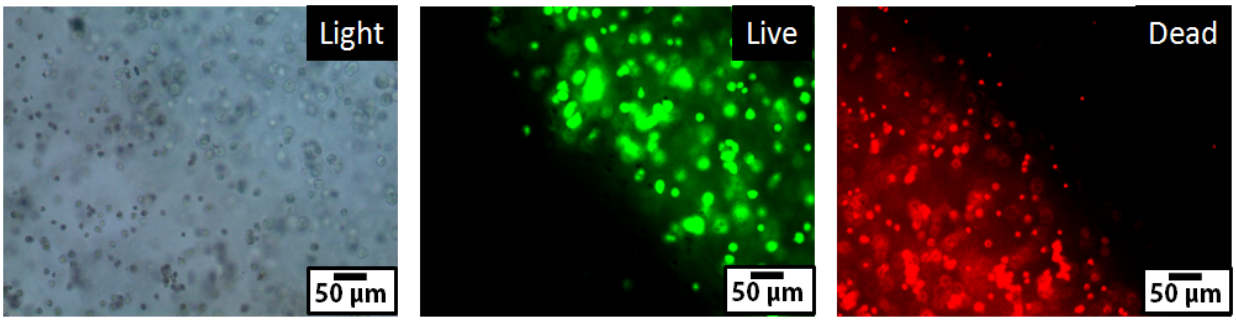

Figure 5.9: Optical light microscopy images of a chondrocyte-seeded section of agarose gel in contact with PEI coating of S-STRS in $NaHCO_3$-custom media (bottom left of images is closest to tube edge). Regions of cell death (red, ethidium homodimer stain) penetrating micrometers into the gel were observed for chondrocytes in contact with PEI. Beyond the region of cell-death, chondrocytes were mostly alive (green, calcien stain).

5.4.3.3 STRS Geometry Effects on Chondrocyte Viability

To examine how the STRS geometry could affect articular chondrocytes, cell viability was determined for chondrocytes seeded in agarose gel in 1) the layer-by layer process in PS

tubes, 2) the layer-by-layer process outside of a tube, 3) a plug of agarose equivalent in size and shape to the cell-seeded sections of the layer-by-layer process, and 4) the layer-by-layer process in PS tubes assembled into the STRS (Fig 5.10A). Culture geometries 1, 2, and 3 were cultured in petri dishes and immersed in $NaHCO_3$-custom media, with media replaced every 2 days.

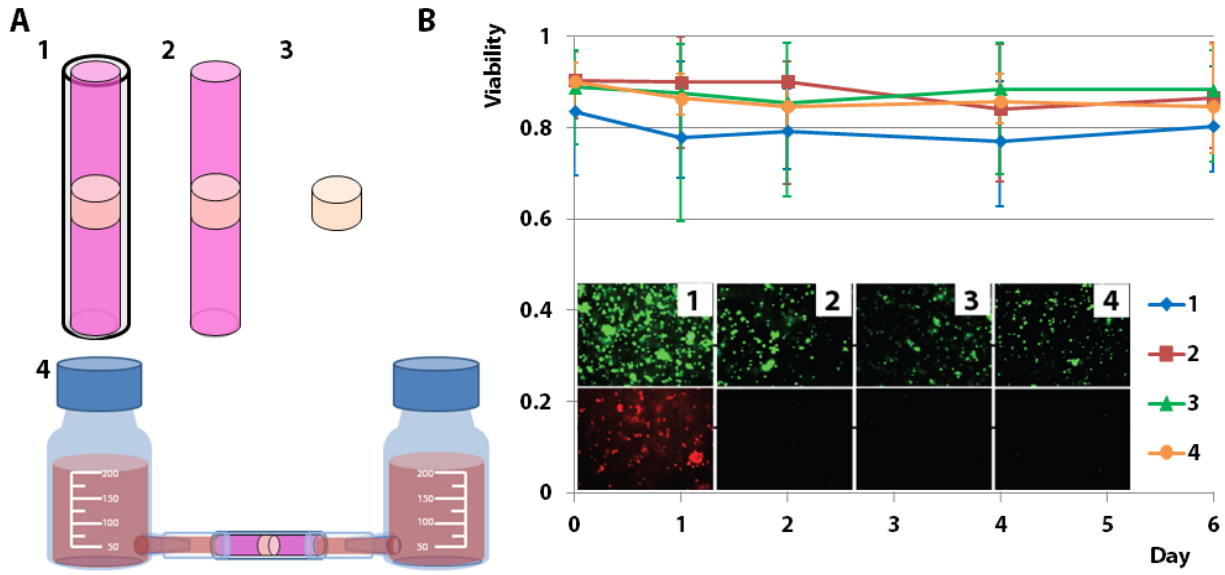

Figure 5.10: Schematic of the culture geometries examined for determining STRS ability to sustain chondrocyte viability in $NaHCO_3$-custom media. Chondrocytes were seeded into agarose gels in a 1) layer-by layer process in PS tubes, 2) layer-by-layer process outside of a tube, 3) plug of agarose equivalent in size and shape to the cell-seeded sections of the layer-by-layer process, and 4) layer-by-layer process in PS tubes assembled into the STRS (A). Plot of chondrocyte viability through 6 days of culture in geometries 1, 2, 3, and 4 (B). Inset in B shows fluorescent images of representative cells stained with calcein (live cells, green, top) and ethidium homodimer (dead cells, red, bottom) cells on day 6 of culture.

Live/dead fluorescence images of cultures harvested on day 6 showed the presence of more dead cells(red, Fig. 5.10, Inset 1) for culture geometry 1 and mostly live cells for culture geometries 2, 3, and 4 (green, Fig. 5.10B Inset 2, 3, 4). The average viability for geometries 2-4 was maintained above 80% through 6 days of culture. Chondrocytes cultured in geometry 1 had the lowest average viability at 77%. The average viability was highest for culture geometries 2 and 3 at 90% where cell access to media was not restricted by the presence of the PS tube. The

average viability of cells within the STRS did not fall below 85% and was comparable to geometry cultures 2 and 3 (Fig. 5.10B). The reservoirs of the STRS improved nutrient delivery from media to the cells within tubes and improved cell viability) 5% compared to cells cultured in PS-tubes in petri dishes.

Silicone tubes were also examined in the STRS due to their gas permeability. The PS tubes are gas impermeable and for carbonate systems which require the exchange of CO_2, PS tubes are not ideal for maintaining pH in such systems. Additionally, most cell types require O_2 to live. Chondrocytes cultured in silicone tubes in the STRS maintained viabilities averaging >93% through 9 and 12 day cultures (Fig. 11A). Fluorescent images of Live/Dead® stained samples showed the presence of very few dead (red) cells (Fig. 5.11B).

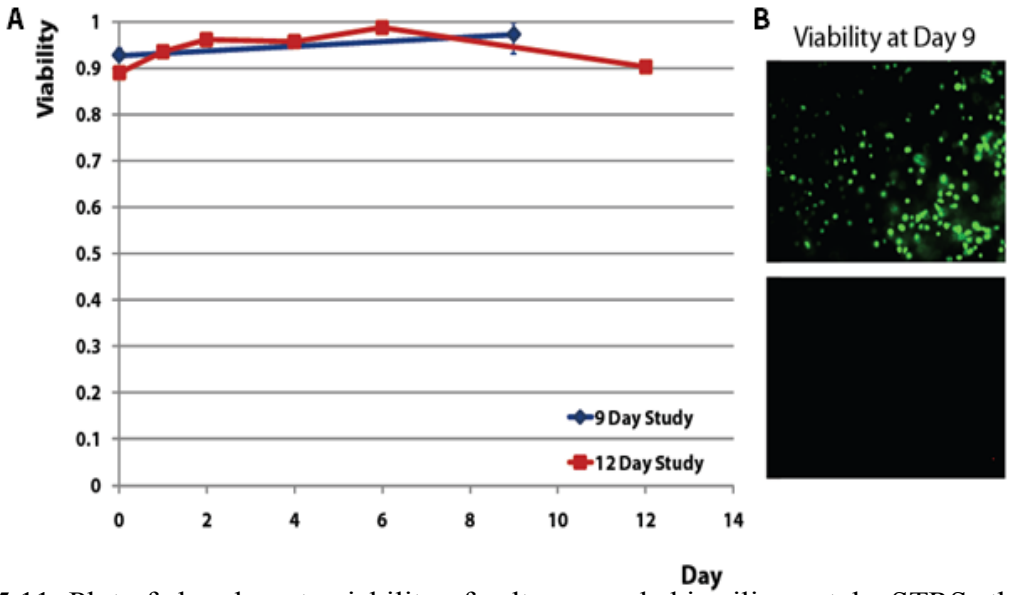

Figure 5.11: Plot of chondrocyte viability of cultures seeded in silicone tube STRSs through 9 and 12 days of culture in $NaHCO_3$-custom media (A). Representative live (green, top) and dead (red, bottom) images of cells on day 9 (B).

In addition to the gas-permeable silicone tubes improving the average viability of chondrocytes in the STRS compared to PS tubes, it was observed that the variability in viability was also significantly decreased.

5.4.3.4 Determining the Effects of Replenishing Media in the STRS

Media and its additives such as antibiotics, ascorbic acid, and fetal bovine serum have a limited lifetime. In typical chondrocyte cultures, media is replaced every 2-3 days through the duration of the culture to replenish nutrients and to remove by-products of waste. In the STRS, it is difficult to replace media and requires a large volume of media. Viability was determined for chondrocytes cultured in PS and S-STRSs through 8 and 9 days respectively with $NaHCO_3$-custom media maintained or replaced every 3 days (Fig. 5.12).

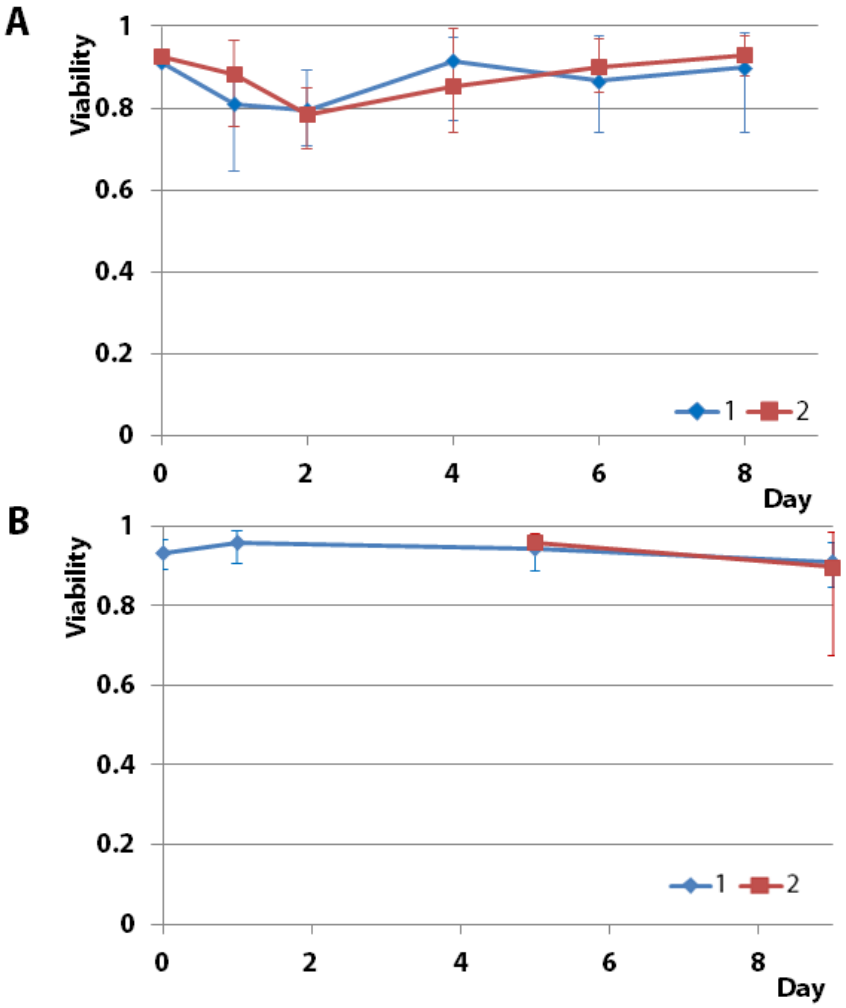

Figure 5.12: Viability of articular chondrocytes in the PS-STRS (A) and S-STRS (B) where $NaHCO_3$-custom media was not replaced through the duration of culture (solid diamonds) or replaced every 3 days (solid squares).

The viability of cells cultured in the STRS in PS tubes was similar through 8 days of culture (Fig. 5.12A). The lowest average viability of PS-STRSs without media replacement was 80%. The lowest average viability PS-STRSs with media replacement was 79%. For the S-STRSs, the lowest average viability for systems without media replacement was 91% and the lowest for systems with media replaced was 90% (Fig. 5.12B). In addition to having higher average viabilities, cells cultured in S-STRSs had a more narrow range of cell viability throughout the gel than cells cultured in PS-STRSs regardless of whether media was replaced or not. Replenishing nutrients for chondrocytes seeded into the silicone tubes had little effect to improve average viability through day 5. Systems cultured through day 9 have decreased viability in some regions of the gel, but average viability remained above 80%.

5.4.3.5 Addition of Ascorbic Acid in Culture

Ascorbic acid is a common supplement in media to support matrix production of chondrocytes *in vitro*. Ascorbic acid was added to the media of chondrocyte cultures in PS tubes in Petri dishes, PS-STRS, and S-STRS and fresh ascorbic acid added every 3 days of culture. Cell viability of cultures with ascorbic acid was compared to cultures without exposure to ascorbic acid. Cell division was determined to have occurred if paired cells were observed (Fig. 5.13). It was observed in optical microscope images that cultures in PS tubes in petri dishes showed no visible cell division through the culture period. Chondrocytes in PS-STRS had cell division occur at 5 days with the addition of ascorbic acid without media replacement. Without ascorbic acid, cells in the PS-STRS took 9 days for cell division if media was replaced every 3 days and had no cell division if no ascorbic acid was added and media was not replaced. For cultures in the S-STRS system, cell division was observed at 3 days with ascorbic acid and

media replacement and 5 days with ascorbic acid and media not replaced. The results are summarized in Table 5.2.

Figure 5.13: Representative brightfield image, taken on day 5 of culture, of articular chondrocytes cultured in S-STRS with $NaHCO_3$-custom media supplemented with ascorbic acid. Cell division was determined to have occurred if the presence of paired cells (circled by dotted line) were observed to be present.

Table 5.2: Start of cell division in chondrocyte cultures with and without ascorbic acid.

System	Tube Type	Media Replaced	Ascorbic Acid	Visible Cell Division [Day]
Petri dish	PS	Yes	No	None
Petri dish	PS	No	No	None
STR	PS	Yes	No	9
STR	PS	No	Yes	5
STR	PS	No	No	None
STR	Silicone	Yes	Yes	3
STR	Silicone	No	Yes	5

Subsequent experiments were done in the S-STRS with addition of ascorbic acid every 3 days and the media kept constant as chondrocytes were able to show visible proliferation by 5 days of culture.

It was observed through the course of these experiments that the cell-seeded section of PS tubes became increasingly acidic through culture time in $NaHCO_3$-custom media gels, seen by the phenol red indicator becoming a bright yellow, and confirmed by pH measurements showing the region around the cell-seeded section to be pH 4.5 after 5 days of culture. The gas impermeability of the PS tubes limited the exchange of CO_2 to maintain the pH of 7.4 for cultures utilizing carbonate buffers. Although HEPES buffered systems do not require the presence of CO_2 to maintain pH, subsequent studies utilized the silicone tubing, which was gas permeable to CO_2 and O_2 and therefore would be more suitable for introducing other cell types that require O_2.

5.4.3.6 Assessment of Cell-seeded Layer Location

The location of 4 mm cell-seeded agarose bands in the STRS were set at the center of the gel length, 2.8 cm from the reservoir and at 4 and 1.6 cm from the reservoirs to determine if changing the cell location would affect viability if reservoir contents were kept as the same $NaHCO_3$-custom media. There was no observable difference in viability of the cell plug between the two locations.

5.4.3.7 Assessing Matrix Production in STRS

In addition to maintaining the viability of cells above 80% through the duration of culture, it was also important to evaluate cellular activity such as matrix production in the STRS.

A 1 mm thick section of cell-seeded gel was harvested along the axial direction of the gel length and stained with safrinin-O for GAGs to indicate chondrocyte matrix production at 5 days and 9 days of culture with and without $NaHCO_3$-custom media supplemented with ascorbic acid replacement (Fig 5.14).

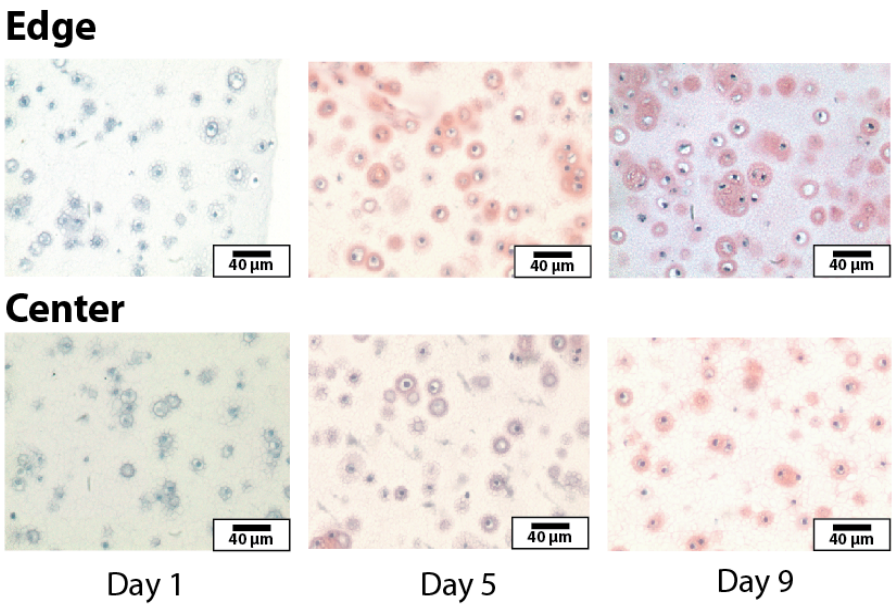

Figure 5.14: Optical microscope images, taken on days 1, 5, and 9 of culture, of S-STRS chondrocytes cultured with $NaHCO_3$-custom media supplemented with ascorbic acid. The images are taken at the edge and center of cell-seeded gels. Positive staining for GAGs by safranin-O is observed by days 5 and 9. Larger regions of the gel at the edge of cell-seeded sections stained positive for GAGS than gels at the center of the cell-seeded sections. Gel sections were counterstained with hematoxylin and eosin to visualize chondrocyte cellular membrane and nucleus.

Matrix production appeared to be higher on average at the edges of the cell plug compared to the center of the gel (Fig. 5.15; see Fig. 5.6 for definitions of edge and center). At day 5 of culture, the areas stained for GAGs were similar at the edge and center for S-STRS cultures with media replaced on the 3rd day, while cultures with the media kept constant had slightly less matrix production at the center compared to the edge of the cell-seeded section of

the gel. At day 9, the difference in matrix production becomes more obvious for systems in which the media was kept constant. In these samples, matrix production at the center did not increase as compared to the amount produced by day 5. Systems where the media was replaced continued to produce more matrix, with more matrix at the edges than the center through day 9.

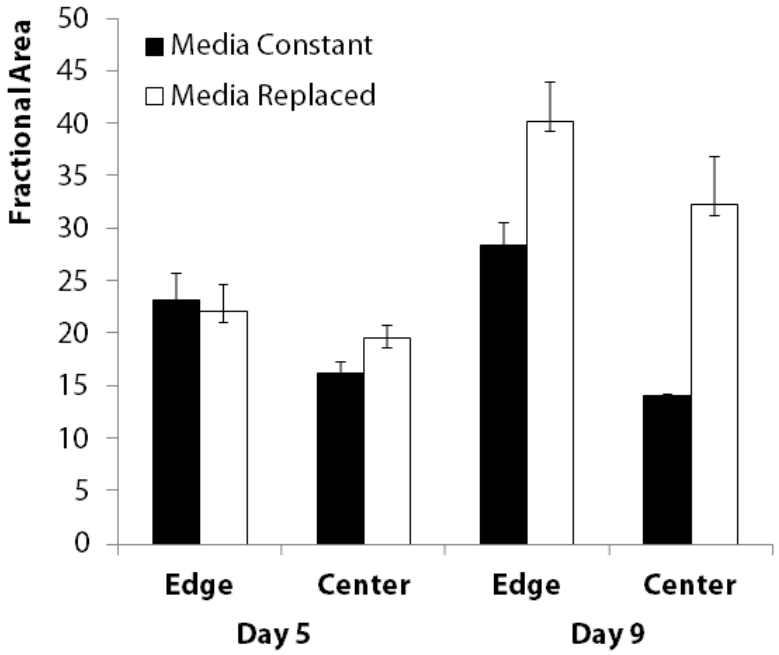

Figure 5.15: Fractional area stained positive for GAGs to indicate matrix production by safrinin-O at the edge and center of chondrocyte-seeded gel sections in the S-STRS at days 5 and 9 with and without $NaHCO_3$-custom media replaced.

For day 9 samples, cell-seeded sections were further examined in six areas, as shown in Figure 5.16A. For cultures where the media was kept constant, matrix production was similar in all regions at the outer edges of the cell-seeded section (edge 1, edge 2, edge 3, center 1, and center 3) with the lowest amount of matrix at the center. Where media is replaced, matrix production covered more than 30% of the field of view for all regions at day 9 (Fig. 5.15 and Fig. 5.16B).

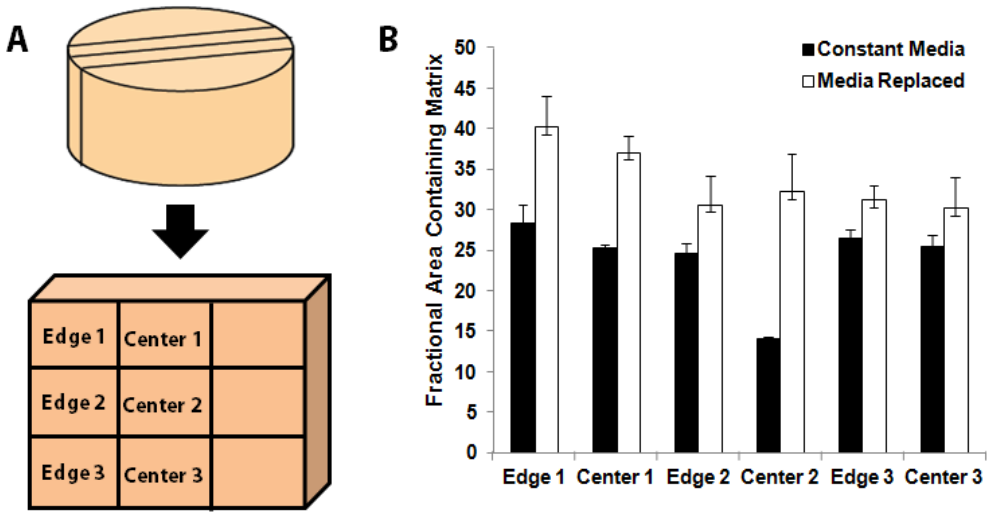

Figure 5.16: Schematic showing the 6 regions that gel sections were examined over (A). The area fraction stained positive for GAGs plotted to indicate matrix production in the 6 regions described in the schematic (B).

5.4.3.8 Calcium and Phosphate Tolerance of Articular Chondrocytes

Calcium and phosphate tolerances of articular chondrocytes were evaluated by examining the viability of cells cultured in media containing different concentrations of calcium and phosphate. Chondrocyte viability in media containing different concentrations of calcium maintained average viabilities >86% through 4 days of culture, with the lowest viability for media supplemented with 0.25 mM $CaCl_2$ and the highest viability of 98% for cultures in $NaHCO_3$-custom media containing 8 mM $CaCl_2$ (Fig 5.17). Through 10 days of culture however, average viability of chondrocytes cultured in media containing 1.4 mM or more calcium had average viabilities less than <33%. Cells cultured in 0.25 mM maintained a good viability at 98%.

Articular chondrocyte viabilities in phosphate-containing media were examined through 9 days. Average viability of chondrocytes cultured in 1.5, 3, 6, and 9 mM Na_2HPO_4 remained > 75% through 9 days of culture (Fig. 5.18). Average viability on day 5 was roughly 95% for all

phosphate concentrations and, by day 9, dropped to roughly 80% for all conditions except for cells cultured in 6 mM Na_2HPO_4, for which viability dropped to 89%.

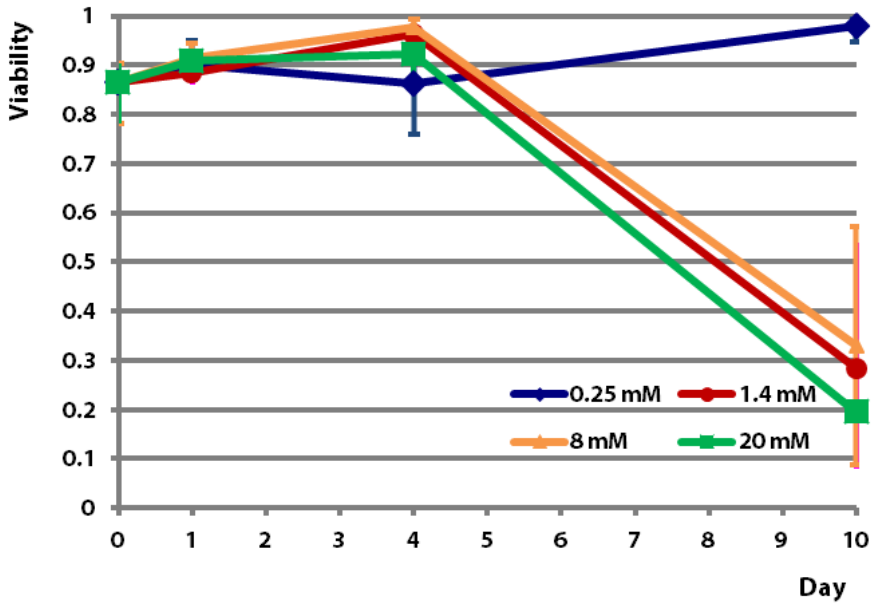

Figure 5.17: Viability of articular chondrocytes cultured in cell-seeded agarose plugs through 10 days of culture in $NaHCO_3$-custom media supplemented with 0.25, 1.4, 8, and 20 mM $CaCl_2$.

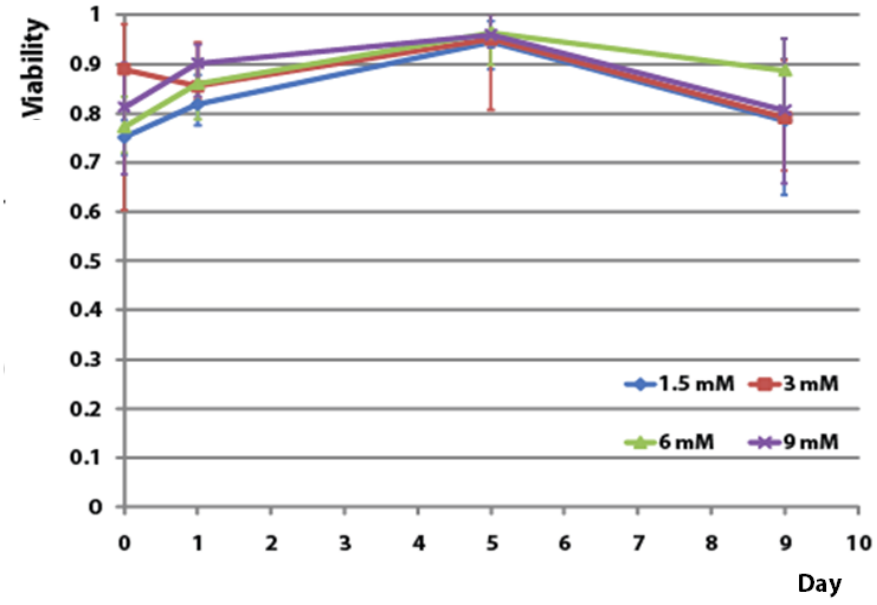

Figure 5.18: Viability of articular chondrocytes cultured in cell-seeded agarose plugs through 10 days of culture in $NaHCO_3$-custom media supplemented with 1.5, 3, 6, and 9 mM Na_2HPO_4.

5.4.3.9 Diffusion of Calcium and Phosphate through STRS

To evaluate the diffusion of calcium and phosphate in the STRS, the concentrations of calcium and phosphate were determined, via ICP, in a 0.7 cm length of gel taken from the center of the 6 cm gel. A baseline calcium concentration value of 2.1 ± 0.1 mM was observed for control gels without calcium supplement. The presence of calcium was contributed by FBS in the culture media (Fig 5.19). For STRS with 8 mM calcium in one reservoir, the concentration of calcium decreased below baseline, before increasing to an average concentration of 3.7 mM on day 9, and then decreasing again. The fluctuation in calcium concentration suggests initial depletion of calcium in the gel through 3 days before an increase in calcium diffusion through the gel. Precipitation of calcium carbonate may have occurred from calcium interaction with the sodium bicarbonate buffer at 8 mM concentrations of calcium, similar to what was observed in media supplemented with 20 mM of calcium.

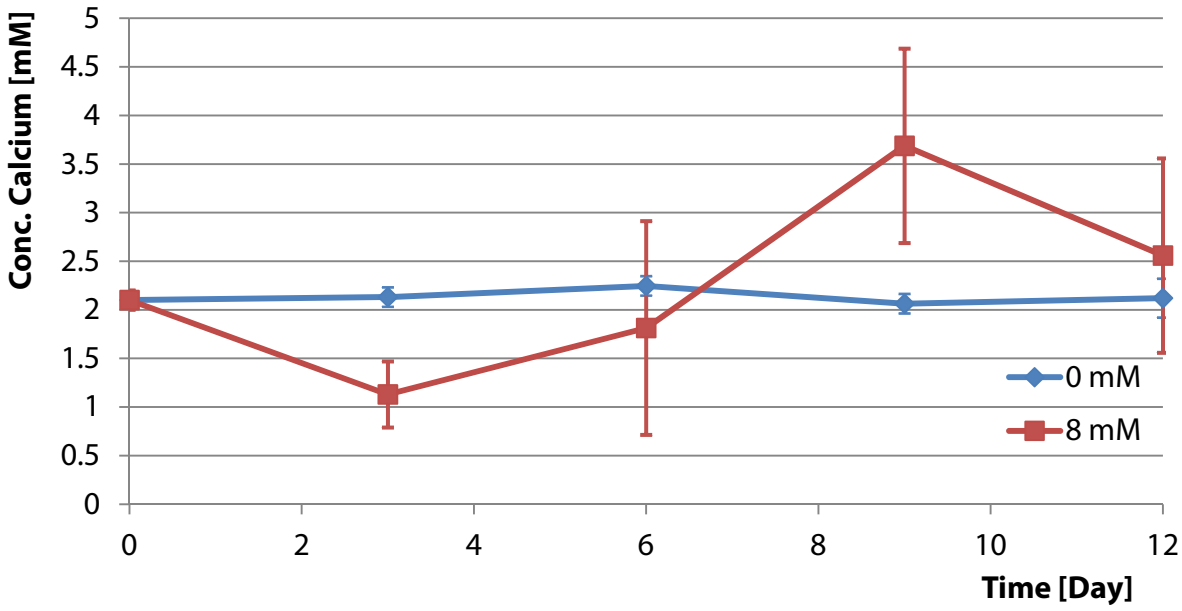

Figure 5.19: Concentration of calcium in a 0.7 cm length of gel taken from the center of the 6 cm gel in the STRS through 12 days with supplement of 0 and 8 mM $CaCl_2$ to the $NaHCO_3$-custom media in one reservoir and no calcium supplement in the opposing reservoir.

The diffusion of phosphate through the STRS was also examined (Fig 5.20). A baseline phosphate concentration of 1.2 ± 0.2 mM was observed in the gel before additional phosphate was added to the media in the reservoirs. The concentration of phosphate reached a steady concentration after 1 day. The apparent equilibrium concentration of phosphate in the gels remains below 30 mM through the course of the experiment, less than the concentration in the P-reservoir (40 mM). Average P-concentrations begin to decrease slightly as phosphate ions reach the opposing reservoir. The P-free reservoir acts as a sink to the phosphate, ensuring that the phosphate concentration in the gel will never reach 40 mM and is expected to continue decreasing until the concentrations of P are equal in both reservoirs.

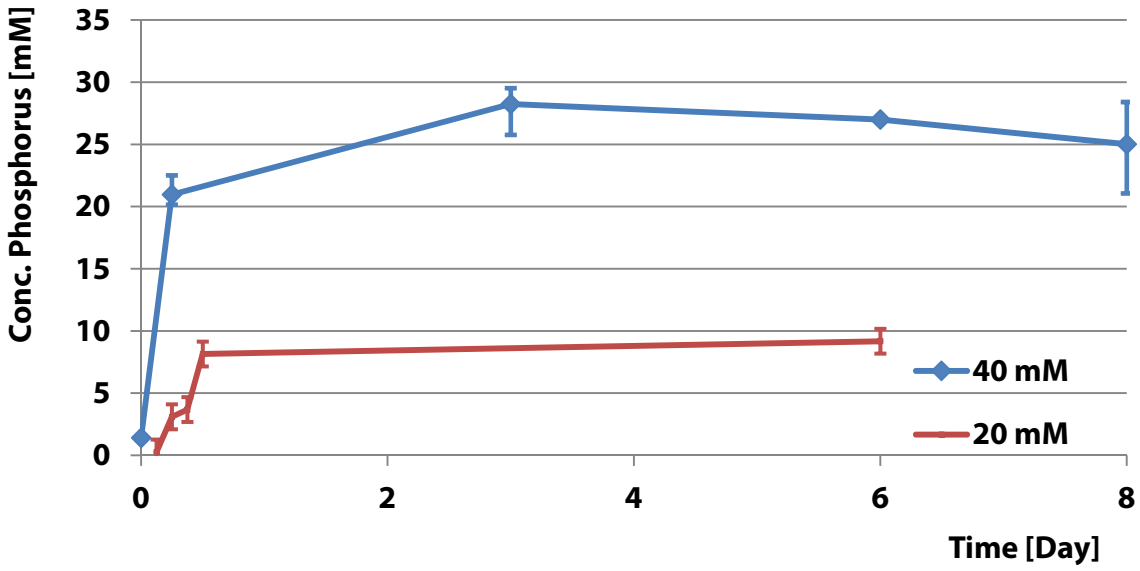

Figure 5.20: Concentration of phosphorus in a 0.7 cm length of gel taken from the center of the 6 cm gel in the STRS through 8 days with supplement of 20 and 40 mM Na_2HPO_4 in the $NaHCO_3$-custom media one reservoir and no phosphate supplement in the opposing reservoir.

5.4.3.10 Summary of Cell Viability and Function in the STRS with Sodium Bicarbonate Buffered Media

The STRS system can support cultures of bovine articular chondrocytes through 5 days with an average viability above 91% and produce GAGs for matrix formation. Supplementing cultures with ascorbic acid promotes cell proliferation in the STRS. Past five days, the media in the STRS needs to be replaced in order to replenish glucose supply to the cells for improved matrix production and to minimize differences in matrix production of cells located at the center of the cell-seeded gel layer and cells located at the edge of the cell-seeded gel layer. The difference in matrix production in the different regions of the cell-seeded layer indicates a limit to the size of cultures in this system. With or without the replacement of media, cell viability remains above 91% through 9 days of culture.

The calcium and phosphate tolerances of articular chondrocytes seeded in agarose gels was inconclusive as the concentration of free calcium ions in the media could not be accurately determined due to the precipitation of calcium carbonate in the media. The irregularity of calcium content in the gels as determined by ICP corroborates the presence of Ca-buffer interaction. Articular chondrocytes tolerated up to 9 mM phosphate, higher concentrations may also be tolerated but were not investigated due to the restriction from the calcium concentrations. To investigate mineral formation in the STRS, an alternative buffer was examined in the STRS.

5.4.4 Optimizing STRS for Mineralization

5.4.4.1 Mineral Formation in the STRS

In preparation to examine the formation of mineral in the STRS in the presence of cells, initial mineralization experiments in the S-STRS was done in the absence of cells in Tris and

HEPES buffer. Opposing reservoirs were filled with 100 mM $CaCl_2$ and 100 mM Na_2HPO_4 in Tris buffer and pH balanced to 7.4. Silicone tubes fully coated with PEI and coated with PEI with a PEI-free window were used in the STRS. Mineralization was allowed to occur for 5 days before gels were removed from the S-STRS (Fig 5.21).

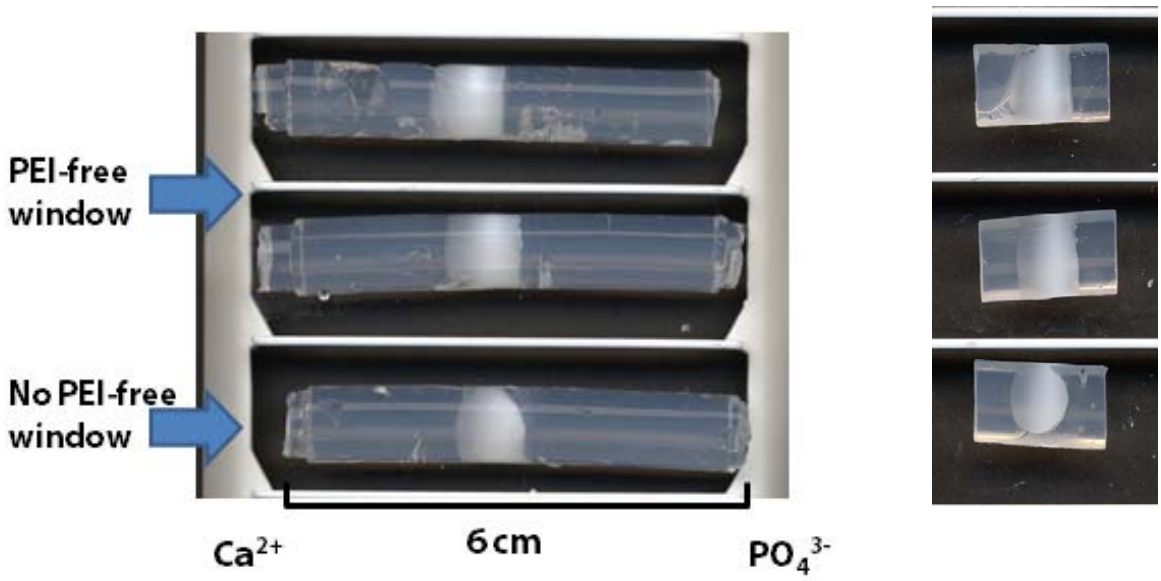

Figure 5.21: Mineral bands formed in the S-STRS system with 100 mM $CaCl_2$ and 100 mM Na_2HPO_4 in Tris buffer in opposing reservoirs after 5 days. S-tubes were coated with and without PEI at the center of the tube (right). Cross-section of mineral band (left).

Mineral bands 1 cm in length were consistently formed slightly off center towards the calcium reservoir. In tubes that were coated with PEI, the edges of the mineral band were slightly rounded away from the interface of gel and tube, suggesting that PEI inhibited mineral growth. Mineralization in the STRS was also examined in 20 mM HEPES-custom media containing 50 mM $CaCl_2$ and 50 mM Na_2HPO_4. After 6 days of mineralization, gels were removed from the S-STRS and mineral density and location was determined by relative changes in gray value through ImageJ. It was noted that the elapsed time between preparation and usage of the HEPES-custom media containing calcium affected the band location (Fig. 5.22).

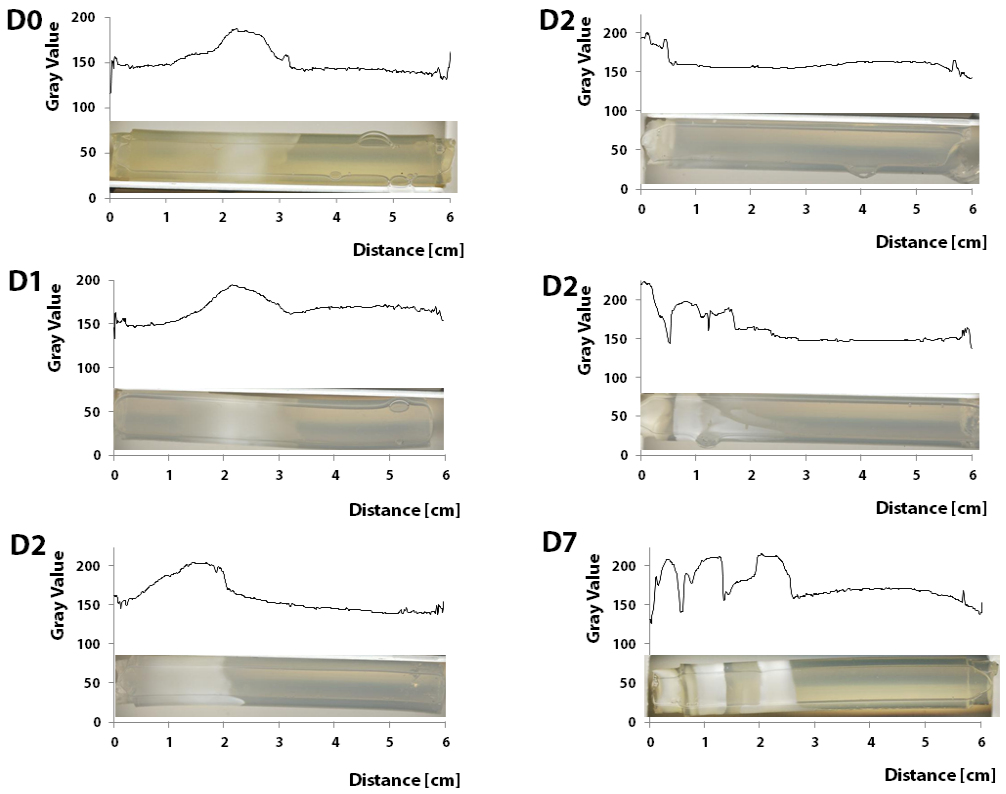

Figure 5.22: Mineral bands formed in S-STRS system in HEPES-custom media with media aged 0 (D0, representative image), 1 (D1), 2 (D2), and 7 (D7, representative image) before addition to the reservoirs.

HEPES-custom media prepared 0-1 days before use had mineral band formation starting at the center of the gel at 3 cm then extending towards the calcium reservoir to form mineral bands slightly less than 2 cm in length (Fig. 5.22, D0, D1). The center of the 1 cm mineral band is more densely mineralized than the edges of the band. Mineralization with HEPES-custom media prepared 2 days before use showed several variations in the location and number of mineral bands (Fig. 5.22, D2). Systems that used HEPES-custom media prepared 7 days before use formed 3 mineral bands on the calcium end of the reservoir. To minimize these inconsistencies in mineral band formation for mineralization experiments in the STRS, HEPES-custom media supplemented with calcium was prepared the day the STRS was set up for an

experiment. Mineralization of gels using freshly prepared HEPES custom media supplemented with calcium formed mineral bands consistently between the 1 - 3 cm region from the Ca-reservoir in the gel in the STRS without cells (Fig. 5.23).

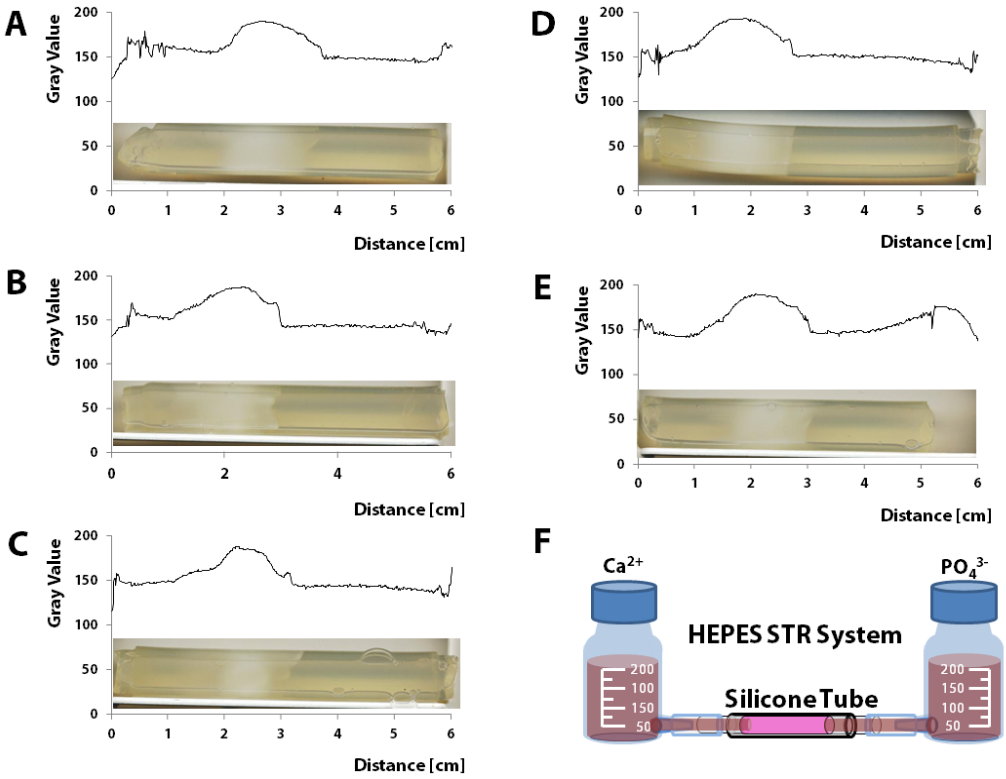

Figure 5.23: Mineral bands formed in HEPES-custom media prepared the day of setting up the S-STRS (A-E) with a line scan along the length of the gel for relative mineral density. Schematic of the S-STRS with Ca-media on the left reservoir and P-media on the right (F).

Mineralization in $NaHCO_3$-buffered media was not examined as calcium concentrations at 20 mM resulted in precipitation of $CaCO_3$ and lower concentrations were unable to form mineral bands within the gel in the allotted time period.

5.4.4.2 Mineralization in the Presence of Articular Chondrocytes

Articular chondrocytes were seeded in the S-STRS at the location of mineral band formation observed before (Fig. 5.23) at 2 cm lengths in the tube (Fig. 5.24) in 20 mM HEPES-custom media as controls. 20 mM HEPES-custom media was also prepared with 50 mM $CaCl_2$ and 50 mM Na_2HPO_4 and placed into opposing reservoirs for mineralization (Fig. 5.25F). Systems were cultured for 6 days.

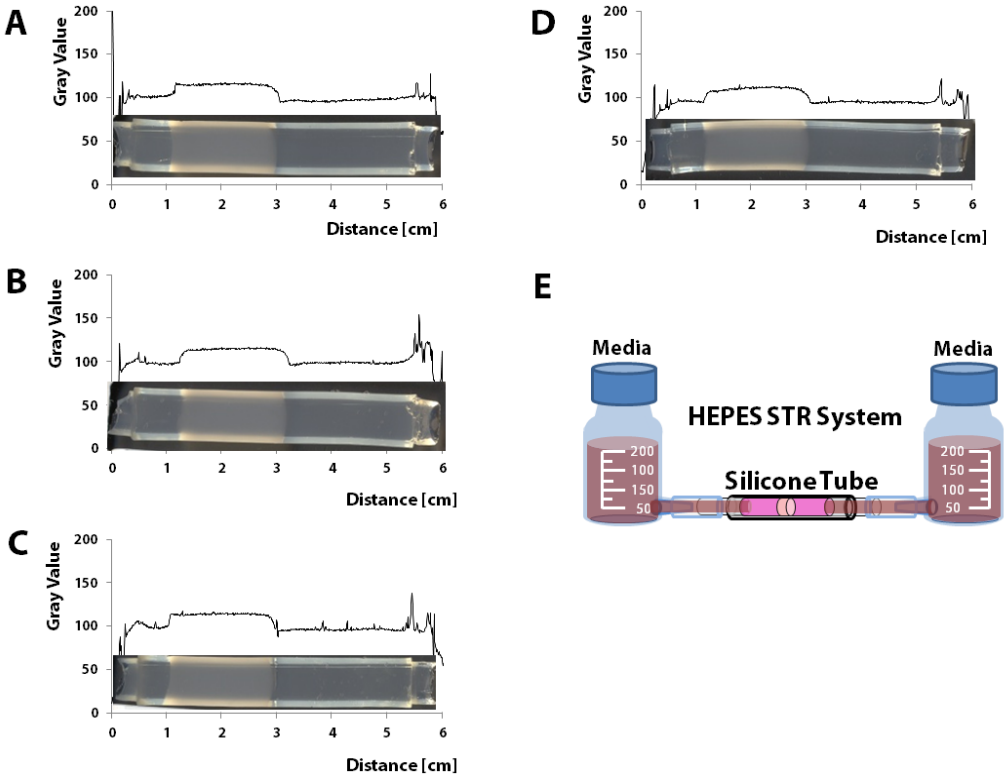

Figure 5.24: Chondrocyte-seeded agarose gels in S-STRS in HEPES-custom media with a line scan along the length of the gel showing cell-seeded location (A-D). Schematic of the S-STRS with Ca-media on the left reservoir and P-media on the right (E).

After 6 days, gels were removed from the S-STRS and mineral density and location was determined by relative changes in gray value through ImageJ (Fig 5.25).

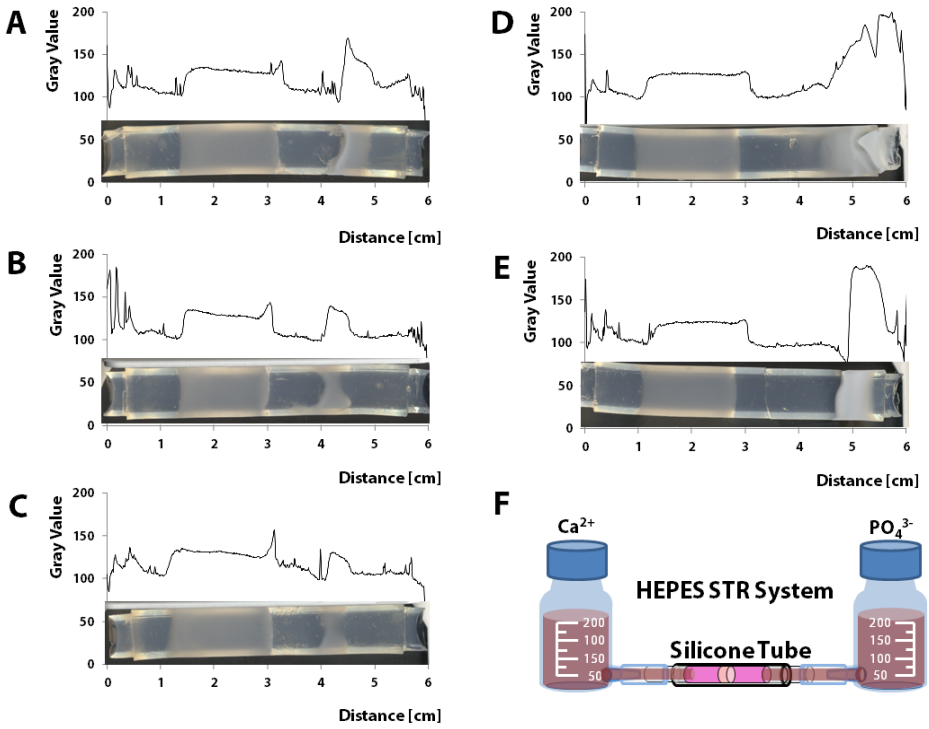

Figure 5.25: Scanned images of chondrocyte-seeded gels under mineralizing conditions after 5 days with line scans across the gel to determine relative changes in density to show the cell-seeded section of the gel and mineral location (A-E). Schematic showing S-STRS set up with Ca-media on the left reservoir and P-media on the right (F).

Two types of band formation were observed, designated as Type I and Type II. Type I mineralization (Fig. 5.25 A-C) showed the presence of two mineral bands and was observed in four out of six systems. A larger band, between 4-5 cm from the Ca-reservoir, was observed as well as a second, narrower band just inside the cell-seeded gel section closer to the P-reservoir (Fig. 5.26). Cross-sections at the two mineral bands showed discrete nodules of mineral at the smaller band (Fig. 5.27A) and a diffuse band of mineral through most of the gel cross-section for the larger band (Fig. 5.27B).

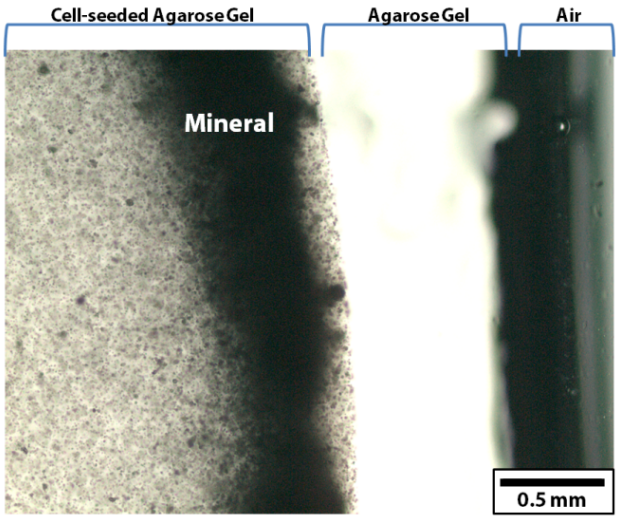

Figure 5.26: Optical microscopy image of the mineral band formed at the edge of the chondrocyte-seeded gel section of Type I mineralization in the S-STRS with HEPES-custom media.

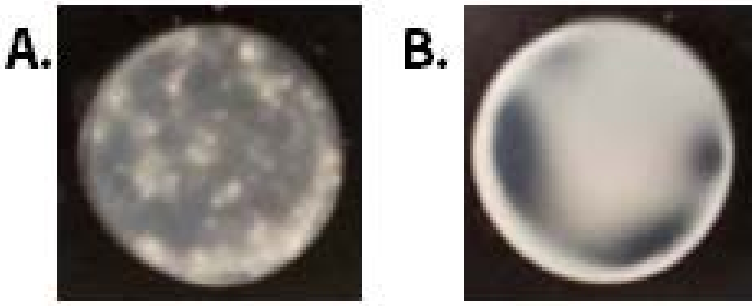

Figure 5.27: Cross-section of Type I mineral bands showing the band formed in the chondrocyte-seeded section of the gel (A) and the band closer to the P-reservoir (B).

Type II mineralization was observed in two out of six systems (Fig 5.25 D-E). Two mineral bands were also observed from the gray value line scan. However, the smaller mineral band at the end of the cell-seeded section of the gel closer to the P-reservoir was not visible by eye. The larger band formed roughly 4.5 cm away from the Ca-reservoir. The solution of the P-reservoir remained clear, indicating that most of the Ca ions were retained in the gel and did not reach the P-reservoir.

5.4.4.3 Mineral Analysis in the S-STRS in HEPES Buffered Media

The mineral bands were sectioned from the gel, washed thrice in 0.15 M NH_4OH, freeze-dried and analyzed via pXRD (Fig. 5.28). There was not enough mineral from the smaller band in Type II mineralization to be examined via pXRD. A broad hump between 13° and 23° was seen for all samples and attributed to the agarose gel. XRD analysis of mineral formed in acellular STRS displayed a single sharp peak at 32° indexed to hydroxyapatite (HA, $Ca_{10}(PO_4)_6(OH)_2$) {211} and the absence of the peak for {002} in three out of four samples (Fig. 5.28Ai). The fourth sample showed peaks indexed for octacalcium phosphate (OCP, $Ca_8H_2(PO_4)_6 \cdot 5H_2O$) (Fig. 5.28Aii).

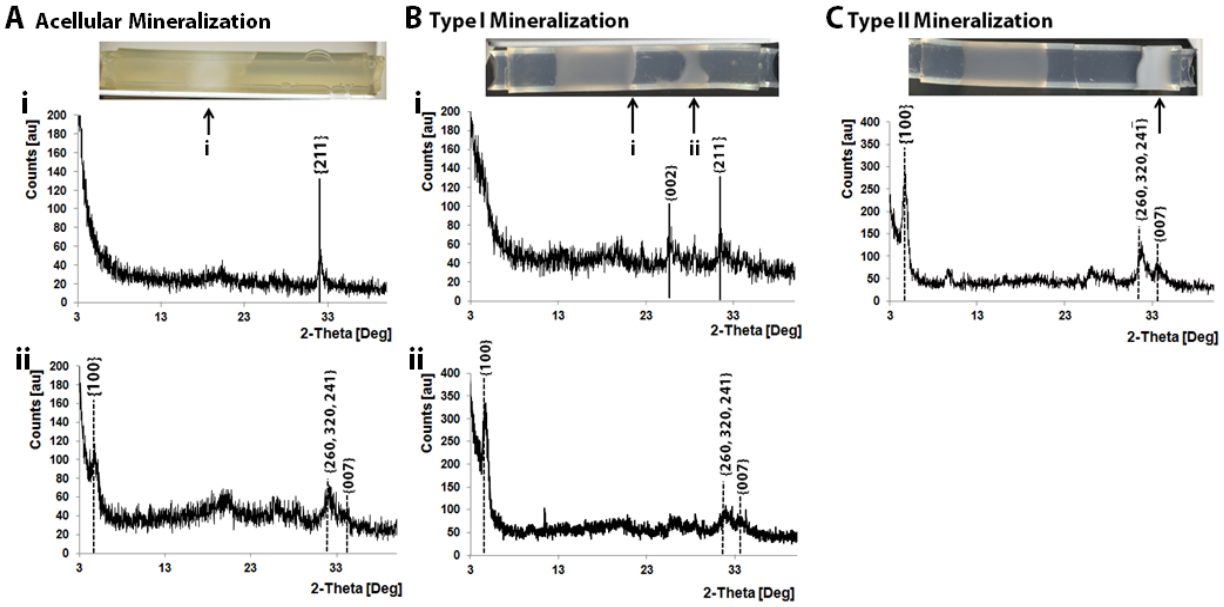

Figure 5.28: pXRD patterns from mineral sectioned from the S-STRS with HEPES-custom media formed without cells present (A) and Type I mineralization (B) and Type II mineralization (C) in the presence of chondrocytes. Miller indices of HA are indicated by the solid lines and Miller indices of OCP are indicated by the dotted lines.

The larger mineral band in Type I mineralization and the mineral band in Type II mineralization was determined to be OCP (Fig. 5.28Bii, C). OCP crystals in Type II mineralization appears more crystalline and may be larger in size due to the shaper, more defined peaks present (Fig. 5.28C). The smaller mineral band in Type I mineralization appears to be HA.

5.4.4.4 Chondrocyte Viablity in the STRS with HEPES Buffered Media

Chondrocyte viability in the S-STRS in HEPES buffered media in 0.4 cm and 2 cm cell-seeded lengths was examined, as well as the viability in systems with Ca and P added to the reservoirs after 6 days of culture (Fig. 5.29). It was observed in all systems a high degree of cell death through the length of the cell-seeded section for all samples where the cell-seeded sections closer to the Ca^{2+} reservoir (Fig. 5.29B section A) had viabilities above 11%. Shorter cell-seeded lengths maintained viabilities above 14% in sections A & B (Fig. 5.29B, section B), but dropped to slightly above 11% in section C (Fig. 5.29B, section C). Longer cell-seeded sections had viabilities above 14% away from the center in section A and C, which fell to 9% in the center region (B). On introducing calcium and phosphate into the system, where section A was closer to the Ca-reservoir and section C was closer to the P-reservoir, viabilities were above 14% closer to the Ca-reservoir and nearly 0% in sections B and C. Chondrocytes maintained spherical phenotype through these experiments.

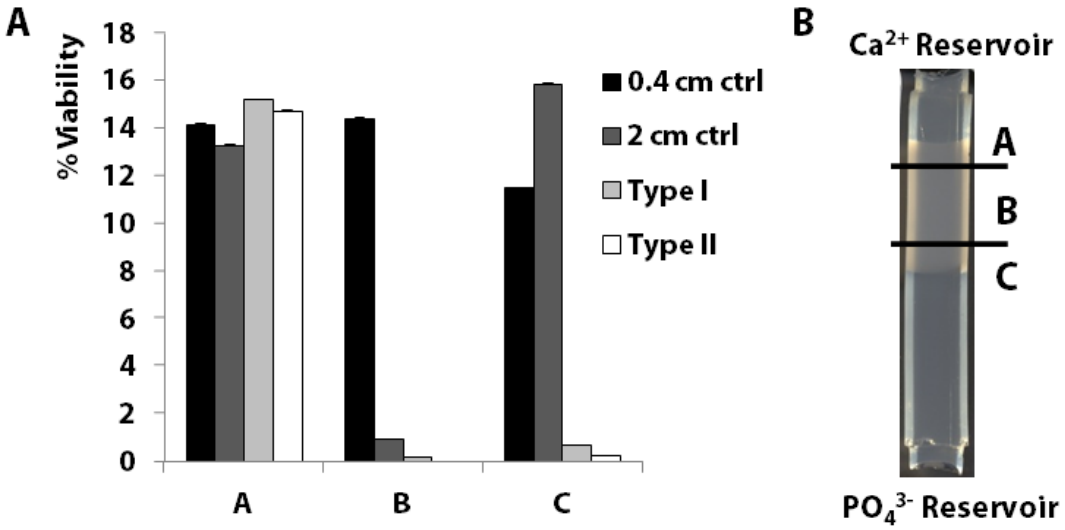

Figure 5.29: A. Viability of articular chondrocytes in the S-STRS with HEPES-custom media cultured in 0.4 cm cell-seeded length, 2 cm cell-seed length, and 2 cm cell seeded length with the appearance of Type I and Type II mineralization. B. Viabilities were examined along the edge closest to the Ca^{2+} reservoir (A), center of the cell-seeded section (B), and the edge closest to the PO_4^3-reservoir (C) (B).

5.5 Discussion

Developing 3-D culture systems that allow for temporal and spatial gradients is challenging as the system needs to be confined, contain a source(s) for introducing the material of interest to form gradients in the system, and sustain cell health and viability through the duration of the experiment. To form such a system, the Single Tube Reservoir System was constructed where cells can be seeded within an agarose-filled silicone tube that is fitted to two media bottles, which can dispense nutrients and introduce gradients of ions, growth factors, and other molecules or proteins of interest. To improve agarose adhesion to the tube walls, PEI, a positively charged polymer, shown to assist in cell attachment [31], was coated on inner tube surface. Studies utilizing PEI for gene transfection have shown PEI to be toxic to certain cell

types in a dose dependent manner [32] and with increasing positive charge [33]. Cell cultures in fully coated PEI tubes showed a region of cell death; henceforth tubes were either not coated with PEI or coated and left with a PEI-free section of tube for the cell-seeded section of gel.

Articular chondrocytes were able to go through cellular division, produce matrix, and sustain viabilities above 90% through 12 days of culture in the S-STRS in the presence of $NaHCO_3$-custom media. Cell division occurred earlier with the introduction of ascorbic acid into the system. Despite maintaining viability above 90%, chondrocytes located in the center of the cell-seeded gel section produced less matrix and showed less cell division. The length of the cell-seeded gel layer is limited as cells at the outer edges of the culture consume nutrients and other molecules or ions needed for function and deplete the amount that is able to diffuse towards cells seeded at the center of the cultures [34, 35]. The increased matrix production at the edges of the cell-seeded gel may also further restrict the exchange of waste and nutrients from the cells closer to the center [36]. The decrease in matrix production can be alleviated by replacing the media in the reservoirs every three days to introduce fresh nutrients to the cells, however increasing the length in unfavorable conditions leads to cell death, as seen in STRS with HEPES-custom media.

Buffers are an important component of the system in order to maintain pH suitable for cells and mineral formation. Over time, chondrocyte cultures go through pH fluctuations from acid build up from anaerobic processes and buffers are required to maintain pH [37]. Here we examined cell response to sodium bicarbonate and HEPES buffer and mineral formation in Tris and HEPES buffer. Cell viability was highest for sodium bicarbonate buffered media and low for HEPES buffered media although both buffers are commonly used in cell culture [38]. Tris has been demonstrated to be cytotoxic to cells in previous studies by preventing deactivation of

proteolytic enzymes which can break down the cell membrane and inhibit enzymatic binding. These effects are reduced in cultures with HEPES buffer [39], thus HEPES was used in the STRS to compare mineral formation in the STRS to previous work done in with the Boskey double diffusion system which uses Tris buffer [19]. HEPES buffer is a commonly used buffer for cell culture at concentrations up to 50 mM [40]; however studies have shown adverse effects on mammalian cells by disrupting ion channels [41] and the cellular membrane [42]. In chondrocyte culture, where there is acid built up, sodium bicarbonate has been demonstrated as the better buffer in maintaining pH and improving cell proliferation and matrix production [37, 43]. These previous studies, as well as the experiments described here, demonstrate $NaHCO_3$ to be the preferred buffer system for maintaining chondrocyte health and viability. None of these reports, however, have reported drastic decreases in cell viability for HEPES buffered media as was observed here, and therefore, cell death may not be due solely to the change in buffers. Additionally, for gradient studies involving calcium, $NaHCO_3$ is an inappropriate buffer to use due to the precipitation of $CaCO_3$ in the calcium reservoir.

Introducing cell culture media into the system adds complexity to the system as many of the components may interact with the gradient of interest. Here, we used HEPES buffered media supplemented with 10% FBS, and 1% AB/AM in order to examine mineral formation in the STRS. Fetal bovine serum contains significant amounts of fetuin-A, a protein known to inhibit mineralization by binding calcium phosphate to form mineral pre-nucleation clusters loaded with fetuin-A and acts as a mineral carrier at higher concentrations of calcium and phosphate [44]. HEPES buffer also interacts with calcium, as shown by the change in mineral band formation with the aging of calcium-containing HEPES buffered media in this study and by others [40, 45]. These factors may inhibit mineral formation so that mineral bands formed in HEPES buffered

media are more diffuse and form closer to the Ca-reservoir as compared to mineral bands formed in Tris buffer. These experiments demonstrate the need to establish controls for studying gradient formation in the presence of buffer and media before the introduction of cells.

Preliminary examination of mineral formation in the presence of articular chondrocytes in the STRS showed a shift in the location of mineral formation from the Ca-reservoir to the P-reservoir. The lower cell viabilities in HEPES buffered system with and without additional calcium and phosphate make it difficult to attribute the shift in band location to an active response from the articular chondrocytes to elevated levels of calcium and phosphate. The shift may be due to the presence of proteins and enzymes released by the cells in death. The thin mineral band found on the P-side of the cell-seeded agarose is intriguing, however further investigation is necessary to understand what is occurring in the system.

5.6 Conclusions

The STRS was developed to provide a system that could sustain cell viability and function within a 3-D culture environment that could be applied with 1-D diffusion of ions, gases, and nutrients. The current form of the STRS has been optimized to sustain articular chondrocyte viability and health with sodium bicarbonate buffer; however this buffer restricts introducing gradients of chemicals, which will interact with the sodium bicarbonate buffer such as calcium. HEPES buffered media, also used in conventional cell culture, had less interaction with calcium ions. On replacing the sodium bicarbonate buffer with HEPES buffer, the STRS was not able to sustain cell health and viability above 90%. Despite the inability to sustain cell viability, preliminary studies demonstrate that the presence of articular chondrocytes can affect mineral formation within the STRS. Examination of what is being released by the articular

chondrocytes is necessary for understanding this shift in mineral formation. Further work to optimize the system for cells in HEPES buffer is a prerequisite before understanding how the cells can actively affect the mineralization process. The STRS is time intensive to set up and requires significant amounts of media and space; however it demonstrates the potential of such a system to provide answers on cell response to temporal and spatial gradients unavailable in other systems.

References

[1] Keenan TM, Folch A. Biomolecular gradients in cell culture systems. Lab Chip 2008;8:34-5.

[2] Tortelli, F, Cancedda, R. Three-dimensional cultures of osteogenic and chondrogenic cells: a tissue engineering approach to mimic bone and cartilage in vitro. Eur Cell Mater 2009;17:1-14.

[3] Ngyuyen KT, West JL. Photopolymerizable hydrogels for tissue engineering applications. Biomaterials 2002;23(22):4307-14.

[4] Lutolf MP. Integration column: artificial ECM: expanding the cell biology toolbox in 3D. Integr Biol 2009;1:235-41.

[5] Slaughter BV, Khurshid SS, Fischer OZ, Khademhosseini A, Peppas N. Hydrogels in regenerative medicine. Adv Mater 2009;21:3307-29.

[6] Cheung YK, Azeloglu EU, Shiovitz DA, Costa KD, Seliktar D, Sia SK. Microscale control of stiffness in a cell-adhesive substrate using microfluidics-based lithography. Angew Chem Int 2009;48:7188-92.

[7] Chatterjee K, Lin-Gibson S, Wallace WE, Parekh SH, Lee YJ, Cicerone MT, Young MF, Simon CG Jr. The effect of 3D hydrogel scaffold modulus on osteoblast differentiation and mineralization revealed by combinatorial screening. Biomaterials 2010;31:5051–62.

[8] Jiang J, Tang A, Ateshian GA, Guo XE, Hung CT, Lu HH. Bioactive stratified polymer ceramic-hydrogel scaffold for integrative osteochondral repair. Ann Biomed Eng 2010;38(6):2183-96.

[9] Jiang J, Nicoll SB, Lu HH. Co-culture of osteoblasts and chondrocytes modulates cellular differentiation in vitro. Biochem Biophys Res Commun 2005;63:521-8.

[10] Khanarian NT, Haney NM, Burga RA, Lu HH. A functional agarose-hydroxyapatite scaffold for osteochondral interface regeneration. Biomaterials 2012;33:5247-58.

[11] Liu Z, Xiao L, Xu B, Zhang Y, Mak AFT, Li Y, Man W, Yang M. Covalently immobilized biomolecule gradient on hydrogel surface using a gradient generating microfluidic device for a quantitative mesenchymal stem cell study. Biomicrofluidics 2012;6(2):024111-12.

[12] Sant S, Hancock MJ, Donnelly JP, Iyer D, Khademhosseini A. Biomimetic gradient hydrogels for tissue engineering. Can J Chem Eng 2010;88:899-911.

[13] Dorvee JR, Boskey AL, Estroff LA. Rediscovering hydrogel-based double-diffusion systems for studying Biomineralization. CrystEngComm 2012;14:5681-700.

[14] Peret BJ, Murphy WL. Controllable soluble protein concentration gradients in hydrogel networks. Adv Funct Mater 2008;18(21):3410-7.

[15] Henisch HK. Crystal Growth in Gels. Dover Publications; 1996.

[16] Silverman L, Boskey AL. Diffusion systems for evaluation of Biomineralization. Calcified Tissue Int 2004;75(6):494-510.

[17] Hunter GK, Goldberg HA. Nucleation of hydroxyapatite by bone sialoprotein. Proc Natl Acad Sci 1993;90(18):8562-5.

[18] Ijima M, Moradian-Oldak J. Control of apatite crystal growth in a fluoride containing amelogenin-rich matrix. Biomaterials 2005;26(13):1505-603.

[19] Boskey AL. Hydroxyapatite formation in a dynamic collagen gel system- effects of Type-I collagen, lipids, and proteoglycans. J Phys Chem 1989;93(4):1628-33.

[20] Gardner DL, Mzuryk R, O'Connor P, Orford CR. Anatomical changes and pathogenesis of OA in man, with particular reference to the hip and knee joints. Studies in osteoarthrosis. John Wiley & Sons, Chichester; 1989:21-48.

[21] Kheir E, Shaw D. Hyaline articular cartilage. Orthop Trauma 2009;23(6):450-5.

[22] Silver IA. Measurement of pH and Ionic Composition of Pericellular Sites. Philos Trans R Soc Lond B Biol Sci 1975;B271:261-272.

[23] Urban JPG. The chondrocyte: a cell under pressure. Br J Rheumatol 1994;33:901-8.

[24] Zizak I, Roschger P, Paris O, Misof BM, Berzlanovich A, Bernstorff S, Amenitsch H, Klaushofer K, Fratzl P. Characteristics of mineral particles in the human bone/cartilage interface. J Struct Biol 2003;141(3):208-17.

[25] Sedi A, Ramalingam M, Elluomi-Hannachi I, Ostrovidov S, Khademhosseini A. Gradient biomaterials for soft-to-hard interface tissue engineering. Acta Biomater 2011;7(4):441-51.

[26] Wang W, Kirsch T. Retionic acid stimulates annexin-mediated growth plate chondrocyte mineralization. J Cell Biol 2002;157(6):1061-9.

[27] Poole A, Kobayashi M, Yasuda T, Laverty S, Mwale F, Kojima T, Sakai T, Wahl C, El-Maadawy S, Webb G, Tchetina E, Wu W. Type II collagen degradation and its regulation in articular cartilage in osteoarthritis. Ann Rheum Dis 2002;61(Suppl 2):ii78-81.

[28] Poole AR, Rosenberg LC, Reiner A, Ionesou M, Bogoch E, Roughley PJ. Contents and distributions of the proteoglycans decorin and biglycan in normal and osteoarthritic human articular cartilage. J Orthop Res 1996;14:681-9.

[29] ANGUS Chemical Company Technology Review, Biotechnology Applications of TRIS AMINO® (TRIS buffer), JDN-Form No. 319-00072, 2000.

[30] Ligou JC, Nahas GC. Comparative effects of acidosis induced by acid infusion and CO_2 accumulation. Am J Physiol 1960;198:1201-6.

[31] Vancha AR, Govindaraju S, Parsa KVL, Jasti M, González-García M, Ballestero RP. Use of polyethyleneimine polymer in cell culture as attachment factor and lipofection enhancer. BMC Biotechnol 2004;4:23.

[32] Boeckle S, von Gerdorff K, van der Piepen S, Culmsee C, Wagner E, Ogris M. Purification of polyethylenimne polyplexes highlights the role of free polycations in gene transfer. J Gene Med 2004;6(10):1102-11.

[33] Forrest ML, Meister GE, Koerber JT, Pack DW. Partial acetylation of polyethylenimine enhances in vitro gene delivery. Pharm Res 2004;21:365–71.

[34] Buckley CT, Thorpe SD, Kelly DJ. Engineering of large cartilaginous tissues through the use of microchanneled hydrogels and rotational culture. Tissue Eng Part A 2009;15(11):3213-20.

[35] Kelly TAN, Ng KW, Wang CCB, Ateshian GA, Hung CT. Spatial and temporal development of chondrocyte-seeded agarose constructs in free-swelling and dynamically loaded cultures. J Biomech 2006;39:1489-97.

[36] Martin I, Wendt D, Heberer M. The role of bioreactors in tissue engineering. Trends Biotechnol 2004;22(2):80-6.

[37] Xu X, Urban JPG, Browning JA, Tirlapur U, Wilkins RJ, Wu MH, Cui Z, Cui Z. Influences of buffer systems on chondrocyte growth during long-term culture in alginate. Osteoarthritis Cartilage 2007;15(4):396-402.

[38] Fundamental techniques in cell culture – 2nd Edition. European Collection of Cell Cultures and Sigma-Aldrich; 2010.

[39] Lubas WA, Spiro RG. Evaluation of the role of rat liver Golgi endo-alpha-D-mannosidase in processing N-linked oligosaccharides. J Biol Chem 1988;263(8):3990-8.

[40] Pasch A, Farese S, Gräber S, Wald J, Richtering W, Floege J, Jahnen-Dechent W, A nanoparticle-based serum test measuring overall calcification inhibition, J Am Soc Nephrol 2012;23(10):1744-52.

[41] Yamamoto D, Suzuki N. Blockage of chloride channels by HEPES buffer. Proc R Soc Lond Biol Sci 1987;232:93-100.

[42] Poole CA, Reilly HC, Flint MH. The adverse effects of HEPES, TES, and BES zwitterion buffers on the ultrastructure of cultured chick embryo epiphyseal chondrocytes. In Vitro 1982;18:755-65.

[43] Waldman SD, Couto DC, Omelon SJ, Kandel RA. Effect of sodium bicarbonate on extracellular matrix accumulation, and morphology of cultured articular chondrocytes. Tissue Eng 2004;10(11-12):1633-40.

[44] Jahnen-Dechent W, Heiss A, Schäfer C, Ketteler M. Fetuin-A regulation of calcified matrix metabolism. Circ Res 2011;108(12):1494-509.

[45] Jalota S, Bhaduri SB, Tas AC. Effect of carbonate content and buffer type on calcium phosphate formation in SBF solutions, J Mater Sci Mater Med 2006;17(8):697-707.